EXPERIMENTAL STUDY OF TERRESTRIAL ELECTRON ANTI-NEUTRINOS WITH KAMLAND

A DISSERTATION
SUBMITTED TO THE DEPARTMENT OF PHYSICS
AND THE COMMITTEE ON GRADUATE STUDIES
OF STANFORD UNIVERSITY
IN PARTIAL FULFILLMENT OF THE REQUIREMENTS
FOR THE DEGREE OF
DOCTOR OF PHILOSOPHY

Nikolai R. Tolich
March 2005

I certify that I have read this dissertation and that in my opinion it is fully adequate, in scope and quality, as a dissertation for the degree of Doctor of Philosophy.

Giorgio Gratta
(Principal Adviser)

I certify that I have read this dissertation and that in my opinion it is fully adequate, in scope and quality, as a dissertation for the degree of Doctor of Philosophy.

Norman Sleep

I certify that I have read this dissertation and that in my opinion it is fully adequate, in scope and quality, as a dissertation for the degree of Doctor of Philosophy.

Patricia Burchat

Approved for the University Committee on Graduate Studies:

Abstract

The analysis presented here uses Kamioka Liquid scintillator Anti-Neutrino Detector (KamLAND) to measure the rate of electron anti-neutrinos, $\bar{\nu}_{\mathrm{e}}$'s, produced from terrestrial ^{238}U and ^{232}Th. ^{238}U and ^{232}Th are thought to be the main heat source driving mantle convection in the Earth, which in turn is responsible for plate tectonics. The total terrestrial ^{238}U and ^{232}Th content has been estimated from Earth models and rock samples from a very small fraction of the Earth. Until now there have been no direct measurements. Since $\bar{\nu}_{\mathrm{e}}$'s have an exceedingly small cross section, they propagate undisturbed in the Earth interior, and their measurement near the Earth surface can be used to gain information on their sources.

Based on a total of $(2.63 \pm 0.19) \times 10^{31}$ target proton-years (0.506 kton-years), the 90 % confidence interval for the total number of terrestrial ^{238}U and ^{232}Th $\bar{\nu}_{\mathrm{e}}$'s detected is 4 to 40. This is consistent with the best models of terrestrial ^{238}U and ^{232}Th content.

Acknowledgments

KamLAND is supported by the Center of Excellence program of the Japanese Ministry of Education, Culture, Sports, Science, and Technology under grant 09CE2003, and by the United States Department of Energy under grant DEFG03-00ER41138. The reactor data are provided courtesy of the following electric associations in Japan: Hokkaido, Tohoku, Tokyo, Hokuriku, Chubu, Kansai, Chugoku, Shikoku, and Kyushu Electric Power Companies, Japan Atomic Power Company, and the Japan Nuclear Cycle Development Institute. The Kamioka Mining and Smelting Company provided service for activities in the mine. Part of my funding was provided by a generous grant from the Stanford Graduate Fellowship.

This work was only possible due to the vision of Atsuto Suzuki and the hard work of the entire KamLAND collaboration. The following deserve particular thanks: Sanshiro Enomoto for the many insightful discussions on terrestrial neutrinos and for teaching me almost every thing I know about DAQ's and electronics, Patrick Decowski and Glenn Horton-Smith for helping me come to grips with the KamLAND analysis tools, and analysis in general, and Bruce Berger for being my goto guy when it comes to the "Fine Berkeley Electronics". Also thanks go to the people who managed to make spending so much time underground bearable, and sometimes even enjoyable: Brian Fujikawa, Mitsuko Murakami, Evgueni Yakushev, Kengo Nakamura, Masayuki Koga, Jelena Maricic, Diane Markoff, Tanya Miletic, Kevin Lesko, Tim Classen, Christopher Mauger, and many others.

For the help I got while developing the trigger, I would like to thank YiFang Wang, Dennis Murphree, Fred Bieser, Thorsten Stezelberger, John Wolf, and Mark Freitag.

I would like to thank my thesis committee for taking the time to read this thesis

and providing me with useful comments. Particularly I appreciate that Norm Sleep took the time to explain simple geophysical concepts to me.

I would like to thank my advisor Giorgio Gratta, from whom I have leant so much knowledge that will help me for my future in neutrino physics or whatever path my career takes. Many thanks go to Sam Waldman, Jesse Wodin, Yoshi Uchida, Naoko Kurahashi, Matt Green, Russell Neilson, and the rest of the Gratta research group. You all made my time here at Stanford extremely enjoyable. I also thank Linda Hubly for taking care of me while I was in the Gratta research group.

A huge thank-you goes to Jason Detwiler, who was the person who single handedly kept me sane during my time in the mine, and who helped me immensely with all aspects of this work from computer code to analysis discussions. I do not know how this would have turned out without him.

The one person I have to thank the most is my fiancee Kazumi Ishii. Not only did she spend so much time reading this thesis, but she also encouraged me when I needed encouragement, and filled my life with love.

Finally I would like to thank my parents Sandra and Tony Tolich, and the rest of my family for the love and support they have given me.

Contents

List of Tables

List of Figures

Chapter 1

Introduction

The idea of using electron anti-neutrinos, $\bar{\nu}_{\mathrm{e}}$'s, to study processes inside the Earth was first suggested by Eder[1] and Marx[2]. ^{238}U, ^{232}Th, and ^{40}K decays within the Earth are responsible for the majority of the current radiogenic heat production. These decays also produce $\bar{\nu}_{\mathrm{e}}$'s, the vast majority of which reach the Earth's surface since neutrinos hardly interact with matter, allowing a direct measure of total Earth radiogenic heat production by these isotopes.

Kamioka Liquid scintillator Anti-Neutrino Detector (KamLAND) detects $\bar{\nu}_{\mathrm{e}}$'s by neutron inverse β decay and is large enough to detect these geological neutrinos. Due to the neutron inverse β decay threshold, KamLAND can only observe $\bar{\nu}_{\mathrm{e}}$'s from ^{238}U and ^{232}Th decay.

1.1 Structure and composition of the Earth

Models based on seismic data divide the Earth into three basic regions: the core, mantle, and crust. As shown in Figure 1.1 these regions are further subdivided into a inner core, outer core, lower mantle, transition zone, upper mantle, continental crust, and oceanic crust. Table 1.1 shows the contribution of each region to the overall mass of the Earth.

All regions are solid except for the liquid outer core and the upper mantle, which

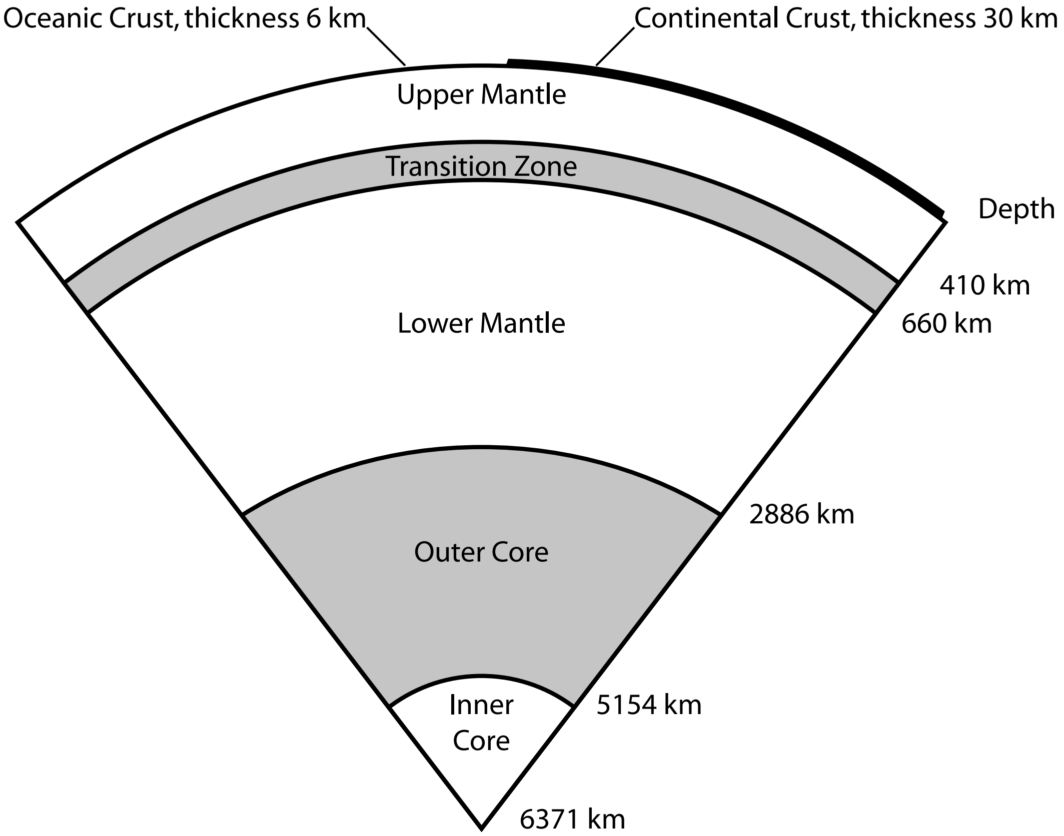

Figure 1.1: Radial distribution of the major Earth regions as determined by seismic data. Modified from Schubert[3].

Region	Depth Range [km]	Mass [10^{21} kg]	Mass Fraction [%]	Average Density [$\mathrm{kg\,m^{-3}}$]
Oceanic crust	0-6	6	0.1	3,100
Continental crust	0-30	19	0.3	2,700
Upper mantle	(6,30)-410	615	10.3	3,350
Transition zone	410-660	415	7.0	3,860
Lower mantle	660-2,886	2,955	49.6	4,870
Outer core	2,886-5,140	1,867	31.1	11,000
Inner core	5,140-6,371	98	1.6	12,950
Whole Earth	0-6,371	5,975	100	5,515

Table 1.1: Mass and density of the major Earth regions. Modified from Schubert[3].

Region	U		Th		K	
	[ppb]	[10^{16} kg]	[ppb]	[10^{16} kg]	[ppm]	[10^{20} kg]
Oceanic crust[5]	100	0.06	220	0.13	1250	0.08
Continental crust[6]	1400	2.66	5600	10.64	15600	2.96
Mantle	13.6	5.42	53.0	21.11	165	6.58
BSE[7]	20.3	8.14	79.5	31.88	240	9.62

Table 1.2: Estimated concentration and mass of U, Th, and K in the major Earth regions. The mass of radiogenic elements in the mantle is obtained from the difference between the BSE and crust.

may contain partial melts. The transition zone is thought to represent a pressure induced phase transition. Two very different[3] types of crust, Continental and Oceanic, cover ∼40 % and ∼60 % of the Earth's surface, respectively. Continuous renewal of the oceanic crust at mid ocean ridges and recycling at subduction zones make the oceanic crust remarkably homogenous and relatively young, on average only ∼ 80 Myr old. By contrast, the continental crust is variable and much older, on average ∼ 2,000 Myr old.

The regional composition of the Earth is determined by a number of different methods. The deepest hole ever dug penetrates 12 km of the crust[4], allowing direct sampling from only a small fraction of the Earth. Lava flows bring xenoliths, foreign crystals in igneous rock, from the upper mantle to the surface. Physical properties determined from seismic data can be compared to laboratory measurements. Our current knowledge suggests that the crust and mantle are composed mainly of silica, with the crust enriched in U, Th, K. The core is composed mainly of Fe but includes a small fraction of lighter elements. Table 1.2 shows the estimated concentration of U, Th, and K in the different Earth regions.

It is believed that the solar system formed from a cloud of rotating gas and dust, solar nebula, as it condensed onto the median plane ∼ 4500 Myr ago[8]. During and following solar nebula condensation, solid particles were assembled by accretionary processes into larger lumps. This took less than ∼ 100 Myr, eventually forming the planets and astroid belt[9]. This formation released significant heat and lead to the complete melting of the outer part of the Earth. Lumps of Fe would have formed and moved to the center of the Earth due to it's higher density, forming the core. The mantle would have crystallized outward from the core-mantle boundary which explains why the crust is enriched in U, Th, and K, since they preferentially enter an available melt phase. Heat loss at the surface resulted in a thin crustal surface. This crust would have been repeatedly modified by large meteoritic impacts and eventual formed the current continental crust. U, Th, and K have continued to enter the crust in igneous rocks throughout the Earth's history, and subduction has returned some fraction to the Mantle.

The chemical composition of the Sun's outer layer, solar abundance, can be measured from the light absorption spectra of the chemical elements. This produces similar abundances to those measured in primitive undifferentiated meteorites such as type I carbonaceous chondrites[10]. The composition of non-volatile elements in the Earth should be similar to the solar abundance since they formed in the same process. Models[7] based on the solar abundance data establish the composition of the undifferentiated mantle in the early formation stage of the Earth, referred to as "Bulk Silicate Earth" (BSE). Table 1.2 includes the estimated concentration of U, Th, and K in the BSE. The ratio of Th/U, between 3.7 and 4.1, is known better than the total abundance[11].

1.2 Thermodynamics of the Earth

The rate of radiogenic heat released from U, Th, and K decays are $98.1\,\mu\mathrm{W\,kg^{-1}}$, $26.4\,\mu\mathrm{W\,kg^{-1}}$, and $0.0035\,\mu\mathrm{W\,kg^{-1}}$[3], respectively. Table 1.3 summarizes the total radiogenic heat production rate in the Earth regions based on the mass of these elements given in Table 1.2. The rate of mantle heating due to lunar tides is a negligible $\sim 0.12\,\mathrm{TW}$[12].

The radiogenic heat production within the Earth can be compared to the measured heat dissipation rate per unit area at the surface, q_o. Assuming only conductive heat loss near the surface, q_o is given by

$$q_o = -k\frac{\partial T}{\partial r}, \tag{1.1}$$

Region	U [TW]	Th [TW]	K [TW]	Total [TW]
Oceanic crust	0.06	0.03	0.03	0.12
Continental crust	2.61	2.81	1.04	6.46
Mantle	5.32	5.57	2.30	13.19
BSE	7.99	8.42	3.37	19.78

Table 1.3: Radiogenic heat production rate in different Earth regions.

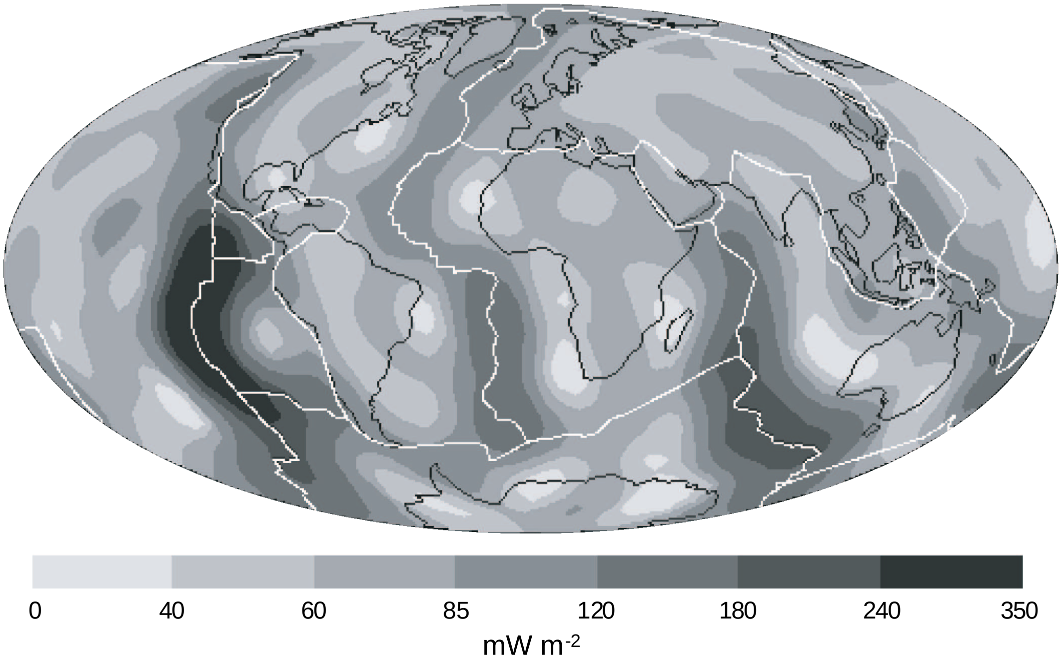

Figure 1.2: Map of conductive heat dissipation rate. Modified from Pollack[13]. Black lines represent land masses, white lines represent continental plate margins.

where k is the thermal conductivity, T is the temperature, and r is the depth. Table 1.4 and Figure 1.2 show the estimated heat dissipation rate from the Earth based on a review[13] of q_o measured at 20,201 sites. The majority of the heat is lost through the oceanic crust, despite the fact that the continental crust contains the majority of the radiogenic heat producing elements.

The Urey ratio, the ratio between mantle heat dissipation and production, indicates what fraction of the current cooling is due to primordial heat. Subtracting the

Region	Heat Dissipation Rate $[\mathrm{W\,m^{-2}}]$	Area $[\mathrm{m^2}]$	Global Heat Dissipation Rate [TW]
Oceanic crust	$101 \pm 2.2 \times 10^{-3}$	3.1×10^{14}	31.2 ± 0.7
Continental crust	$65 \pm 1.6 \times 10^{-3}$	2.0×10^{14}	13.0 ± 0.3
Whole Earth	$87 \pm 2.0 \times 10^{-3}$	5.1×10^{14}	44.2 ± 1.0

Table 1.4: Crustal conductive heat dissipation rate.

continental crust heat production rate of 6.5 TW, the mantle is dissipating heat at a rate of 37.7 TW and generating heat at a rate of 13.3 TW, giving a Urey ratio of ∼0.35. It is widely believed that the mantle convects although the exact nature of that convection is still unclear. Models of mantel convection give Urey ratios greater than ∼0.69[14, 15, 16], which is inconsistent with the value obtained from heat considerations. A direct measurement of the terrestrial radiogenic heat production rate would help our understanding of this apparent inconsistency.

1.3 Terrestrial $\bar{\nu}_\mathrm{e}$ signal

Each of the ^{238}U, ^{232}Th, and ^{40}K decay chains[17], shown in Figure 1.3, produces at least one $\bar{\nu}_\mathrm{e}$ since they all contain at least one β^- decay. Since β^- decay is a three body decay, the kinetic energy of the $\bar{\nu}_\mathrm{e}$'s, E_ν, has a continuum spectrum up to the decay endpoint energy, E_o. The energy spectrum is given by[18]

$$\frac{dN}{dE_\nu} = C p_e W_e E_\nu^2 F(Z, W_e), \tag{1.2}$$

where C is the normalization constant, $p_e = (E_o - E_\nu)^{1/2}(E_o - E_\nu + 2m_e)^{1/2}$ is the electron momentum, $W_e = E_o - E_\nu + m_e$ is the electron total energy, m_e is the electron mass, $F(Z, W_e)$ is the Fermi-function taking into account the distortion of the electron wave function by the nuclear charge, and Z is the charge of the daughter

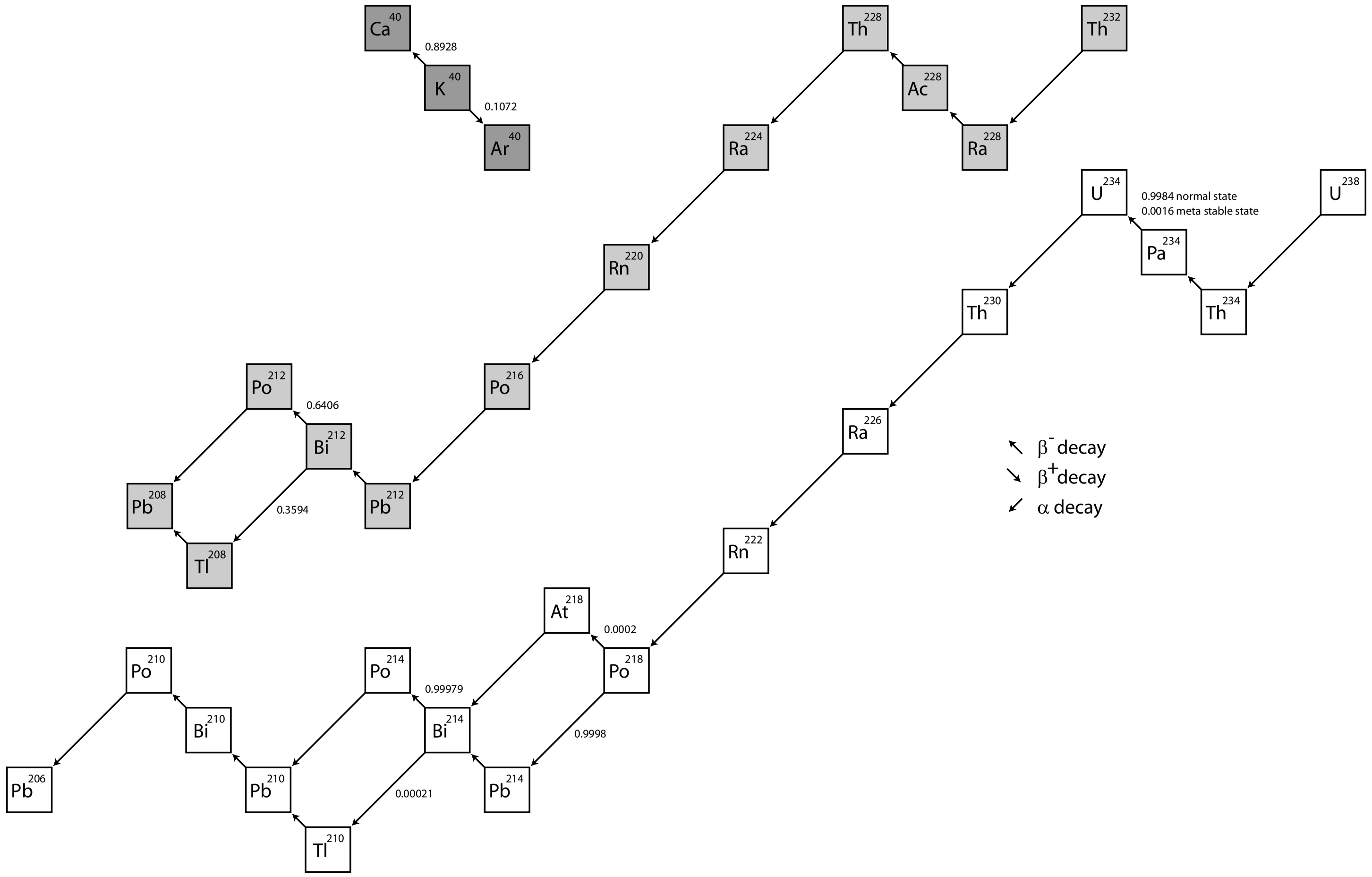

Figure 1.3: ^{238}U, ^{232}Th, and ^{40}K decay chain.

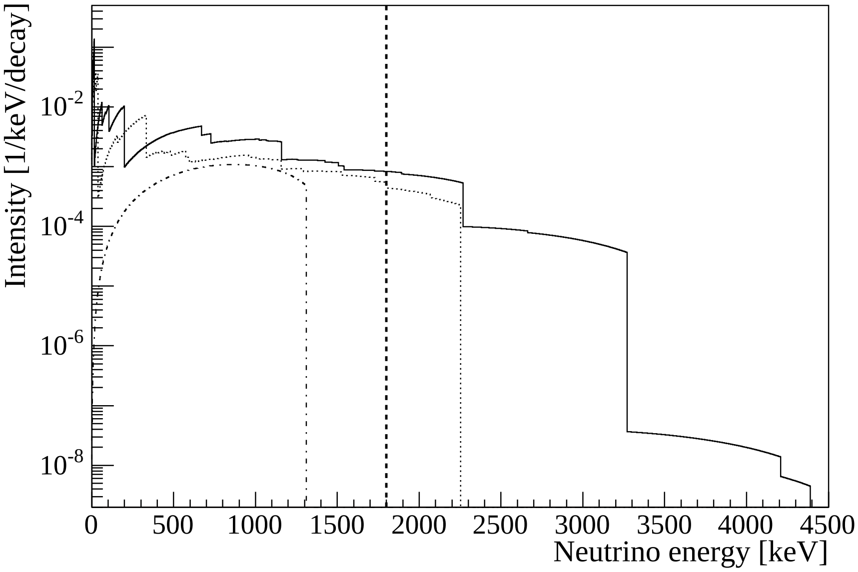

Figure 1.4: The $\bar{\nu}_{\rm e}$ energy distributions for the ^{238}U (solid), ^{232}Th(dash), and ^{40}K(dot-dash) decay chains. The vertical line represents the $\bar{\nu}_{\rm e}$ detection threshold at KamLAND, described in Section 1.5.

nucleus. $F(Z, W_e)$ is normally written as the product

$$F = F_o L_o, \tag{1.3}$$

where L_o is the nucleus finite charge distribution correction obtained from numerical calculations[19], and F_o is the solution of the Dirac equation for a point charge nucleus evaluated at the nuclear radius, $R = 1.2\,\mathrm{fm} \times A^{1/3}$, given by

$$F_o = 4\left(\frac{2p_eR}{\hbar}\right)^{2\gamma-2}\exp(\pi\eta)\frac{|\Gamma(\gamma+i\eta)|^2}{|\Gamma(2\gamma+1)|^2}, \tag{1.4}$$

where $\eta = \alpha Z W_e/p_e$, $\gamma = [1-(\alpha Z)^2]^{1/2}$, and $\alpha = 1/137.0388$.

Figure 1.4 shows the $\bar{\nu}_{\rm e}$ energy distributions, $\frac{dn}{dE_\nu}$, for the ^{238}U, ^{232}Th, and ^{40}K decay chains, based on Equation 1.2, and the endpoint energies and branching ratios[17].

1.4 Neutrino oscillations

Three neutrino flavors have now been observed, associated with electron, muon, and tau weak interactions. These three weak interaction neutrino eigenstates, $|\nu_\ell\rangle$, may be superpositions of definite mass eigenstates $|\nu_i\rangle$[20],

$$|\nu_\ell\rangle = \sum_{i=1}^{3} U_{\ell i}|\nu_i\rangle, \tag{1.5}$$

where U is a mixing matrix parameterized by three angles: θ_{12}, θ_{13}, and θ_{23}, a CP violating phase, δ, and two Majorana phases: α_1 and α_2.

The mass eigenstates evolve independently in time according to the Schroedinger equation. This changes the probability of the neutrino being found in a given flavor eigenstate as a function of distance travelled, a phenomenon usually referred to as "neutrino oscillations". In the ultra-relativistic neutrino limit, the probability of finding flavor ℓ' at distance L, after starting with a neutrino of flavor ℓ, is given by

$$P(\nu_\ell \to \nu_{\ell'}) = \sum_i |U_{\ell i}U^*_{\ell' i}|^2 + \Re\left(\sum_i \sum_{j\neq i} U_{\ell i}U^*_{\ell' i}U^*_{\ell j}U_{\ell' j}e^{i\frac{\Delta m^2_{ij}L}{2E_\nu}}\right), \tag{1.6}$$

where $\Delta m^2_{ij} = \left|m^2_i - m^2_j\right|$, m_i is the mass of the ith mass eigenstate, and E_ν is the neutrino energy. Because $\Delta m^2_{12} \gg \Delta m^2_{32}$[21, 22], and there is very little mixing between the 1 and 3 mass states[23], the electron neutrino survival probability can be approximated as,

$$P(E_\nu, L) = 1 - \sin^2 2\theta_{12}\sin^2\left(\frac{1.27\Delta m^2_{12}[\mathrm{eV}^2]L[\mathrm{m}]}{E_\nu[\mathrm{MeV}]}\right), \tag{1.7}$$

where $\Delta m^2_{12} = 7.9^{+0.6}_{-0.5} \times 10^{-5}\,\mathrm{eV}^2$, and $\sin^2 2\theta_{12} = 0.816^{+0.073}_{-0.070}$[21].

The neutrino oscillations discussed so far are vacuum oscillations. Neutrino scattering in matter changes the phase of the neutrino flavors. Since neutral current scattering affects all three neutrino flavors, it does not change the relative phase of the neutrino flavors. However, charged current scattering only affects electron neutrinos, changing their phase with respect to the other neutrino flavors. The distance over which the electron neutrino phase changes by 2π is

$$L_m = \frac{2\pi}{\sqrt{2} G_F N_e}, \tag{1.8}$$

where G_F is the Fermi constant, and N_e is the matter electron density. For ordinary rock with a density of $3\,\mathrm{g\,cm^{-3}}$, $L_m \sim 10^4\,\mathrm{km}$. This is much greater than the typical oscillation lengths for the $\bar{\nu}_\mathrm{e}$'s from the Earth detected with KamLAND, so it does not significantly modify the oscillation probability in Equation 1.7.

1.5 $\bar{\nu}_\mathrm{e}$ detection with KamLAND

KamLAND detects $\bar{\nu}_\mathrm{e}$'s by neutron inverse β decay,

$$\bar{\nu}_\mathrm{e} + \mathrm{p} \longrightarrow \mathrm{e}^+ + \mathrm{n}. \tag{1.9}$$

The positron, e^+, almost immediately deposits its kinetic energy, then annihilates with an electron producing two γ-rays. KamLAND detects this as a single event, referred to as the "prompt event". The neutron, n, first thermalizes, then is captured by a proton with a mean capture time of $\sim 200\,\mu\mathrm{s}$. KamLAND detects the 2.2 MeV γ-ray produced in this capture, referred to as the "delayed event". The space and time coincidence between the prompt and delayed events, coupled with the well-defined energy of the delayed event, results in a signature clearly distinguishable from most backgrounds.

To zeroth order in 1/M, where M is the nucleon mass, the total positron energy, $W_e^{(0)}$, is related to the total neutrino energy, W_ν, by

$$W_e^{(0)} = W_\nu - m_n + m_p, \tag{1.10}$$

where m_n and m_p are the neutron and proton masses, respectively. The neutron inverse β decay reaction has a threshold $\bar{\nu}_\mathrm{e}$ energy of 1.8 MeV. Therefore KamLAND can not observe the $^{40}\mathrm{K}$ $\bar{\nu}_\mathrm{e}$'s since their endpoint is less than the 1.8 MeV detection threshold, as shown in Figure 1.4.

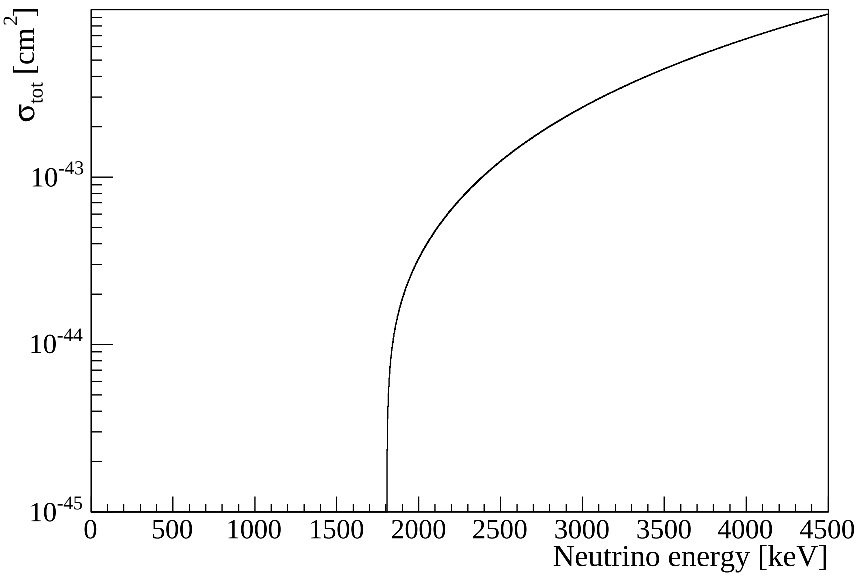

Figure 1.5: The neutron inverse β decay cross-section for the terrestrial $\bar{\nu}_{\mathrm{e}}$ energy range.

To zeroth order in 1/M, the neutron inverse β decay cross-section[24] is given by

$$\sigma_{tot}^{(0)} = 0.0952 \left(\frac{W_e^{(0)} p_e^{(0)}}{1\,\mathrm{MeV}^2} \right) \times 10^{-42}\,\mathrm{cm}^2, \tag{1.11}$$

where $p_e = \sqrt{{W_e}^2 - m_e^2}$ is the positron momentum. Figure 1.5 shows the cross-section as a function of W_ν. Including first order corrections and radiative corrections[25] the total error on this cross section is estimated to be 0.2 %[26].

1.6 Expected terrestrial $\bar{\nu}_{\mathrm{e}}$ signal with KamLAND

As a function of energy the estimated neutron inverse β decay rate per target proton in KamLAND due to terrestrial ^{238}U or ^{232}Th is given by

$$\frac{d\Phi}{dE_\nu}(E_\nu) = A \frac{dn}{dE_\nu}(E_\nu)\,\sigma(E_\nu) \int_\oplus d\mathbf{L}\, \frac{a(\mathbf{L})\rho(\mathbf{L})P(E_\nu, |\mathbf{L}|)}{4\pi|\mathbf{L}|^2}, \tag{1.12}$$

where $A = 1.24 \times 10^7\,\mathrm{s}^{-1}\mathrm{kg}^{-1}$ $(0.41 \times 10^7\,\mathrm{s}^{-1}\mathrm{kg}^{-1})$ is the ^{238}U (^{232}Th) decay rate per unit mass, $\frac{dn}{dE_\nu}(E_\nu)$ is the $\bar{\nu}_\mathrm{e}$ energy distribution, shown in Figure 1.4, $\sigma(E_\nu)$ is the neutron inverse β decay cross-section given in Section 1.5, $\mathbf{L}$ is the position relative to the detector, $a(\mathbf{L})$ is the isotope mass per unit rock mass, $\rho(\mathbf{L})$ is the density, $P(E_\nu, |\mathbf{L}|)$ is the $\bar{\nu}_\mathrm{e}$ survival probability due to neutrino oscillations discussed in Section 1.4, and the integral is over the volume of the Earth.

Equation 1.12 can be rewritten as

$$\frac{d\Phi}{dE_\nu}(E_\nu) = A\frac{dn}{dE_\nu}(E_\nu)\,\sigma(E_\nu)\Delta(E_\nu)\int_\oplus d\mathbf{L}\,\frac{a(\mathbf{L})\rho(\mathbf{L})}{4\pi|\mathbf{L}|^2}, \tag{1.13}$$

where $\Delta(E_\nu)$ is an oscillation dependent energy correction given by

$$\Delta(E_\nu) = \int_\oplus d\mathbf{L}\,\frac{a(\mathbf{L})\rho(\mathbf{L})P(E_\nu, |\mathbf{L}|)}{4\pi|\mathbf{L}|^2} \Bigg/ \int_\oplus d\mathbf{L}\,\frac{a(\mathbf{L})\rho(\mathbf{L})}{4\pi|\mathbf{L}|^2}\ . \tag{1.14}$$

Figure 1.6 shows $\Delta(E_\nu)$ calculated for terrestrial ^{238}U given the neutrino survival probability in Equation 1.7, and the Earth model given in Section 1.1 assuming KamLAND is on the boundary of oceanic and continental crusts. Since there is not much variation in $\Delta(E_\nu)$, the expected observed energy spectrum is proportional to $\frac{dn}{dE_\nu}(E_\nu)\,\sigma(E_\nu)$, shown in Figure 1.7.

Based on a detailed simulation[27], including seismic models of crustal thickness and type, the number of neutron inverse β decays in KamLAND due to terrestrial ^{238}U and ^{232}Th is estimated[1] to be 29 ± 5 and 7 ± 1 per 10^{32} target protons per year, with a total of 36 ± 6 per 10^{32} target protons per year, respectively. This can be compared to a total of 27 per 10^{32} target protons per year obtained from the simple Earth model presented in Section 1.1 and assuming KamLAND is on the boundary of continental and oceanic crust.

---

[1] The numbers are modified for $\sin^2 2\theta_{12} = 0.816$ instead of $\sin^2 2\theta_{12} = 0.863$ as used in ref.[27].

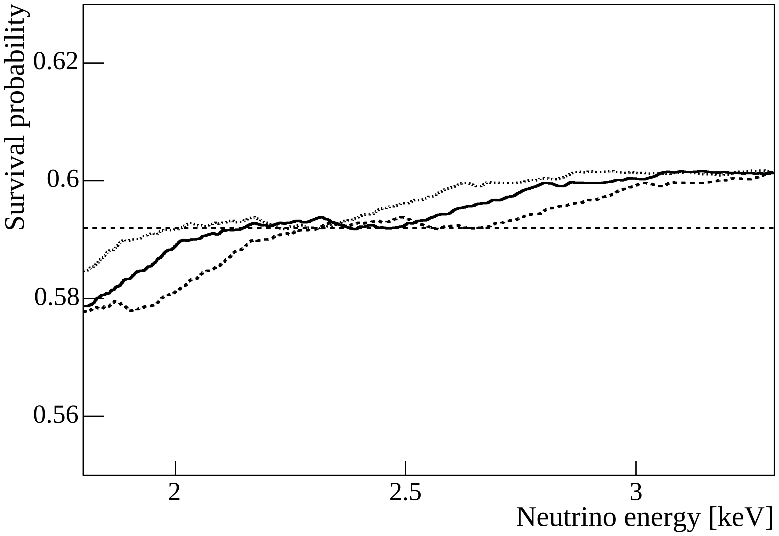

Figure 1.6: Correction to the expected ^{238}U $\bar{\nu}_e$ energy spectrum due to neutrino oscillations for $\sin^2 2\theta_{12} = 0.816$ and $\Delta m^2_{12} = 7.9 \times 10^{-5}\,\mathrm{eV}^2$ (solid), $\Delta m^2_{12} = 8.5 \times 10^{-5}\,\mathrm{eV}^2$ (dash), and $\Delta m^2_{12} = 7.4 \times 10^{-5}\,\mathrm{eV}^2$ (dot). The horizontal line shows the correction assuming $\sin^2\left(\frac{1.27\Delta m^2_{12}|\mathbf{L}|}{E_\nu}\right) = 0.5$.

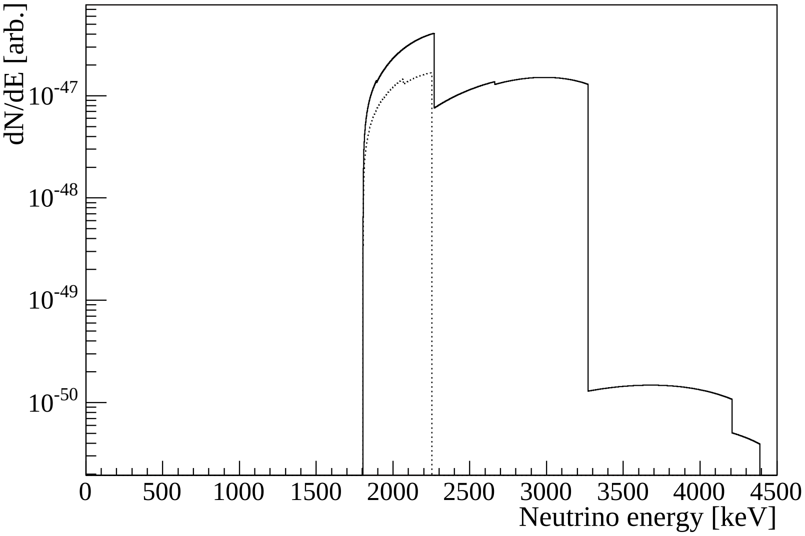

Figure 1.7: The expected $\bar{\nu}_e$ energy distribution observed with KamLAND for the ^{238}U (solid) and ^{232}Th (dash) decay chains.

Chapter 2

Detector and electronics

KamLAND is located in Kamioka mine, Gifu prefecture, Japan (36.42°N, 137.31°E). It was built and commissioned between 1998 and 2002 primarily to study neutrino oscillations by observing $\bar{\nu}_{\mathrm{e}}$'s from the nuclear power plants surrounding the detector; it is also sensitive to $\bar{\nu}_{\mathrm{e}}$'s from ^{238}U and ^{232}Th decay in the Earth.

Figure 2.1 shows a schematic of KamLAND. There are two major components: the Inner Detector (ID) and Outer Detector (OD). The ID consists of $\sim 1\,\mathrm{kton}$ of liquid scintillator housed in an approximately spherical balloon of radius $\sim 6.5\,\mathrm{m}$. This is surrounded by a steel sphere of radius $\sim 9\,\mathrm{m}$. The volume between the steel sphere and the balloon is filled with a non-scintillating buffer oil. The scintillation light is detected with Photo Multiplier Tubes (PMT's) which are mounted inside the steel sphere. The OD, used as a water-Cherenkov cosmic ray veto, is confined from the outside by the cylindrical rock cavern and from the inside by the steel sphere.

As shown in Figure 2.2, the output signals from the PMT's are connected to the Front-End Electronics (FEE), which record each PMTs' voltage as a function of time. This voltage as a function of time is refereed to as a waveform. The MACRO electronics[1], described in Appendix B, provide a redundant system for recording the PMT waveforms. The trigger module makes the decision to record the PMT waveforms, based on how many tubes have detected at least one photon in the last 125 ns.

---

[1] The MACRO electronics were originally designed for the Monopole, Astrophysics and Cosmic Ray Observatory (MACRO) at Gran Sasso and were installed in KamLAND after the decommissioning of MACRO.

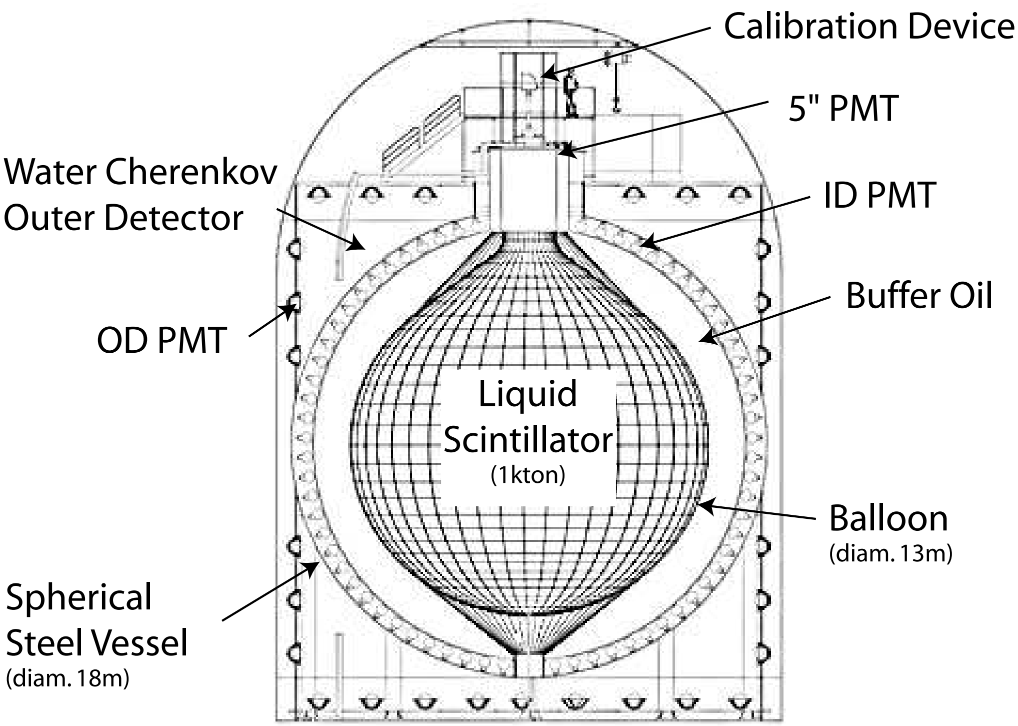

Figure 2.1: Schematic diagram of the KamLAND detector.

The Data Acquisition (DAQ), described in Appendix E, asynchronously receives and records data from the FEE, MACRO electronics, and trigger module, and communicates the run parameters to these systems.

2.1 Inner detector

A network of Kevlar ropes supports and constrains the balloon. The balloon is made of 135 μm thick transparent nylon/EVOH (ethylene vinly alcohol) copolymer composite film. The balloon is filled with liquid scintillator which consists of 80 % dodecane, 20 % pseudocumene (1,2,4-trimethylebenzene), and 1.52 g ℓ^{-1} of PPO (2,5-diphenyloxazole) as a fluor. The scintillator converts the kinetic energy of charged particles into visible photons with a typical wavelength of ~350-400 nm. The total number of visible photons produced is proportional to the kinetic energy of the particle; there are some corrections to this proportionality, discussed in Section 3.5. A mixture of dodecane and isoparaffin oils (buffer oil) between the balloon and the steel sphere shields the liquid scintillator from external radiation, particularly from the PMT glass. The buffer oil is 0.04 % less dense than the liquid scintillator, and provides buoyancy to the balloon so that the ropes only have to support ∼600 kg.

The highest purity oil commercially available has U, Th, and ^{40}K concentrations of about 10^{-13} g/g each. In order to reduce the backgrounds from these isotopes the liquid scintillator and buffer oil were purified by water extraction and nitrogen stripping[28] during the filling. U, Th, and K metal ions are more soluble in water than oil or pseudocumene. Water extraction works by mixing the oil and pseudocumene with pure water which preferentially absorbs the metal ions. Because the scintillator and buffer oil do not dissolve in water, these can be easily separated from the water after mixing. The small amount of water remaining in the liquid scintillator and buffer oil after the water extraction is removed by passing dry nitrogen though the mixture. After this purification the measured U, Th, and ^{40}K concentrations in the scintillator are less than 6×10^{-16} g/g, 2×10^{-16} g/g, and 2×10^{-16} g/g, respectively.

The steel sphere is covered with 1325 new Hamamatsu R7250 17" PMT's and 554 20" PMT's refurbished from Kamiokande[2]. There are also six 5" PMT's attached to the top of the ID pointing downward. In the analysis presented here, only the 17" PMT's are used, which provides a photo-cathode coverage of 22 %. The PMT's are operated with a gain of 10^7, which results in a ∼ 22 % efficiency for converting a 480 nm incident photon into a Photo Electron (PE). The typical time resolution of these 17" PMT's is ∼3 ns. A set of compensation coils surrounding the detector reduces the terrestrial magnetic field of ∼350 mGauss at the KamLAND site to a value well below the 50 mGauss required for proper operation of the PMT's.

2.2 Outer detector

The OD consists of a 3.2 kton water-Cherenkov detector with 225 20" PMT's, surrounding the ID. The OD is used to tag cosmic-ray muons which produce visible

---

[2] Kamiokande was a water cherenkov detector located in the cavern now occupied by KamLAND.

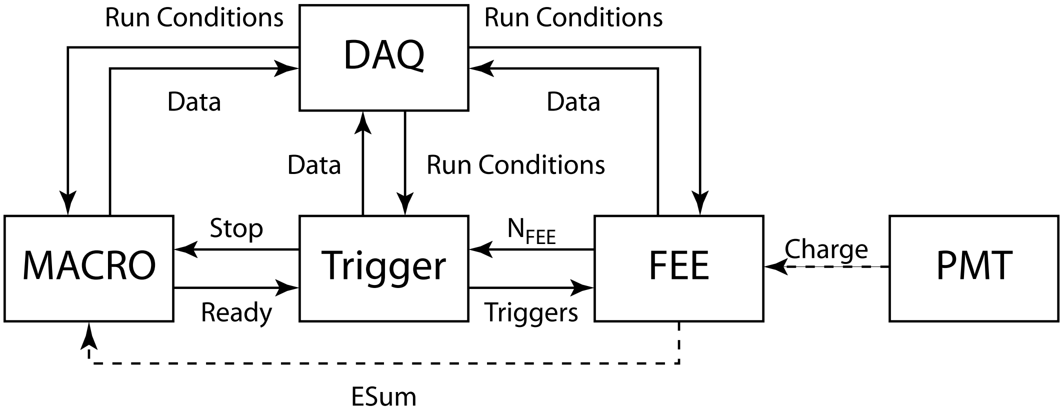

Figure 2.2: An overview of the main electronics components and the communication among them. Solid and dashed lines are digital and analog communications, respectively.

photons in a cone along their path via Cherenkov radiation. Muons are identified by their high light yield since the presence of the ID obstructs the radiation cones in the OD, limiting the ability to reconstruct the cone. The OD also acts as a buffer for the ID, absorbing γ-rays and neutrons from surrounding rocks.

The OD consists of four optically isolated sections: the top, upper, lower, and bottom sections. The top and bottom sections have PMT's attached in concentric circles to the ceiling and floor of the detector, respectively. The upper and lower sections have PMT's attached uniformly to the side of the detector above and below the equator, respectively. Optical isolation is obtained with reflective Tyvek®[3] sheets, which are also placed on all surfaces to increase the overall efficiency for the collection of optical photons. The water in the OD is being constantly circulated, which controls the temperature of the ID by removing excess heat.

2.3 Front-end electronics

The FEE uses a VME bus for data transfer and is arranged as 9U VME modules, each of which has 12 PMT inputs. Each input channel has a separate discriminator, with a threshold that can be set by the DAQ. The waveforms are recorded on Analogue

---

[3] DuPont Tyvek® is a lightweight yet strong material.

Transient Waveform Digitizers (ATWD's). These are self launching; acquiring the waveform only when it goes above the discriminator threshold. In order to record the start of any waveform signal, the input to the ATWD is delayed with respect to the discriminator logic.

Each ATWD can simultaneously acquire four 128-sample-long waveforms. At the start of each run, the DAQ sets the sampling time, which can vary between approximately 1 and 3 ns per sample. During normal data taking, the sampling time is $\sim$1.6ns per sample, corresponding to $\sim$200 ns-long waveforms. The signal from the PMT is connected to three different amplifiers with high($\times$20), medium($\times$4), and low($\times$0.5) gains. The output from these are connected to three of the ATWD inputs. This allows the FEE to record a broad range of signals from a single PE with an amplitude as small as $\sim$0.7 mV to signals as large as 1 V from a muon. The fourth input to the ATWD is connected to a 25 ns sinusoidal clock signal. The sampling time can be calibrated from the known frequency of this clock input.

The ATWD's digitize the acquired waveforms with a 10-bit ADC when the FEE receives a command to digitize. Appendix A contains a complete list of the commands and their correspond FEE behaviors. If the FEE receives no global acquisition command within a fixed number of clock-ticks from the completion of acquiring a waveform, the acquisition hold time, then the waveform is erased, and the ATWD is free to record another waveform. For normal data taking the acquisition hold time is 7 clock-ticks, or 175 ns, sufficient to record the earliest light associated with an event.

The trigger module distributes a 40 MHz clock signal to every FEE module, which has a scaler to record the number of clock-ticks, called the timestamp. The timestamp is reset when the FEE module receives a reset timestamp command; see Appendix A. The timestamp is recorded for each waveform and is used to associate waveforms. The FEE also records the number of 40 MHz clock-ticks that elapsed between the times when a channel starts acquiring a waveform and receives a command to digitize the waveform; called the launch offset. Figure 2.3 shows an example schematic of the timing for acquiring and digitizing waveforms. In this example, the FEE modules receive the global acquisition command at the N^{th} clock-tick; this is recorded as the timestamp. Channel 1 goes above threshold and starts acquiring from the N-13^{th}

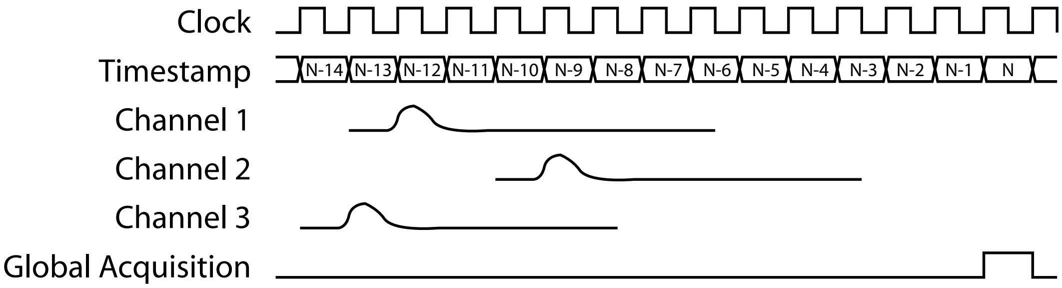

Figure 2.3: Schematic of the FEE waveform acquisition and digitization timing.

clock-tick; the total acquire time is just under 200 ns. Similarly Channel 2 starts acquiring a waveform from the N-10th clock-tick. The launch offsets for Channel 1 and 2 are 13 and 10, respectively. Note that Channel 3 is not recorded because it finished acquiring longer than the acquisition hold time of 7 clock-ticks before the global acquisition command.

One waveform with timestamp, launch offset, and other identification information is recorded as a 256 byte block of data. Each board has 32 MB of memory, corresponding to ~130,000 waveforms. This is useful for collecting short bursts of data, such as that expected from a nearby Supernova, see Appendix D. However, due to limitations in the DAQ throughput, the maximum sustained rate is a total of ~20,000 waveforms per second.

After an ATWD acquires a waveform, it takes $\sim 1\,\mu$s to clear before becoming capable to acquire another waveform and $\sim 30\,\mu$s to digitize one waveform. Each channel acquires waveforms at a rate of between 50 and 150 kHz and digitizes waveforms at a rate of ~5 Hz. To reduce dead-time, two ATWD's, ATWD A and ATWD B, are connected to each channel; when one ATWD is dead, the other can acquire a waveform.

2.4 Trigger module

The trigger module distributes a 40 MHz clock to all FEE modules, keeping them synchronized with the trigger module. Every clock-tick the trigger module receives the number of PMT's connected to each FEE module with a signal above the channel's discriminator level in the last 125 ns, $\mathrm{N_{FEE}}$. The trigger module then sums $\mathrm{N_{FEE}}$'s from FEE modules connected to ID 17" ($\mathrm{N_{ID}}$), OD top ($\mathrm{N_{ODtop}}$), OD upper ($\mathrm{N_{ODupper}}$), OD lower ($\mathrm{N_{ODlower}}$), OD bottom ($\mathrm{N_{ODbottom}}$), and 5" ($\mathrm{N_{5"}}$) PMT's. Based on these sums, the trigger module must issue a global acquisition command to the FEE within ∼400ns in order for the ATWD's to digitize the waveforms. When the trigger module issues this command a trigger record stores: the timestamp, trigger type (see Table C.1), $\mathrm{N_{ID}}$, $\mathrm{N_{ODtop}}$, $\mathrm{N_{ODupper}}$, $\mathrm{N_{ODlower}}$, $\mathrm{N_{ODbottom}}$, and $\mathrm{N_{5"}}$. This timestamp is the same as that recorded by the FEE modules, allowing waveforms to be associated with the trigger record. Trigger records are simply called "triggers". Not all triggers are necessarily associated with issuing a command to the FEE. Appendix C gives a detailed description of how the trigger module works along with a description of all the different trigger types. This includes a discussion of a trigger to detect a nearby supernova explosion, and how the absolute time is recorded, which is important to compare supernova events at different detectors.

Chapter 3

Event reconstruction and calibration

As described in Chapter 2, KamLAND is a liquid scintillator detector surrounded by 1325 17" PMT's. The PMT's detect scintillation light produced by ionizing particles and produce waveforms which are recorded by the FEE's. This chapter describes how the ionizing particle's location and energy are reconstructed from the waveforms.

3.1 Calibration sources

Radioactive sources with known energies and positions are used to tune the energy and position reconstruction algorithms. A "z-axis" calibration system deploys encapsulated sources at different heights down the center of the detector. The following sources are available for deployment:

- ^{60}Co, which produces correlated 1.173 MeV and 1.332 MeV γ's.
- ^{68}Ge, which produces an e^+ that annihilates with an e^- in the capsule, producing two correlated 0.511 MeV γ's.
- ^{65}Zn, which produces a 1.116 MeV γ.
- ^{203}Hg, which produces a 0.279 MeV γ.

- ^{241}Am^{9}Be , which produces either a neutron, n_0, a neutron and a 4.43 MeV γ, n_1, or a neutron and a 7.65 MeV γ, n_2. With a mean time of $\sim 200\,\mu$s these neutrons are then captured by ^{1}H or ^{12}C producing a 2.223 MeV γ or 4.945 MeV γ, respectively. Capture on ^{12}C is substantially less common than on ^{1}H because of the smaller cross-section and lower concentration of C atoms.

As well as the radioactive sources above, radioactive backgrounds in the detector, on the balloon surface, and those produced after muons are used for calibration.

3.2 Event data association

As described in Chapter 2, waveforms and trigger records are collected asynchronously. An off-line event-builder associates waveforms and trigger records with the same timestamp into a single event. During normal operation, ID, OD top, OD upper, OD lower, and OD bottom history triggers, described in Section C.2.4, with thresholds of 120, 6, 5, 6, and 7, respectively, are enabled. This results in a series of history triggers from consecutive 40 MHz clock-ticks, history trigger train. $\mathrm{NMax_{ID}}$ is the maximum $\mathrm{N_{ID}}$ in a history trigger train. $\mathrm{NMax_{OD}}$ is the sum of the maximum of $\mathrm{N_{ODtop}}$, $\mathrm{N_{ODupper}}$, $\mathrm{N_{ODlower}}$, and $\mathrm{N_{ODbottom}}$ in a history trigger train. $\mathrm{NMax_{ID}}$ and $\mathrm{NMax_{OD}}$ are associated with the other triggers occurring during a history trigger train.

3.3 Pulse arrival time and number of photo electrons

For all events analyzed here, other than muons, the waveforms typically have one or a few PE's per PMT. The following algorithm to calculate the pulses arrival times and number of PE's is used for all events except muons. The arrival times of pulses are calculated from waveforms after removing the fixed channel-to-channel fluctuations in each ATWD, referred to as “ATWD fluctuation”, removing the pedestal, and smoothing. The pedestal is the waveform offset from zero without any PMT signal.

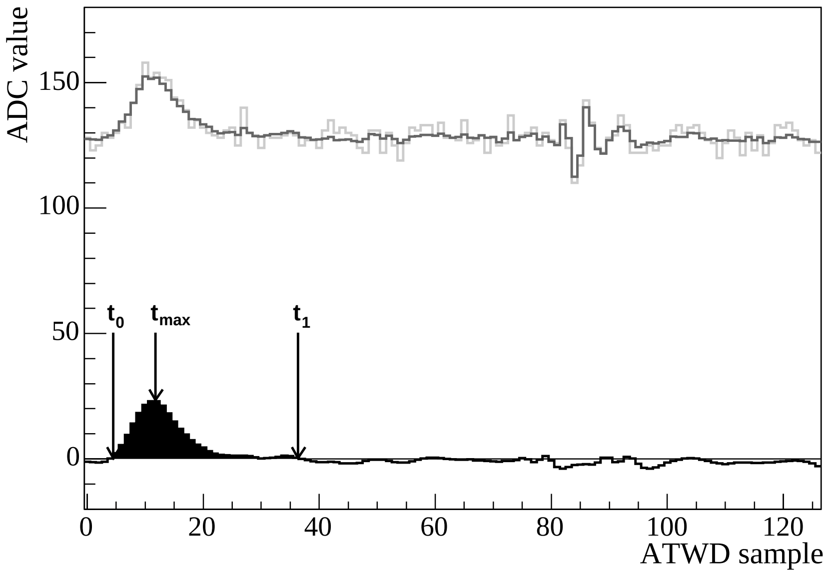

Figure 3.1: A typical waveform(light grey line), "ATWD fluctuation" subtracted waveform (dark grey line), and corrected waveform (black line). The filled black region represents the only pulse found in this waveform. t_0 and t_1 represent the start and end time of the pulse, respectively. t_{max} represents the time when the pulse amplitude is maximum.

At the start of each run 50 waveforms are collected from each ATWD at a fixed frequency. The pedestal is subtracted before averaging the waveforms without random PE's to produce the "ATWD fluctuation" for each ATWD. The "ATWD fluctuation" is then subtracted from all waveforms collected from that ATWD throughout the run. Figure 3.1 shows a typical waveform and "ATWD fluctuation" subtracted waveform which is smoother.

The pedestal is calculated by ordering the samples from largest to smallest and removing the extrema until the two extrema are the same "distance" away from the average of the remaining samples within an accuracy of 0.025. The average of the remaining samples is then subtracted from all samples. Finally the waveform is smoothed using a Savitzky-Golayto[29] filter, removing high frequency noise while preserving the signal area; Figure 3.1 shows the corrected waveform in black.

Pulses are located by looking for contiguous areas of waveform above zero provided the area is at least 15 % of the total area above zero. Three different times measured in ATWD samples are assigned to each pulse: the time when the waveform goes above zero (t_0), the time when the waveform goes below zero (t_1), and the time when the pulse amplitude is maximum (t_{max}). Figure 3.1 shows an example pulse and assigned times.

The time in nanoseconds is given by,

$$t_{ns} = t_{sample} p_{sample} - n_{launch} 25\text{ns}, \tag{3.1}$$

where t_{sample} is the time in ATWD samples, p_{sample} is the nanoseconds per sample, and n_{launch} is the launch offset. p_{sample} is calculated for each ATWD at the start the run using 50 waveforms collected from the sinusoidal signal with a period of 25 ns input to each ATWD.

The number of PE's in a pulse is estimated by dividing the integral of the pulse area by the average integral of the pulse area for each ATWD with the ^{60}Co source deployed at the detector center. The total number of PE's in an event, NPE_{ID}, is equal to the sum of pulse PE's greater than 0.3.

3.4 Position reconstruction

The event vertex is calculated using the collection of pulse t_{max}'s. Figure 3.2 shows the t_{max} distribution subtracting the travel time from the estimated vertex to the PMT for a ^{60}Co event located at the center of the detector. The vertex algorithm is an iterative push-pull method that only uses pulses arriving between 10 ns before and 5 ns after the mean of the peak time. A push or pull in the direction from the currently estimated vertex to the PMT is calculated for all pulses in the time window. The magnitude of each push or pull is determined from the magnitude of the difference between the expected arrival time for a given vertex and the actual arrival time. A new vertex is obtained by summing all push and pull vectors and adding this to the previous vertex. This process is repeated until the new vertex is within 5 mm of the previous vertex. Appendix F describes the details of this algorithm, known as Peak

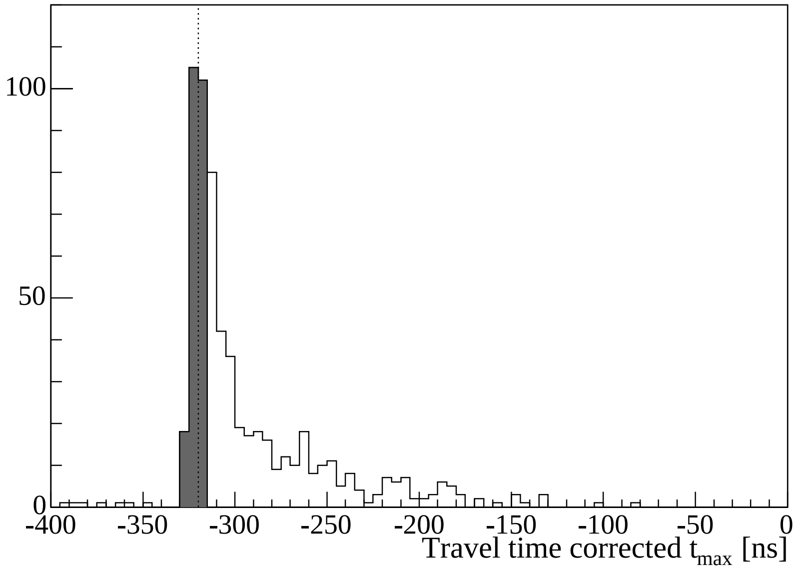

Figure 3.2: t_{max} distribution for a single ^{60}Co event subtracting the travel time from the vertex to the PMT. The shaped region represents the pulses used by PTF and the dashed vertical line represents the mean arrival time of these pulses.

Time Fitter (PTF).

The expected pulse arrival times are obtained assuming photons travel in a straight line from the vertex to the PMT with slightly different effective speeds in the scintillator and buffer oil. The boundary between the scintillator and buffer oil is defined by a simple estimation of the balloon geometry. The effective speeds in the scintillator and the buffer oil are $195\,\mathrm{mm\,ns^{-1}}$ and $205\,\mathrm{mm\,ns^{-1}}$, respectively, obtained by minimizing the reconstructed gamma position biases at all ^{60}Co, ^{68}Ge, and ^{241}Am^{9}Be source positions down the z-axis.

An event has a good vertex if the RMS of t_{max} subtracting the travel time from the vertex for the pulses used is between 2.0 ns and 3.5 ns. Figure 3.3 shows the reconstruction bias and RMS in the z direction for sources deployed down the z-axis. Within the volume analyzed in Chapter 6, the maximum bias is ∼50 mm, and the RMS is consistent to better than ∼5 % for all sources.

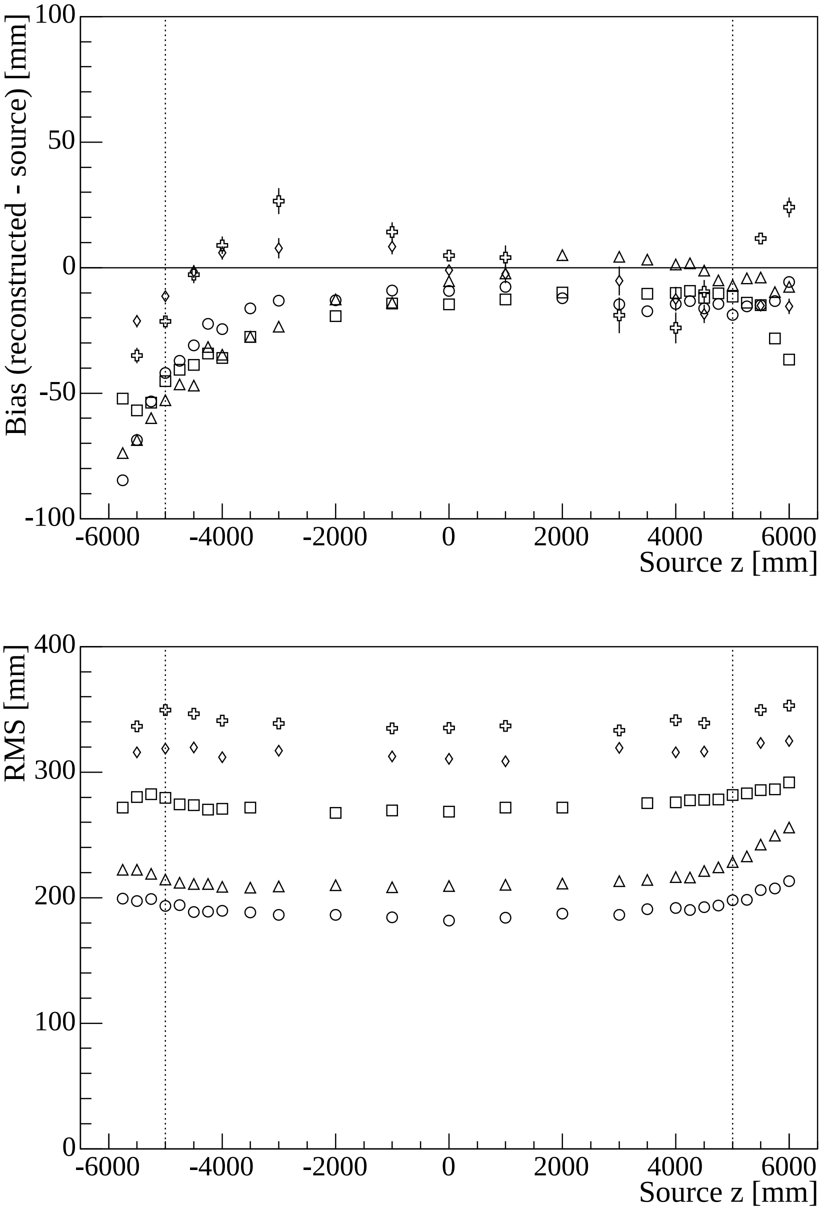

Figure 3.3: Vertex reconstruction bias and RMS in the z direction as a function of source deployment position on the z-axis. ^{60}Co (circles), ^{65}Zn (squares), ^{68}Ge (triangles), ^{241}Am^{9}Be 2.223 MeV γ (diamonds), ^{241}Am^{9}Be 4.43 MeV γ (pluses). The vertical dotted lines represents the maximum and minimum positions for the analysis presented in Chapter 6.

3.5 Energy reconstruction

The energy of a particle is reconstructed from the number PE's, correcting for the event position, and particle type. Only a small fraction of "real" energy is converted into optical photons by the liquid scintillator, and a fraction of these optical photons are detected by the PMT's and recorded by the FEE's. Here the "real" energy refers to the kinetic energy of α's (E_α), the total energy of γ's (E_γ), and the kinetic energy of e^+'s plus the 1.022 MeV energy of the $e^+e^- \rightarrow 2\gamma$ annihilation γ's (E_{e^+}). The "visible" energy (E_{vis}) is calculated from the total number of PE's recorded by the FEE's after correcting for position.

The algorithm to determine E_{vis} maximizes the likelihood for observing the given PMT hit pattern, where the expected number of photons observed at a PMT depends on the solid angle of the PMT, the attenuation length, the number of PE's per MeV, and the mean dark rate. The attenuation length is 25 m, and the number of PE's per MeV per PMT is ~0.22, both are calculated from ^{60}Co deployed at different positions on the z-axis. The mean dark rate is ~0.01 PE's per PMT, deduced from the number of PE's at a random time. Figure 3.4 shows E_{vis} versus distance from the detector center for events following within 0.15 ms to 1.0 ms of a muon. Here the peak at ~ 2 MeV corresponds to γ's from spallation neutrons being captured by ^{1}H. Figure 3.4 shows that the energy is consistent to 1 % throughout the analyzed volume presented in Chapter 6. Figure 3.5 shows the E_{vis} resolution (σ_{vis}) as a function of E_{vis}, which is well fitted by $6.4\,\%/\sqrt{E_{vis}\,\text{MeV}}$. This resolution as added to all calculated energy spectra used in this analysis.

Light quenching and Cerenkov photon production both affect the linear relationship between the "real" energy and E_{vis}. Quenching occurs when the production of scintillation photons saturates for highly ionizing particles and is empirically described by Birks' law[30],

$$\frac{dE_{vis}}{dx} = \frac{\frac{dE}{dx}}{1 + k_b \frac{dE}{dx}}, \tag{3.2}$$

where $\frac{dE_{vis}}{dx}$ is the amount of "visible" energy deposited in the step from x to $x + dx$,

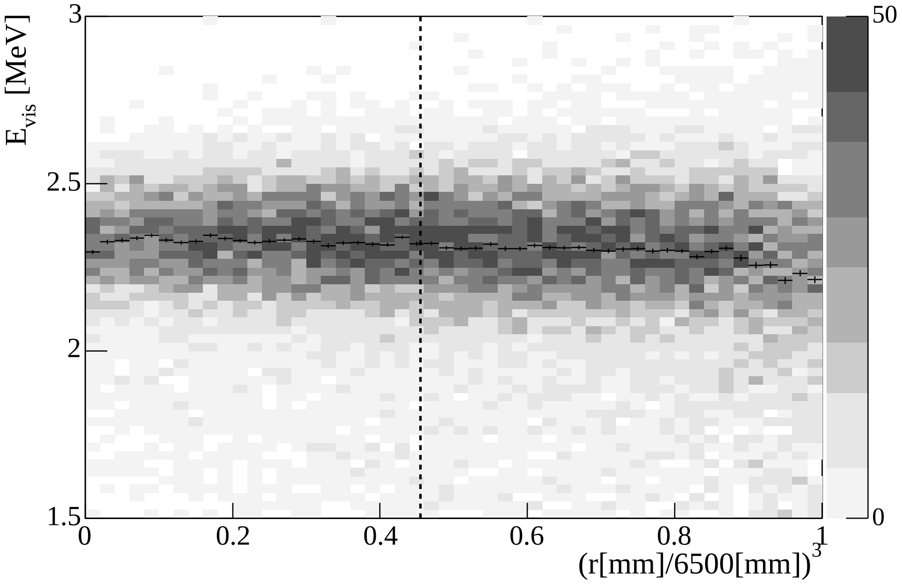

Figure 3.4: E_{vis} versus event radius with respect to detector center for events between 0.15 ms and 1.0 ms after a scintillator muon, see Section 4.1.2, with $\log_{10} Q_{muon} < 7.2$ and good reconstructed track, see Section 3.6. The background between 1.0 ms and 1.5ms is subtracted. The events to the left of the vertical line define the analysis volume used in Chapter 6. The points represent a Gaussian fit at each radius, the variation in the mean of this fit is $\sim 1\,\%$ within the analyzed volume.

$\frac{dE}{dx}$ is the stopping power, and k_b is Birks' constant, which is assumed to be energy and particle independent. For large stopping power $\frac{dE_{vis}}{dx}$ saturates at $1/k_b$. $k_b = 0.990 \pm 0.023 \times 10^{-2}\,\mathrm{g\,cm^{-2}\,MeV^{-1}}$ determined from ^{214}Po and ^{212}Po α's since they have high stopping powers. Optical Cerenkov photons are produced whenever a particle moves faster than the speed of light in that medium. Electrons and positrons with kinetic energy above approximately 0.2 MeV produce Cerenkov photons in the KamLAND scintillator.

The fractional "visible" energy loss due to quenching, $\delta_q(E)$, and Cherenkov photons, $\delta_C(E)$, are particle dependent and are obtained from different Monte Carlo calculations. Taking into account these two effects the relationship between the "real"

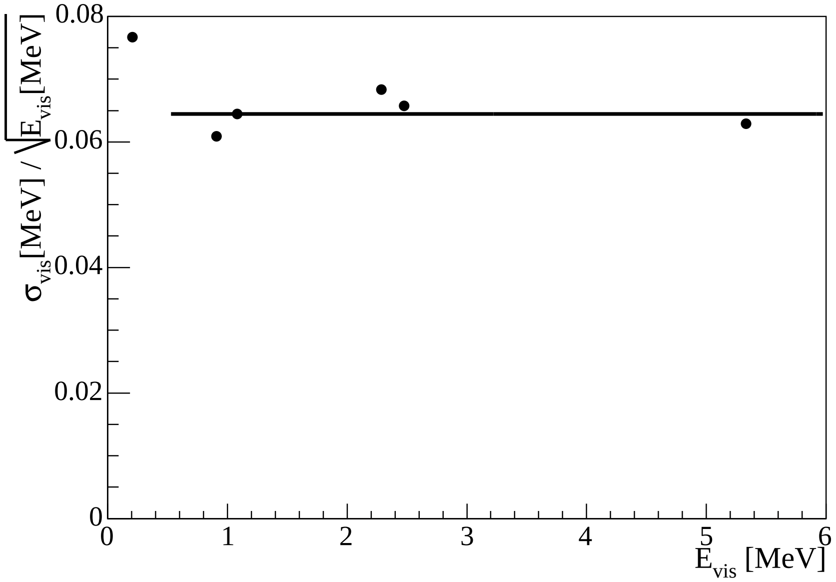

Figure 3.5: E_{vis} RMS (σ_{vis}) as a function of E_{vis}. The horizontal line represents the best fit of $6.4\,\%/\sqrt{E_{vis}\,MeV}$.

energy (E) and E_{vis},

$$\frac{E_{vis}}{E} = 1 - \delta_q(E) + k_o\delta_o(E) + k_C\delta_C(E), \tag{3.3}$$

where $\delta_o(E)$ is the total energy of the particles below the Monte Carlo energy threshold in calculating $\delta_q(E)$, and k_o allows some of this energy to be recovered with an effective quenching factor. Based on a fit to calibration data $k_o = 0.32 \pm 0.14$ and $k_C = 0.29 \pm 0.11$, these are energy and particle independent. Figure 3.6 shows the conversion between E_{vis} and E_γ based in Equation 3.3, including the data from source deployments.

3.6 Muon track reconstruction

Muons pass through the detector producing scintillation photons along the entire path in scintillator and Cherenkov photons in the buffer oil and scintillator. The

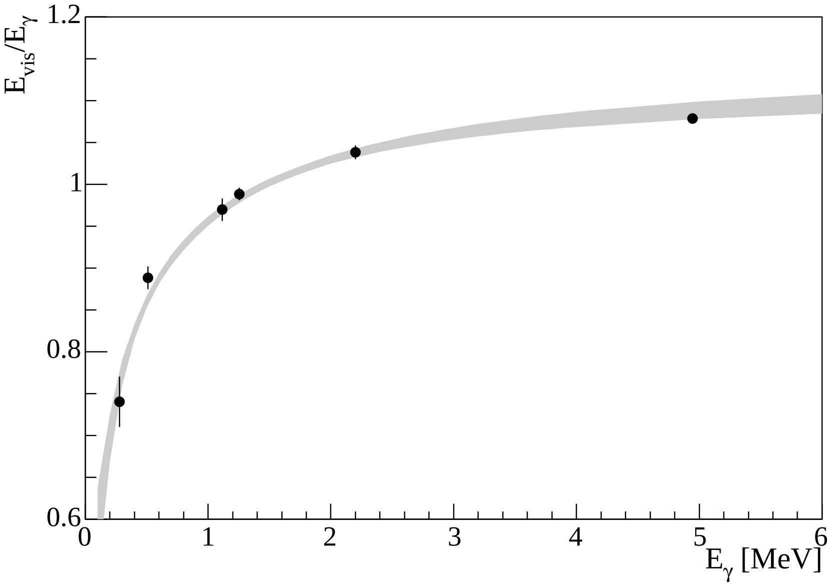

Figure 3.6: E_{vis} to E_γ correction.

number of scintillation photons is approximately ten times more than the number of Cherenkov photons.

A muon track is fitted to all events with $\mathrm{NMax_{ID}} \geq 800$. The left panel of Figure 3.7 shows the distribution of muon total pulse area in arbitrary units (Q_{muon}) for events with $\mathrm{NMax_{ID}} \geq 800$. The peak at $\log_{10} Q_{muon} \approx 7$ is associated with muon tracks passing through the scintillator and buffer oil. The peak at $\log_{10} Q_{muon} \approx 5.5$ is associated with muon tracks passing through the buffer oil only. The lowest peak is associated with radioactivity backgrounds instead of muons, so if $\log_{10} Q_{muon} < 4.5$ no muon track is fitted.

The muon fitter uses the arrival time of the first photons to hit a PMT. Cherenkov photons are produced at an angle, θ_C, relative to the muon track, given by[31]

$$\cos(\theta_C) = \frac{1}{n}, \tag{3.4}$$

where $n = 1.45$ is the refractive index for the optical photons. Scintillation photons

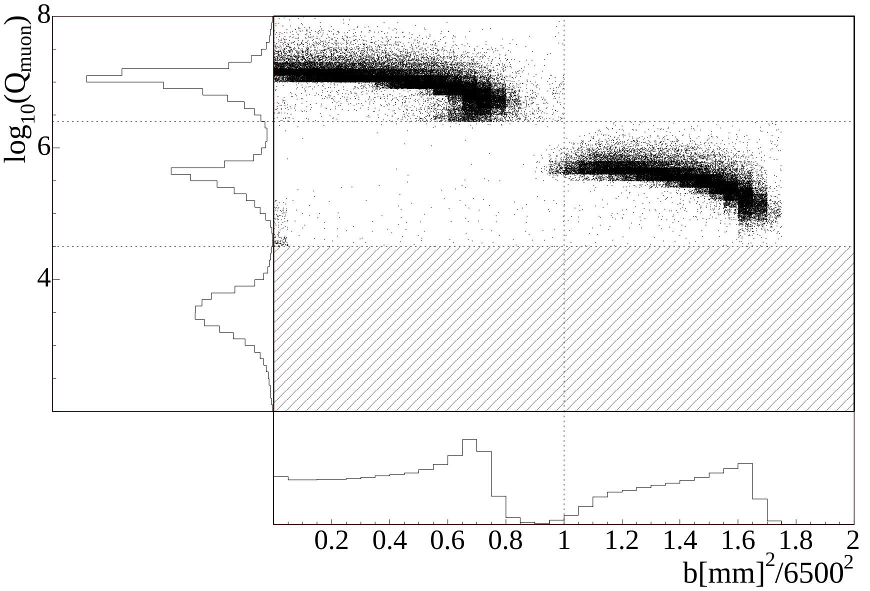

Figure 3.7: Muon total pulse area (Q_{muon}) and closest approach to the detector center (b). The left histogram is for events with $\mathrm{NMax}_{\mathrm{ID}} \geq 800$, the scatter plot and lower histogram also require a good muon track. The vertical line represents the boundary between the scintillator and buffer oil. No muon track is fitted to events below the horizontal line at $\log_{10} Q_{muon} = 4.5$. Events below the horizontal line at $\log_{10} Q_{muon} = 6.4$ are fitted as a oil only muon, otherwise it is fitted as a scintillator muon.

travel isotropically from the muon track. However, due to simple geometric calculations, out of all the scintillation photons, the earliest to hit a particular PMT come from the muon track at the same angle as the Cherenkov photons. Using the first photons to arrive at a PMT allows us to use the same model for Cherenkov and scintillation photons. If $\log_{10} Q_{muon} > 6.4$, the contribution from the buffer oil cherenkov light is ignored, otherwise it is assumed the muon track only passes through the buffer oil. An initial muon track entrance and exit points is estimated from the tubes with the earliest and latest light, respectively. The best fit muon track is obtained by minimizing the deviation between the observed and expected first photon arrival times. Figure 3.7 shows the distribution of the muon tracks closest approach to the detector center, b. At KamLAND we expect the muons to have equal probability of

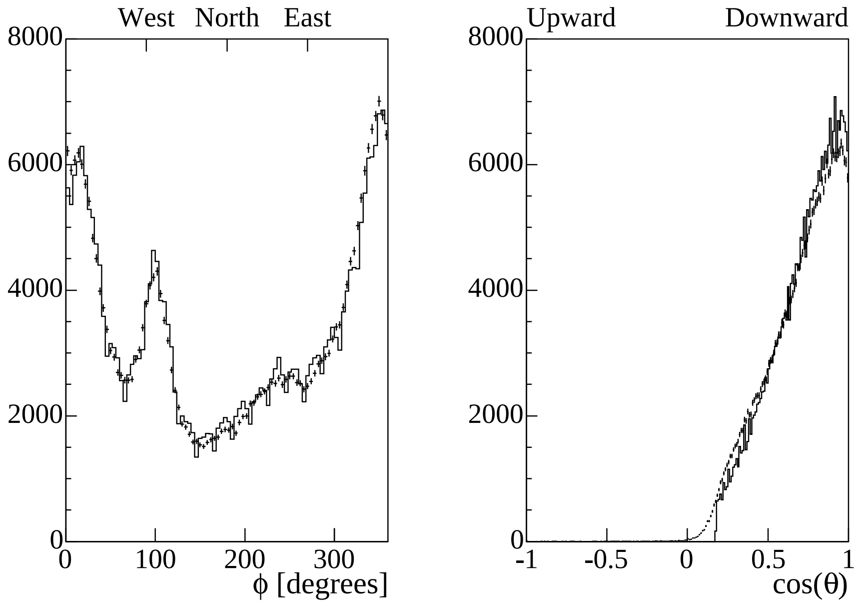

Figure 3.8: Angular distribution of reconstructed muon tracks (points) and simulation (line).

passing through any area; therefore the distribution of b^2 should be flat. It is clear from Figure 3.7 that muons passing through the scintillator close to the balloon are reconstructed slightly toward the center of the detector.

Figure 3.8 shows the angular distribution of the muon tracks, which is well fitted by a simulation taking into account the shape of the mountain above KamLAND. The simulation distributions are normalized to the data. An isotropic muon distribution would result in flat ϕ and $\cos(\theta)$ distributions since these are normalized per unit angular area. The ϕ distribution reflects the different overburden of the mountain in different directions. The $\cos(\theta)$ distribution reflects the amount of matter, including atmosphere, that the muons must go through.

Chapter 4

Candidate selection

The analysis presented here is based on data runs collected between March, 2002 and December, 2003 (runs 207 to 3173). Rudimentary run selection is applied, eliminating runs with anomalous data rates and with data collection failures. The $\bar{\nu}_{\mathrm{e}}$ candidates are selected based on energy, position, and timing cuts chosen to maximize the efficiency for observing neutron inverse β decay, described in Section 1.5, while minimizing backgrounds, described in Chapter 5.

4.1 Cuts

To select prompt and delayed events associated with neutron inverse β decay, we first select good events that are not associated with muons, and then apply space and time coincidences.

4.1.1 Good event cuts

The following good event cuts eliminate periods with excessive noise and ensure that the event selected has a known efficiency, vertex, and energy:

A1, Events within 1.5 ms of the previous event are recorded into multiplets. Events are added to the same multiplet until no event is within 1.5 ms of the last event in the multiplet. Multiplets with greater than four events are removed to eliminate noisy periods. The fraction of livetime from such periods is negligible, $\lesssim 2 \times 10^{-3}\,\%$, and these periods are not correlated with $\bar{\nu}_{\mathrm{e}}$ candidates.

A2, The efficiency for events with $120 \leq \mathrm{NMax}_{\mathrm{ID}} < 200$ is hard to estimate since they require an ID prompt trigger within the previous 1 ms[1]. The neutron inverse β decay delayed event energy, ~2 MeV, is well above the ID prompt trigger threshold. Therefore the reduced ID delayed threshold is not necessary and only events with $\mathrm{NMax}_{\mathrm{ID}} \geq 200$ are considered[2]. Section 4.2.1 discusses the efficiency of this cut.

A3, Only events with a good vertex, see Section 3.4, and energy, see Section 3.5, are considered. Section 4.2.2 discusses the efficiency of this cut.

4.1.2 Muon cuts

The muon cuts eliminate muons, spallation neutrons, and short lived radioactive backgrounds generated by muons. Muons are classified into OD muons ($\mathrm{NMax}_{\mathrm{OD}} \geq 10$), oil muons ($\log_{10} \mathrm{NPE}_{\mathrm{ID}} > 4$), and scintillator muons ($\log_{10} \mathrm{NPE}_{\mathrm{ID}} > 4.8$) OR ($\mathrm{NMax}_{\mathrm{ID}} \geq 1250$ AND $\mathrm{NPE}_{\mathrm{ID}} = 0$)[3]. Events that meet the following muon cuts are removed:

B1, All events, including muons, within 150 μs of a scintillator muon.

B2, Any prompt or delayed event following within 2 ms of any of the muons classified above.

B3, Any prompt or delayed event following within 2 s of any scintillator muon with $\log_{10} Q_{muon} > 7.2$ or with a bad track reconstruction.

---

[1] During normal operation the ID prompt and ID delayed triggers, described in Appendix C.2.1, are enabled with thresholds of 200(~0.8 MeV) and 120(~0.5 MeV), respectively. The ID delayed trigger must occur within 1 ms of the ID prompt trigger.

[2] It is not possible to select only ID prompt triggers since an event could cross the ID delayed trigger threshold before eventually crossing the ID prompt trigger threshold, resulting in only an ID delayed trigger being issued.

[3] This cut is necessary because OD to ID triggers, described in Appendix C.2.1, were not sent to the FEE's before run 1313 in September, 2002, which occasionally resulted in no ID waveforms being recorded.

B4, Any prompt event following within 2 s and 3 m of any scintillator muon with a good track reconstruction.

B5, Any prompt or delayed event following within 2 s of a gap, identified by two consecutive triggers being more than 0.1 s apart.

Section 4.2.3 discusses the efficiency of these muon cuts.

4.1.3 Candidate cuts

Neutrino candidates are selected according to the following cuts:

C1, $|\mathbf{r}_p| < 5000\,\mathrm{mm}$, where $|\mathbf{r}_p|$ is the prompt event radius.

C2, $|\mathbf{r}_d| < 5000\,\mathrm{mm}$, where $|\mathbf{r}_d|$ is the delayed event radius.

C3, $\rho_d > 1200\,\mathrm{mm}$, where ρ_d is the delayed event distance from the z-axis.

C4, $|\mathbf{r}_d - \mathbf{r}_p| < 1000\,\mathrm{mm}$, where $|\mathbf{r}_d - \mathbf{r}_p|$ is the distance between the prompt and delayed events.

C5, $0.5\,\mu\mathrm{s} < t_d - t_p < 500\,\mu\mathrm{s}$, where $t_d - t_p$ is the time between the prompt and delayed events.

C6, $0.9\,\mathrm{MeV} < E_{e^+,p} < 2.7\,\mathrm{MeV}$, where $E_{e^+,p}$ is the E_{e^+} of the prompt event.

C7, $1.8\,\mathrm{MeV} < E_{\gamma,d} < 2.6\,\mathrm{MeV}$, where $E_{\gamma,d}$ is the E_γ of the delayed event.

Sections 4.2.4, 4.2.5, 4.2.6, and 4.2.7 discuss the efficiencies of cuts C1 to C4, C5, C6, and C7, respectively.

4.2 Efficiencies

Table 4.1 summarizes the efficiency for detecting $\bar{\nu}_\mathrm{e}$'s from terrestrial ^{238}U and ^{232}Th. It also includes the efficiency for detection of background events from $\bar{\nu}_\mathrm{e}$'s produced in the nuclear reactors surrounding KamLAND, discussed in Section 5.1, and the

Cut	Efficiency			
	Signal		Background	
	^{238}U $\bar{\nu}_{\mathrm{e}}$	^{232}Th $\bar{\nu}_{\mathrm{e}}$	Reactor $\bar{\nu}_{\mathrm{e}}$	$^{13}\mathrm{C}(\alpha,\mathrm{n})^{16}\mathrm{O}$
$\mathrm{NMax}_{\mathrm{ID}}$	0.99985(9)	0.9996(2)	0.99997(2)	0.9948(26)
Reconstruction	1.000(5)	1.000(5)	1.000(5)	1.000(5)
Muon	0.8531(1)	0.8531(1)	0.8531(1)	0.8531(1)
Spatial	0.845(24)	0.845(24)	0.845(24)	0.809(25)
Timing	0.9094(15)	0.9094(15)	0.9094(15)	0.9094(15)
Prompt energy	0.9995(4)	0.9996(4)		
Delayed energy	0.9946(14)	0.9946(14)	0.9946(14)	0.9946(14)
Total	0.652(19)	0.652(19)	0.652(19)	0.621(20)

Table 4.1: Efficiencies of the different cuts for detecting terrestrial ^{238}U and ^{232}Th $\bar{\nu}_{\mathrm{e}}$'s, reactor $\bar{\nu}_{\mathrm{e}}$'s, and $^{13}\mathrm{C}(\alpha,\mathrm{n})^{16}\mathrm{O}$ background events.

detection of background events from the $^{13}\mathrm{C}(\alpha,\mathrm{n})\mathrm{O}^{16}$ reaction which can mimic neutron inverse beta decay, discussed in Section 5.2.1. The details of each calculation are given below.

4.2.1 $\mathrm{NMax}_{\mathrm{ID}}$ cut efficiency

As shown in Figure 4.1(upper plot) $\mathrm{NMax}_{\mathrm{ID}}$ is correlated with E_{e^+}. Therefore the $\mathrm{NMax}_{\mathrm{ID}} \geq 200$ cut could result in the loss of low energy candidates. Dividing the number of events with $\mathrm{NMax}_{\mathrm{ID}} \geq 200$ by the total number of events Figure 4.1(lower plot) shows the efficiency as a function of E_{e^+}, fitted to an error function with mean 0.856 MeV and sigma 0.054 MeV. The events used to obtain this efficiency are uniformly distributed throughout the fiducial volume, so any dependence on event position is averaged. The total $\mathrm{NMax}_{\mathrm{ID}}$ cut efficiency equals the integral between the prompt energy cut upper and lower limit of the efficiency as a function of E_{e^+} weighted by the expected E_{e^+} distribution for the signal or background.

Throughout the data set the $\mathrm{NMax}_{\mathrm{ID}}$ due to the dark rate varies by ∼3, which is equivalent to a shift in the effective $\mathrm{NMax}_{\mathrm{ID}}$ threshold. This results in a ∼1.5 % shift in the mean of the fit which is added in quadrature with the a 0.6 % error in the E_{vis} to E_{e^+} conversion energy to calculate the efficiency error.

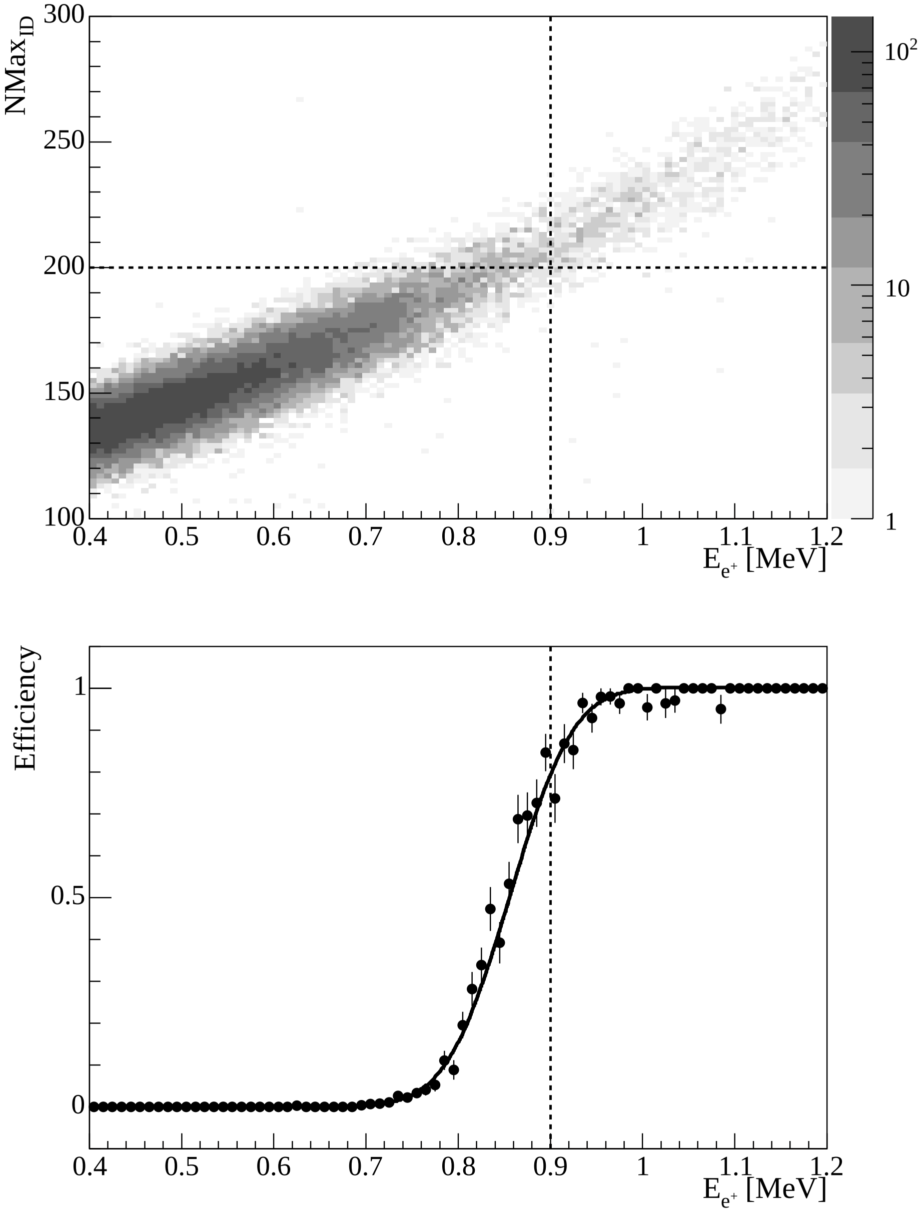

Figure 4.1: The upper plot shows NMax$_{\mathrm{ID}}$ versus E_{e^+} for events within the fiducial volume, collected in a special run with an ID prescale trigger threshold of 35. The horizontal line corresponds to the NMax$_{\mathrm{ID}}$ cut threshold. The lower plot shows the NMax$_{\mathrm{ID}}$ cut efficiency as a function of E_{e^+}. The vertical line in both plots corresponds to the prompt energy cut lower limit.

4.2.2 Reconstruction efficiency

Without a reasonable event position or energy calculation the event is effectively not useable. Therefore we must calculate the efficiency, ε_{recon}, for assigning a reasonable event energy and position. This is not a “typical” cut efficiency since the cut can not be easily change to get a different efficiency. Using sources deployed down the z-axis ε_{recon} is calculated from

$$\varepsilon_{recon} = \frac{A_{recon}}{A_{source}}, \tag{4.1}$$

where A_{recon} is the source activity measured from reconstructed events, and A_{source} is the actual source activity, which was measured to an accuracy of $\sim$3 % before deployment. Since the source activities are so much higher than backgrounds, it is possible to improve the accuracy of A_{recon} by measuring A_{source} during deployment using only trigger data with cuts $300 \leq \mathrm{NMax}_{\mathrm{ID}} < 600$ and $200 \leq \mathrm{NMax}_{\mathrm{ID}} < 300$ for the ^{60}Co and ^{68}Ge sources, respectively. The background with the same cut and no source deployed is then subtracting. A_{recon} is measure with additional cuts: a good energy and vertex exists, the reconstructed vertex is within 1.5 m of the deployed position, and the reconstructed energy is $1\,\mathrm{MeV} < E_{vis} < 3.5\,\mathrm{MeV}$ and $0.5\,\mathrm{MeV} < E_{vis} < 3\,\mathrm{MeV}$ for ^{60}Co and ^{68}Ge sources, respectively.

As shown in Figure 4.2, the average ε_{recon} calculated with the ^{60}Co (^{68}Ge) source deployed at different positions is 1.0002±0.0002 (0.995±0.005). These sources represent the upper and lower energy limits for the analysis presented in Chapter 6 and are both consistent with 1.000, therefore $\varepsilon_{recon} = 1.000 \pm 0.005$.

4.2.3 Muon cut efficiency

The muon cut efficiency equals the fraction of livetime multiplied by fiducial volume remaining after applying the muon cuts, described in Section 4.1.2. This is determined by Monte Carlo integration.

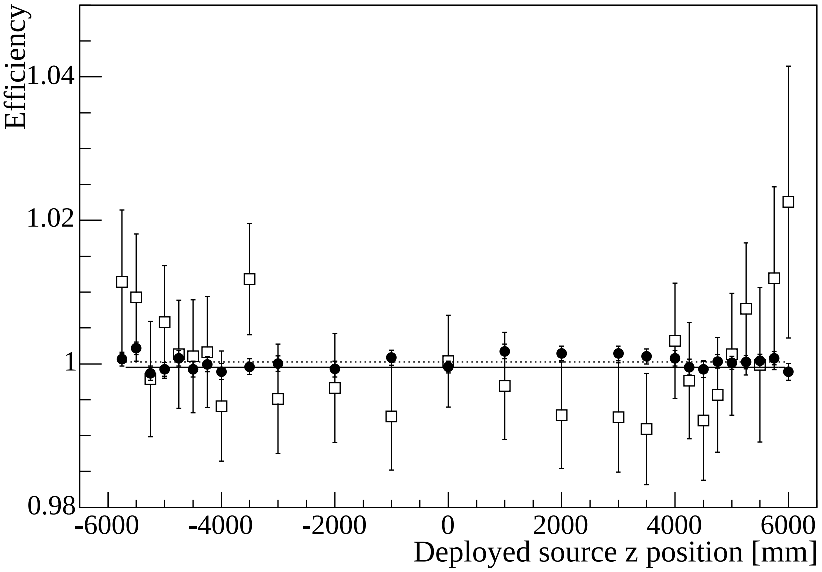

Figure 4.2: Reconstruction efficiency as a function of ^{60}Co (circles) and ^{68}Ge (squares) source deployment position. The horizontal lines represent best fit to ^{60}Co (dotted) and ^{68}Ge (solid) efficiencies.

4.2.4 Spatial cut efficiency

The efficiency of cuts C1 to C4, ε_{space}, is determined from a Monte Carlo simulation of neutron inverse β decays and $^{13}\mathrm{C}(\alpha,\mathrm{n})^{16}\mathrm{O}$ background reactions using Geant4[32]. Events are simulated uniformly in a sphere of 6.5 m, allowing events simulated outside the fiducial volume to pass the cuts. The prompt and delayed vertices equal the mean position of energy deposition determined from the Monte Carlo and include the measured vertex reconstruction resolution. ε_{space} is given by

$$\varepsilon_{space} = \frac{N_{space}}{N_V}, \tag{4.2}$$

where N_{space} is the number of Monte Carlo events passing the cuts and N_V is the number of Monte Carlo events simulated within the fiducial volume. The central values are obtained from averages over prompt event energies and the errors are obtained from the deviations in efficiency over the energy ranges added in quadrature

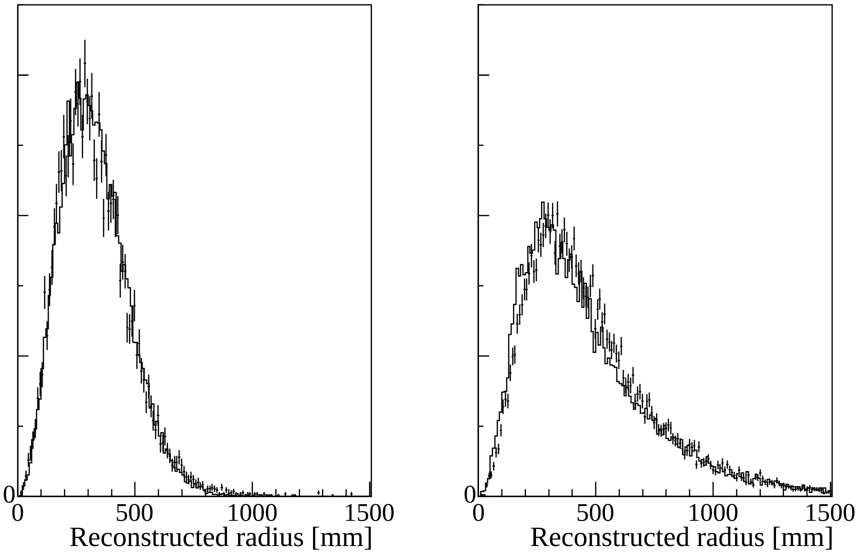

Figure 4.3: The left plot shows the Monte Carlo radial distribution for e^+'s with $\sim$0MeV kinetic energy(line) and the measured radial distribution from ^{68}Ge source events(points). The right plot shows the Monte Carlo radial distribution for neutron capture γ's from neutrons with 5 MeV kinetic energy(line) and the measured radial distribution from ^{241}Am^{9}Be source event neutron capture γ's(points).

with the error obtained from the 5 % variation in the measured vertex resolution shown in Figure 3.3.

Figure 4.3(left) shows the Monte Carlo radial distribution for e^+'s with $\sim$0 MeV kinetic energy and the measured distribution from ^{68}Ge source events. The difference between these distributions results in a 0.3 % difference in the calculated spatial cut efficiency. Similarly Figure 4.3(right) shows the Monte Carlo radial distributions for neutron capture γ's from neutrons with 5 MeV kinetic energy and the measured distributions from ^{241}Am^{9}Be source neutron capture γ events. The difference between these distributions results in a 1.8 % difference in the calculated spatial cut efficiency. Comparing the calculated ^{13}C$(\alpha,\mathrm{n})^{16}$O spatial cut efficiency with that obtained from ^{241}Am^{9}Be source n_0 neutron thermalization and subsequent capture results in a 1.2 % difference. These differences are added in quadrature to the spatial cut efficiency errors.

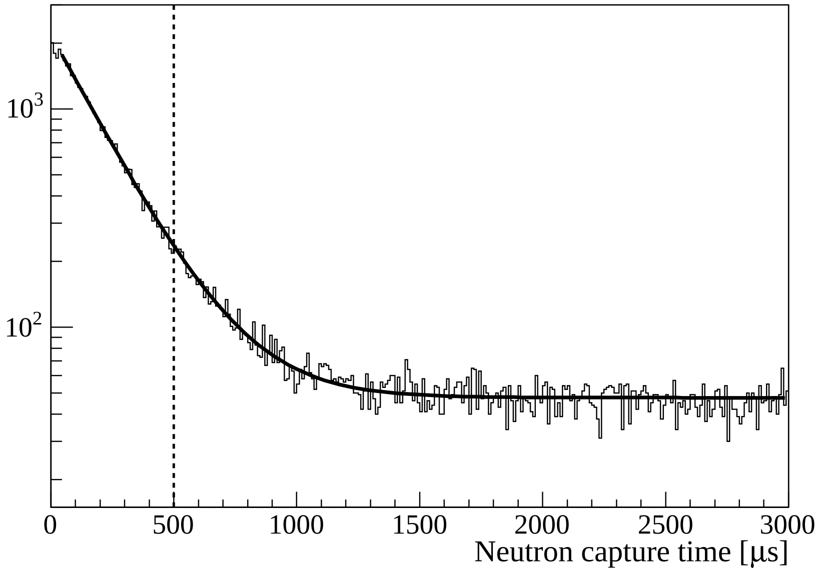

Figure 4.4: Time between all ^{241}Am^{9}Be source n_1 and n_2 neutron events and 2.223 MeV neutron capture γ events, for the source deployed at the center of the detector. The vertical line represents the maximum timing cut and the solid line is a fit to an exponential with a mean time of $205.9 \pm 1.5\,\mu$s and a constant background.

4.2.5 Timing cut efficiency

The timing cut efficiency is given by

$$\varepsilon_t = \int_{0.5\,\mu\mathrm{s}}^{500\,\mu\mathrm{s}} dt\, e^{-t/\tau}, \tag{4.3}$$

where $\tau = 205.9 \pm 1.5\,\mu$s is the mean time between the prompt and delayed events, calculated from the time between all ^{241}Am^{9}Be source n_1 and n_2 neutron events and 2.223 MeV γ neutron capture events, as shown in Figure 4.4.

4.2.6 Prompt energy cut efficiency

The prompt energy cut efficiency equals the fraction of the prompt energy spectrum between the prompt energy cut. For terrestrial $\bar{\nu}_e$ events the error is calculated assuming a 0.8 % (0.6 %) E_{vis} to E_{e^+} error at the lower (upper) prompt energy cut.

Target	Target Fraction	(n,γ) reaction	
		Total γ energy [MeV]	cross-section [mb]
^{1}H	0.6626(66)	2.22	332.6(7)
^{2}H	0.0000994(67)	6.25	0.519(7)
^{12}C	0.3334(33)	4.95	3.53(7)
^{13}C	0.00371(11)	8.17	1.37(4)
^{14}N	0.0001365(14)	10.83	7.50(75)
^{16}O	0.0000676(7)	4.14	0.190(19)

Table 4.2: Relative abundance of neutron capture targets in KamLAND scintillator, total γ energy released on capture, and capture cross-section.

The resulting errors on the prompt energy cut efficiency are added directly since these energy conversion errors may be correlated. The energy scale also includes a 1 % error due to the radial variation in E_{vis} and a 0.6 % error due to the temporal variation in E_{vis}, the corresponding prompt energy cut efficiency errors are added in quadrature to the error obtained from the energy conversion error. The prompt energy cut efficiency for the reactor $\bar{\nu}_{\mathrm{e}}$ background and $^{13}\mathrm{C}(\alpha,\mathrm{n})^{16}\mathrm{O}$ background are included in the calculation of their rates in Sections 5.1 and 5.2.1, respectively.

4.2.7 Delayed energy cut efficiency

The delayed energy cut efficiency is given by

$$\varepsilon_d = P(^{1}\mathrm{H}) f_d, \tag{4.4}$$

where $P(^{1}\mathrm{H})$ is the probability of a neutron being captured by a proton producing a 2.223 MeV γ, and f_d is the probability of the 2.223 MeV γ passing the delayed energy cut. $P(^{1}\mathrm{H})$ is obtained from

$$P(^{1}\mathrm{H}) = \frac{f(^{1}\mathrm{H})\sigma(^{1}\mathrm{H})}{\sum_i f(i)\sigma(i)} = 0.99462 \pm 0.00013, \tag{4.5}$$

where $f(i)$ is the target fraction for nuclei i in the KamLAND scintillator, and $\sigma(i)$ is the neutron capture cross-section[33]. $f(i)$ and $\sigma(i)$ are given in Table 4.2.

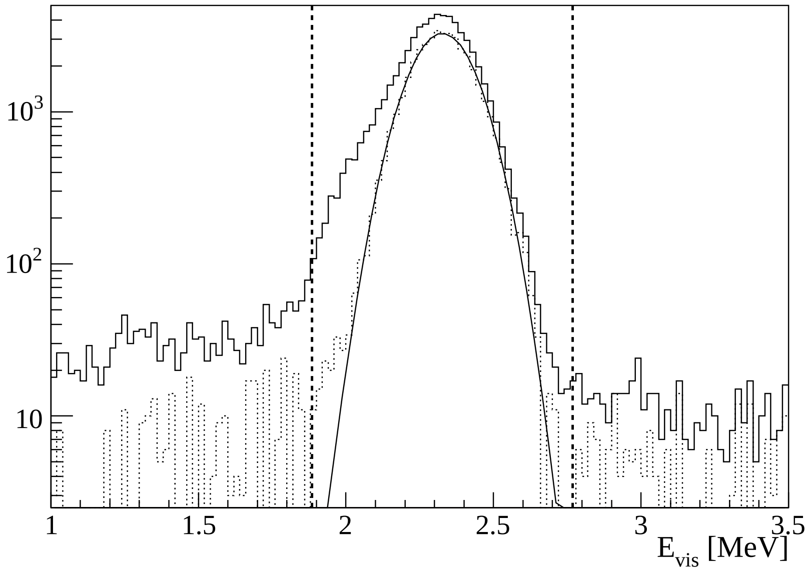

Figure 4.5: E_{vis} for ^{241}Am^{9}Be events within 500 μs of the previous event (solid) with the ^{241}Am^{9}Be source deployed at the center of the detector. E_{vis} for ^{241}Am^{9}Be events within 50 μs and 500 μs subtracting events within 1350 μs and 1500 μs of the previous event (dot). The vertical lines represent the delayed energy cut upper and lower limits converted into the equivalent E_{vis}.

Figure 4.5 shows the E_{vis} distribution for events within 500 μs of the previous event. The peak at $E_{vis} \approx 2.3\,\mathrm{MeV}$ is caused ^{1}H(n,γ) γ's, where the low energy shoulder could be caused by missing waveforms due to FEE dead-time. As described in Section 2.3, if an event occurs within $\sim 30\,\mu$s of the previous event, all the PMT's with a waveform from the previous event have one ATWD busy digitizing the previous event. If the second ATWD from these PMT's is also busy, then the waveform is not recorded, causing a decrease in the calculated E_{vis}. The probability of an ATWD being busy depends on the previous event's E_{vis} and location. To investigate the effect of this Figure 4.6 shows the mean E_{vis} of the ~2.3 MeV peak as a function of time to last event for the ^{241}Am^{9}Be source deployed at the center (upper left plot) and at z=5.5 m (upper right plot). Figure 4.6(lower plot) shows the mean E_{vis} of the ~ 2.3MeV peak for events within 25 μs of the previous event as a function of the previous event E_{vis}. There is clearly a shift in the mean of the ~2.3 MeV peak for

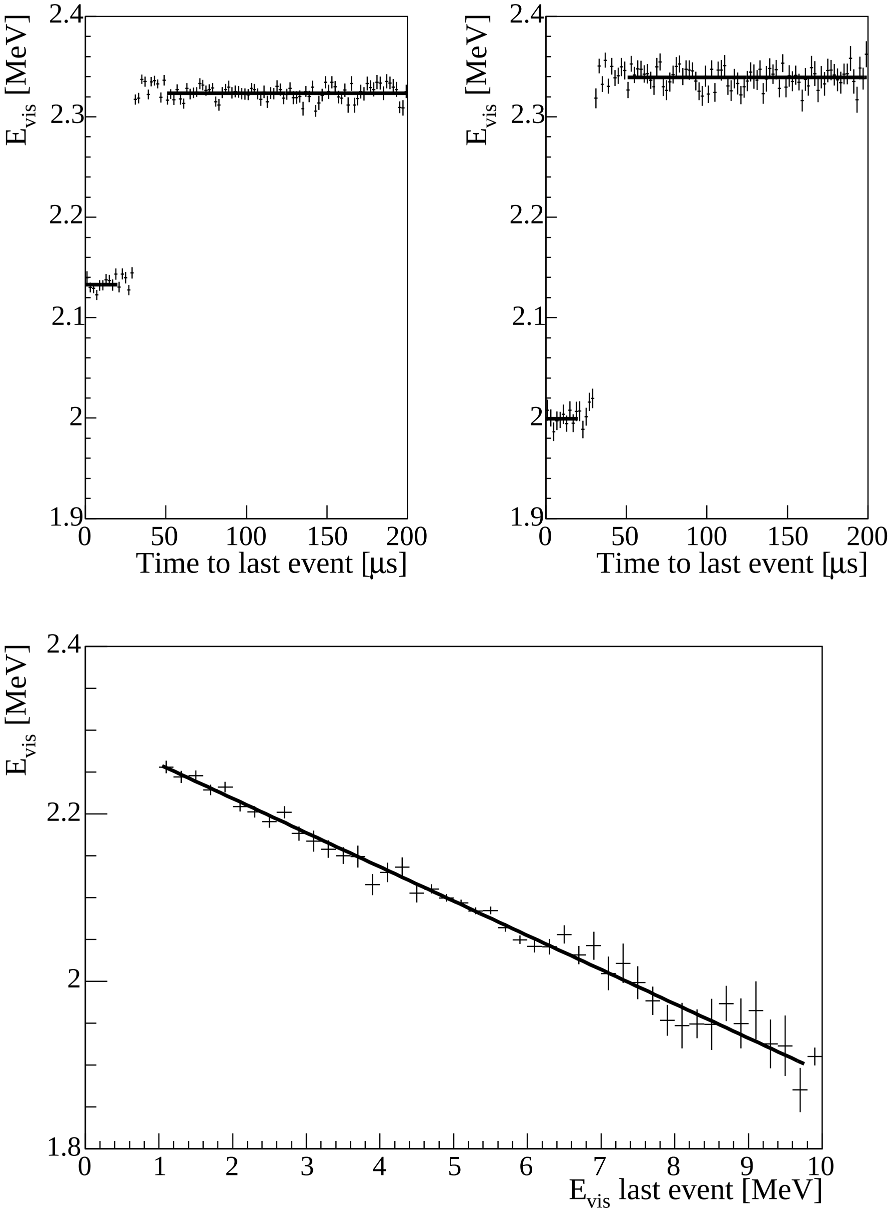

Figure 4.6: The mean E_{vis} for ^{241}Am^{9}Be events as a function of time since the previous event for the source deployed at the center(top left) and at z=5.5 m(top right). The bottom plot shows the mean E_{vis} for events within 25 μs of the previous event as function of the previous event E_{vis} where the line is a linear fit with an offset of 2.3 MeV and a slope of -0.04 MeV/MeV.

events within 30 μs of the previous event, where the size of the shift depends on the source location and linearly on E_{vis} of the previous event. By only select delayed events within 50 μs and 500 μs of the previous event the low energy shoulder of the peak at ∼2.3 MeV is almost absent, as shown by the dotted histogram in Figure 4.5. A Gaussian fit to this peak gives a mean of 2.3266±0.0006 MeV and a sigma of 0.1031±0.0005 MeV.

f_d equals the integral between the delayed energy cut upper and lower limits of the delayed energy distribution. For prompt events with E_{vis} ∼3 MeV at the fiducial boundary, the mean energy of a delayed event within 30 μs would be shifted by ∼ 0.2 MeV, resulting in a 0.8 % reduction in the delayed energy cut efficiency. Only ∼15 % of delayed events occur within 30 μs of the prompt event, resulting in a 0.14 % error in the delayed energy cut efficiency.

4.3 Number of target protons

The number of target protons in the fiducial volume, $N_p = (3.04 \pm 0.20) \times 10^{31}$, is calculated from

$$N_p = \rho_p f V_{scint}, \tag{4.6}$$

where $\rho_p = (6.66 \pm 0.11) \times 10^{22}\,\text{protons}\,\text{cm}^{-3}$ is the scintillator proton density, f is the ratio of fiducial volume to total scintillator volume, and $V_{scint} = 1171 \pm 25\,\text{m}^3$ is the total scintillator volume, calculated from flow rates during filling.

f is calculated from the ratio of ^{12}B β^- decays reconstructed inside the fiducial volume to the total number of ^{12}B β^- decays in the scintillator. ^{12}B is produced by muons passing though the detector, and decays with a half-life of 20.2 ms and an endpoint energy of 13.4 MeV. It is assumed that ^{12}B is generated uniformly since muons pass through KamLAND with a uniform distribution, and ^{12}B production in the scintillator and buffer oil should be similar since they have similar densities and isotopic abundances. Figure 4.7 shows the radial distribution of ^{12}B events, which results in a measured value of $f = 0.388 \pm 0.021$.

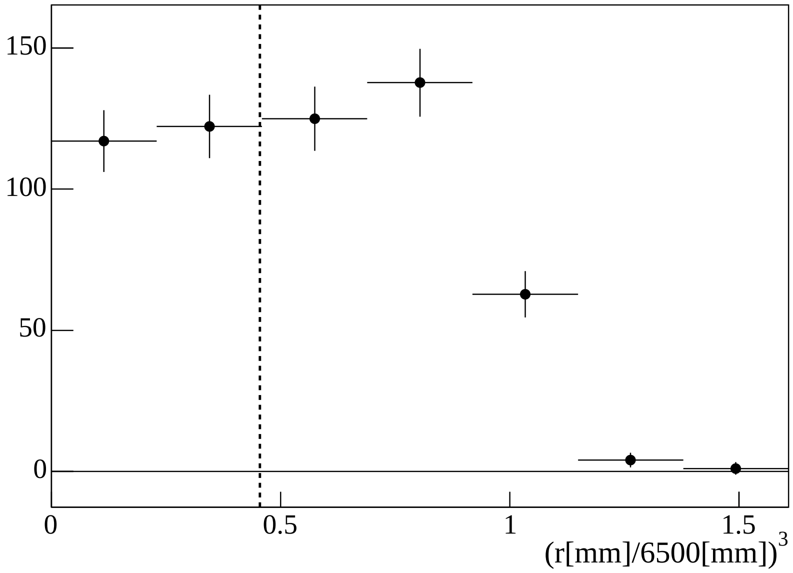

Figure 4.7: ^{12}B radial distribution. The vertical line represents the fiducial volume cut.

^{12}B β^- decays have energies up to 13.4 MeV. However, we are interested in the fiducial volume for events between 0.9 MeV and 2.7 MeV. An energy correction to the fiducial volume is obtained using the distribution of ^{9}Li events generated after muons. These have a prompt event with energy up to 11.2 MeV and a correlated delayed event with energy of 2.22 MeV. For events near the fiducial boundary the difference between the prompt and delayed event radius corresponds to a factor of 1.005 ± 0.013 increase in f at 2.22 MeV.

Although the ^{12}B events are generated uniformly, it is not clear that they are identified uniformly since this relies on muon identification which is not as efficient in the buffer oil. To test the effect of this, only ^{12}B events after scintillator muons are selected, resulting in a 2.1 % increase in f. This represents an upper limit in the error due to muon identification in the oil, so it is added in quadrature to the total error.

4.4 Livetime

The total livetime for the data set equals 484.75 ± 0.24 days, calculated by summing the number of 40 MHz clock-ticks between successive triggers and multiplying it by the clock period. Periods between successive triggers greater than 4×10^6 clock-ticks (0.1 s) are not included since these probably correspond to periods when the trigger module disabled due to a full memory. The error is determined from the fraction of actual livetime with time between events greater than 0.1 s, calculated with a lower limit on the trigger rate of 100 Hz. Other errors are negligible, as described in Appendix G.

Chapter 5

Backgrounds

The number of $\bar{\nu}_{\mathrm{e}}$ candidate background events equals 71.6±6.9, summarized in Table 5.1, with the estimation details given below. Other backgrounds considered and found to be negligible include spontaneous fission, neutron emitters and correlated decays in the ^{238}U and ^{232}Th decay chains, (γ,n) reactions, and solar ν_e induced break up of ^{2}H.

5.1 Nuclear reactor background

KamLAND was designed to observe $\bar{\nu}_{\mathrm{e}}$'s from nuclear power plants, and an analysis of the $\bar{\nu}_{\mathrm{e}}$ energy spectrum above $E_{e^+} = 2.6\,\mathrm{MeV}$, where the terrestrial $\bar{\nu}_{\mathrm{e}}$ signal is

Background	
Nuclear reactor $\bar{\nu}_{\mathrm{e}}$	47.0±5.4
Long-lived nuclear reactor $\bar{\nu}_{\mathrm{e}}$	0.25±0.16
(α,n)	21.9±4.2
Fast neutron	1.01±0.50
Random coincidence	1.41±0.13
Cosmogenic	0.02±0.01
Total	71.6±6.9

Table 5.1: Summary of the backgrounds for the given cuts, livetime and number of target protons.

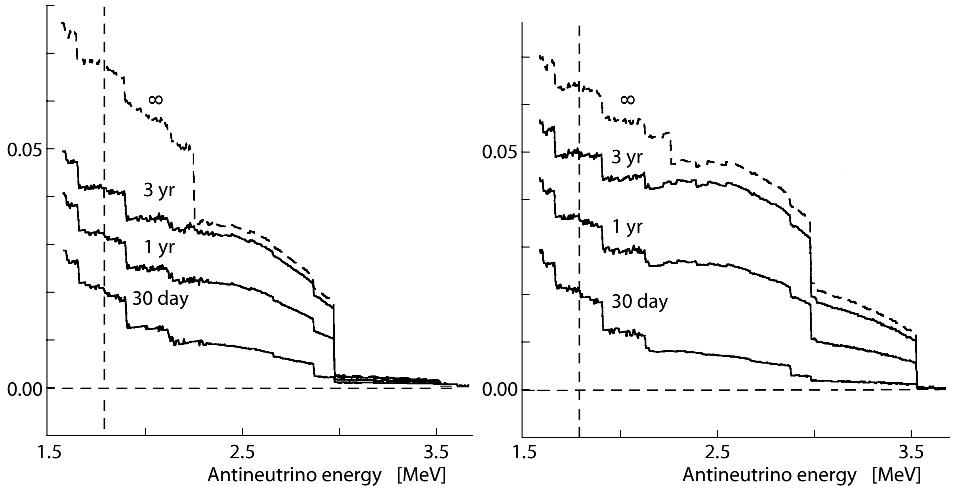

Figure 5.1: Calculated fractional increase in the spectrum obtained after varying lengths of irradiation to that obtained after one day for ^{235}U (left) and ^{239}Pu (right). The vertical lines represent the detection threshold at KamLAND. Modified from Kopekin[36].

negligible, gives the best measurement to date of Δm^2_{12}[21].

Nuclear reactors produce energy primarily from the fission of ^{235}U, ^{239}Pu, ^{241}Pu, and ^{238}U. β^- decay of fission products produces $\bar{\nu}_\mathrm{e}$'s. The $\bar{\nu}_\mathrm{e}$ energy spectrum for ^{235}U, ^{239}Pu, and ^{241}Pu fission is calculated[34, 35] from the β^- energy spectrum measured after exposing each isotope to a thermal neutron flux for approximately 12 hours. Fission fragments with half-lives greater than a few hours would not have reached equilibrium in this time, resulting in the calculated[36] fractional increase in the $\bar{\nu}_\mathrm{e}$ spectrum for longer irradiation times shown in Figure 5.1. The β^- energy spectrum for ^{238}U exposed to a thermal neutron flux has not been measured. Therefore the $\bar{\nu}_\mathrm{e}$ spectrum for ^{238}U fission is calculated[37] from the fission fragment abundances, the β^- decay endpoints, and branching ratios. The error in the total reactor spectrum is estimated to be 2.5 % based on the total reactor $\bar{\nu}_\mathrm{e}$ spectrum measured with detectors placed 15 m and 40 m from a reactor[38].

We have developed a model for the fission rate of each isotope based on the instantaneous thermal power, integrated thermal power from the last reactor refuelling, initial ^{235}U concentration in the new fuel, and the fraction of new fuel at the last refuelling. Where 1/3 of a nuclear reactors fuel is typically replaced with fresh fuel every year. Comparing this model to a detailed simulation the error in the fission rate is estimated to be $\lesssim$1.0 %. Input data to this model for each of the 54 commercial reactor cores in Japan is normally provided to us weekly, but is provided hourly when a reactor is refuelled. The most significant error in the input data is due to the thermal power which results in 2 % error in the fission rate. Over the current data set the average relative contribution from the fission of the ^{235}U:^{238}U:^{239}Pu:^{241}Pu isotopes is 0.563:0.079:0.301:0.057. The contribution from South Korean reactors is calculated using the published electrical power for each power plant and the average fission rate for the Japanese reactors, with a 10 % error assigned to reflect the uncertainty in the conversion from electrical to thermal power. The contribution from all other reactors is calculated from the rated power for each reactor and the average fission rate for the Japanese reactors, with a conservative 50 % error assigned.

The number of reactor $\bar{\nu}_{\mathrm{e}}$ backgrounds is given by

$$N_{reactor} = \varepsilon N_p \int_{0.9\mathrm{MeV}}^{2.7\mathrm{MeV}} dE_{e^+} \int dt \, \frac{dN}{dE_{e^+}dt} \left(E_{e^+}, t\right), \tag{5.1}$$

where ε is the reactor $\bar{\nu}_{\mathrm{e}}$ detection efficiency, given in Section 4.2, N_p is the number of target protons, given in Section 4.3, $\frac{dN}{dE_{e^+}dt}\left(E_{e^+}, t\right)$ is the expected reactor energy spectrum as a function of time, the energy integral is over the prompt energy cut limits, and the time integral is over the entire livetime. The error includes the errors in the expected signal, the error in the number of target protons, and the error in the detection efficiency. The error in the expected signal includes a 3.4 % error due to the production rate at nuclear reactors, a 7.9 % error due to the neutrino survival probability caused by neutrino oscillations, and a 2.6 % error due to the E_{vis} to E_{e^+} conversion.

The background due to $\bar{\nu}_{\mathrm{e}}$'s from the long-lived nuclear reactor fission products is obtained from $\frac{dN}{dE_{e^+}dt}\left(E_{e^+}, t\right)$ multiplied by the average of the ^{235}U and ^{239}Pu fractional increases in Figure 5.1. The long-lived isotopes contained in the spent fuel continue to produce $\bar{\nu}_{\mathrm{e}}$'s as they decay. Currently more than half of the spent fuel in Japan is stored next to the reactor with most of the remainder having been sent overseas for reprocessing[1][39]. If the spent fuel is stored next to the reactor, then the total $\bar{\nu}_{\mathrm{e}}$ flux is equal to that obtained with no fuel replacement. The central value for the background assumes that all the spent fuel is stored next to the reactor, and the reactor has been on for an infinite amount of time. The error is obtained from the difference to the minimum, where the minimum is calculated assuming 1/3 of the fuel has just been replaced, 2/3 has been in the reactor for one year, and all the spent fuel was sent overseas for reprocessing.

5.2 Neutron production

The signals from neutrons produced with a few MeV of kinetic energy can mimic those of neutron inverse β decay. The neutrons first thermalize, ionizing ^{1}H in the process, which produces scintillation light. Later the neutrons can be captured by protons, producing identical delayed event signals to those of neutron inverse β decay delayed events.

5.2.1 (α,n) background

The (α,n) reaction could produce neutrons with a few MeV of kinetic energy. Table 5.2 summarizes the threshold α kinetic energy for different (α,n) target nuclei present in the scintillator. Given these thresholds the only significant α particle source in the scintillator comes from ^{210}Po decay which has a kinetic energy of 5.3 MeV. Because of quenching, discussed in Section 3.5, $E_{vis} = 0.3\,\mathrm{MeV}$. The ^{210}Po decay rate within the fiducial volume equals $23.0 \pm 2.3\,\mathrm{Bq}$, measured from the peak at $E_{vis} = 0.3\,\mathrm{MeV}$ with a low threshold run. The ^{210}Po comes from the decay of ^{210}Pb which has a half-life of 22.3 years and is distributed throughout the detector.

Given α particles with kinetic energy less than 5.3 MeV, ^{13}C is the only target with a threshold low enough to produce neutrons from the (α,n) reaction. The total

---

[1] The reprocessed fuel returned to Japan does not contain the long-lived isotopes.

Target	Target Fraction	(α,n) threshold [MeV]
^{1}H	0.6626(66)	118.01
^{2}H	0.0000994(67)	12.52
^{12}C	0.3334(33)	11.34
^{13}C	0.00371(11)	0
^{14}N	0.0001365(14)	6.09
^{16}O	0.0000676(7)	15.18

Table 5.2: (α, n) targets in KamLAND scintillator.

number of neutrons produced per α particle, Y, is given by

$$Y = \rho \int_0^{E_\alpha} \mathrm{d}E \, \frac{\sigma(E)}{\frac{\mathrm{d}E}{\mathrm{d}x}(E)} = (6.0 \pm 0.3) \times 10^{-8}, \tag{5.2}$$

where the target density $\rho = 3.7 \times 10^{20}$ $^{13}\mathrm{C}\,\mathrm{nuclei}\,\mathrm{cm}^{-2}$, $\sigma(E)$ is the reaction cross-section[40] shown in Figure 5.2, $\frac{\mathrm{d}E}{\mathrm{d}x}(E)$ is the α particle stopping power[41], and E_α is the maximum kinetic energy of the α particle. The error is estimated by repeating the total neutron yield calculation with thick natural C targets and comparing to the measured value[42].

The Q value for the $^{13}\mathrm{C}(\alpha, \mathrm{n})^{16}\mathrm{O}$ reaction is 2.216 MeV. The maximum kinetic energy available to the neutron and ^{16}O in the center of mass frame is 6.27 MeV; therefore the ^{16}O could be created in its 6.05 MeV and 6.13 MeV excited-states. Using the ratio to the excited-states obtained from a Hauser-Feshbach statistical model[40], the cross-section for the $^{13}\mathrm{C}(\alpha, \mathrm{n})^{16}\mathrm{O}^*$ reactions are included in Figure 5.2. The 6.05 MeV excited-state decays by pair production, and the 6.13 MeV excited-state decays by γ emission. Both result in a prompt E_{vis} greater than the upper threshold, so they do not mimic terrestrial $\bar{\nu}_\mathrm{e}$'s, reducing the total number of observable neutrons from the $^{13}\mathrm{C}(\alpha, \mathrm{n})^{16}\mathrm{O}$ reaction by 9.2 %. The excited state cross-section error is unknown, although the peak at ~6 MeV in the prompt energy is consistent with the nominal excited state cross-sections, and can exclude a value twice as large. Therefore a 100 % error in the excited-state cross-section is included.

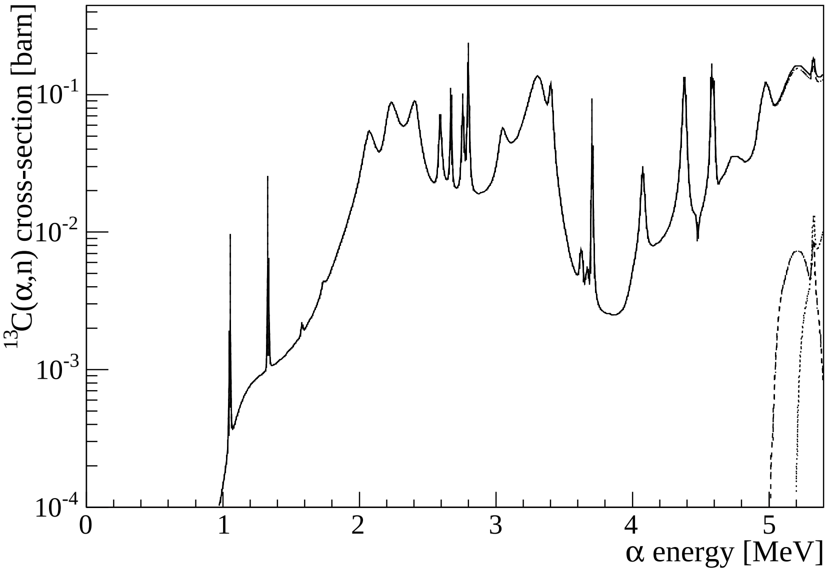

Figure 5.2: Total (solid) $^{13}\mathrm{C}(\alpha,\mathrm{n})^{16}\mathrm{O}$ cross-section and cross-section to ^{16}O ground-state (dot-dash), 6.05 MeV excited-state (dash), and 6.13 MeV excited-state (dot).

The neutron kinetic energy depends on the α particle kinetic energy and the angle at which the neutron is emitted. The maximum and minimum neutron kinetic energies are 7.3 MeV and 2.2 MeV, respectively. The neutron angular distribution as a function of α particle kinetic energy is obtained from the measured Legendre coefficients[43, 44]. The neutron energy distribution, shown in Figure 5.3, is calculated from the $^{13}\mathrm{C}(\alpha,\mathrm{n})^{16}\mathrm{O}$ cross-section, the alpha stopping power, and the neutron angular distribution. There is a large error in the neutron angular distribution, so Figure 5.3 includes a calculation of the neutron energy distribution assuming a uniform neutron angular distribution in the center of mass frame. Figure 5.3 also includes the neutron distribution calculated assuming zero branching ratio to the ^{16}O excited state. These different neutron energy distribution calculations produce deviations up to 50 % at some energies. These deviations are consistent with the deviations from the measured distribution[45] with incident α particle kinetic energies of 5.5 MeV, 5.0 MeV, 4.5 MeV, and 4.0 MeV.

The visible energy for the neutron thermalization is calculated from a Monte

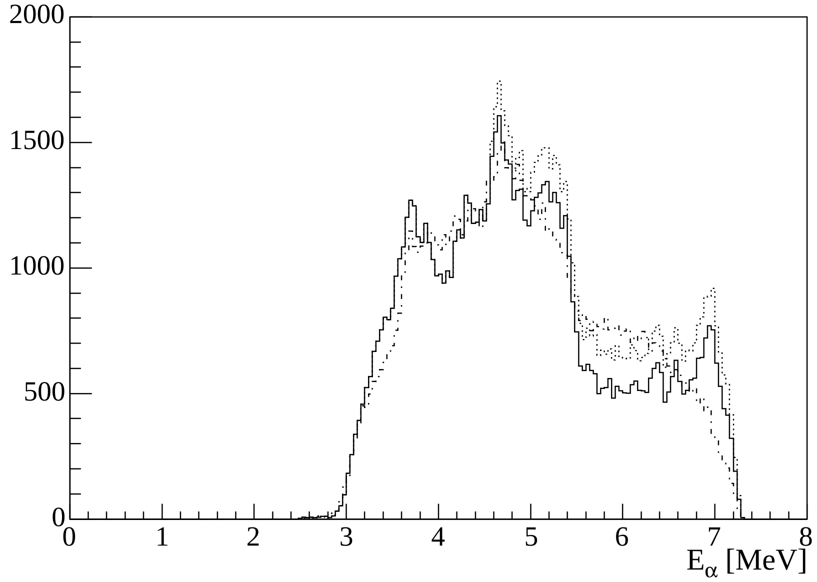

Figure 5.3: ^{13}C$(\alpha, \mathrm{n})^{16}$O neutron energy distribution with fit to angular distribution (solid) and with uniform angular angular distribution in center of mass frame (dot-dash). With fit to angular distribution and assuming no excited state cross-section (dot), this overlaps the solid line at low energies.

Carlo using Geant3[46]. This smooths the different energy distributions shown in Figure 5.3 resulting in a 6 % error in visible energy distribution between the prompt energy upper and lower cuts. The fraction of ^{13}C$(\alpha, \mathrm{n})^{16}$O neutron events passing the prompt energy cut is 0.61 ± 0.09. The error also includes a 5.6 % error added in quadrature due to the 5 % error in calculating E_{vis} based on a comparison of the Monte Carlo and measured visible energy for ^{241}Am^{9}Be source n_0 and n_1 events.

5.2.2 Fast neutron background

Muons passing through KamLAND and the surrounding rock produce fast neutrons that can enter the ID producing a signal that mimics a $\bar{\nu}_{\mathrm{e}}$ candidate. Fast neutrons produced by muons passing through the scintillator, oil, or OD are vetoed by the 2 ms cut following these muons. However, some backgrounds remain due to muon identification inefficiencies. The number of $\bar{\nu}_{\mathrm{e}}$ candidates within 2 ms of any OD only muon is 7. Dividing this by the OD muon identification efficiency, η_{OD}, we obtain the number of candidates generated by fast neutrons from muons passing through only the OD, not the scintillator or oil, N_{OD}. After applying the OD muon cut the number of fast neutron backgrounds equals $N_{OD}(1 - \eta_{OD})$.

Additional fast neutron backgrounds exist from muons that only pass through the rock and hence cannot be vetoed. Assuming the rate of neutron production scales according to the mass of the material the muon passes through, the number of candidates generated by fast neutrons from muons passing through the rock, N_{rock}, can be estimated from N_{OD}, by

$$N_{rock} = \alpha f \frac{A_{cavern}\lambda_{rock}\rho_{rock}}{4V_{OD}\rho_{water}} N_{OD} = 0.007 N_{OD}, \tag{5.3}$$

where $\alpha \simeq 0.7 \pm 0.3$[47] accounts for the extra attenuation of neutrons generated in the rock, and $f = 0.05$[47] is the fraction of muons passing through the volume of rock that do not pass through the OD, oil, or scintillator. $A_{cavern} = 1835\,\mathrm{m}^2$ is the area of the rock surface, $\lambda_{rock} = 0.4\,\mathrm{m}$ is the maximum neutron attenuation length in rock[48], $\rho_{rock} = 2.7\,\mathrm{g\,cm^{-2}}$ is the density of rock, $\rho_{water} = 1.0\,\mathrm{g\,cm^{-2}}$ is the density of water, and $V_{OD} = 2600\,\mathrm{m}^3$ is the volume of water in the OD.

The measured rate of muons passing through the scintillator is 0.204 Hz. Due to the large amount of light produced by scintillator muons, it is assumed that identification of scintillator muons is 100 % efficient. The measured rate of muons passing through the OD has decreased from 0.67 Hz to 0.62 Hz over the data set. Based on detector geometry and the muon angular distribution shown in Figure 3.8, the expected OD muon rate should be 3.57 times the scintillator muon rate; therefore, it is assumed $\eta_{OD} = 0.88 \pm 0.04$.

5.3 Random coincidence background

Two uncorrelated events can pass the cuts described in Section 4.1 as a coincidence pair. After applying the good event and muon cuts the number of random coincidence

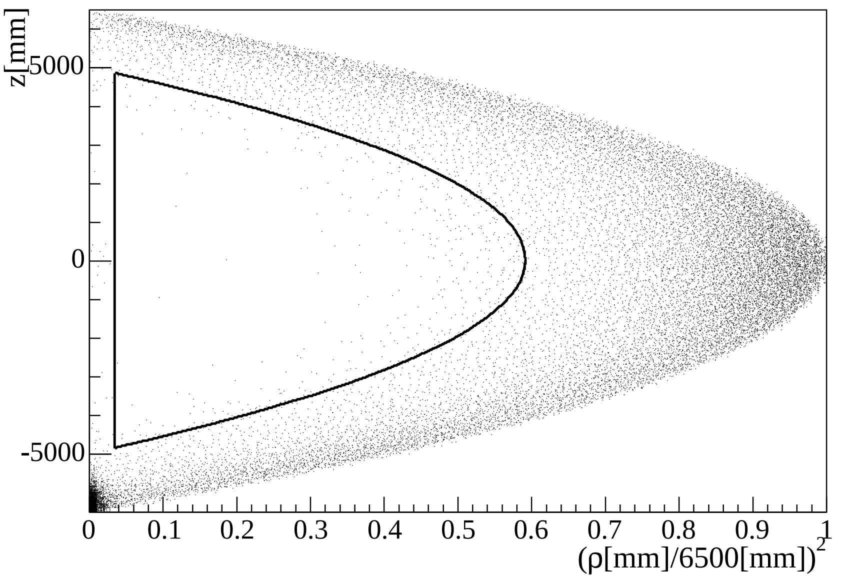

Figure 5.4: Spatial distribution of the prompt randomly paired events that pass all cuts except $|\mathbf{r}_p|$, $|\mathbf{r}_d|$, or ρ_d cuts. The solid line represents the fiducial volume.

background events is given by

$$N_{rand} = N_{\Delta t} P_{coin}, \tag{5.4}$$

where $N_{\Delta t} = 1,921,705$ is the number of uncorrelated events within the timing cut of each other, and $P_{coin} = (7.33 \pm 0.70) \times 10^{-7}$ is the probability of randomly paired events passing all the spatial and energy cuts. Figure 5.4 shows the random coincidence spatial distribution with no $|\mathbf{r}_p|$, $|\mathbf{r}_d|$, or ρ_d cuts. The large random coincidence background rate near the balloon is reduced by the fiducial volume cuts.

5.4 Cosmogenic background

Figure 5.5 shows the time to all previous scintillator muons applying all cuts except the 2 s muon cuts and prompt energy cut. The excess at short times to last scintillator muon suggests that these are radioactive backgrounds produced by muons passing

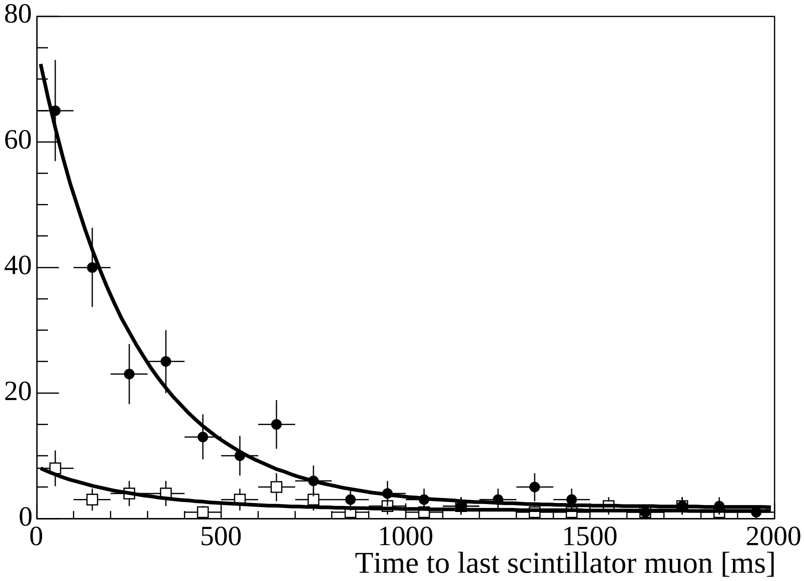

Figure 5.5: Candidate time to last muon with $\log_{10} Q_{muon} > 7.2$ OR bad muon track reconstruction (black circles), and time to last muon with $\log_{10} Q_{muon} < 7.2$ AND good muon track reconstruction AND distance to last muon track less than 3m (squares). Solid lines are exponential fits with a fixed half-life of $178.3\,\mu$s and a flat background.

through the scintillator. Muons produce radioactive isotopes by high-energy spallation, by neutron capture reactions, and by muon-induced nuclear disintegration[49]. Except for neutron capture, these reactions result in nuclei with lower atomic mass than the surrounding nuclei. Table 5.3 contains a list of radioactive nuclei which could mimic neutron inverse β decay and have atomic masses less than or equal to 16, the maximum atomic mass in the scintillator due to the presence of ^{16}O.

Fitting of the time to previous scintillator muons to the sum of exponentials with half-lives given in Table 5.3 and a flat background is consistent with 5.2±2.3 ^{9}Li decays after scintillator muons with $\log_{10} Q_{muon} < 7.2$ AND a good track, and 72±6 ^{9}Li decays after scintillator muons with $\log_{10} Q_{muon} > 7.2$ OR a bad track. Due to the ^{9}Li half-life, the fraction of ^{9}Li decays remaining after the 2 s cut is 0.04 %. For ^{9}Li decays within 2 s of a scintillator muon with $\log_{10} Q_{muon} < 7.2$ AND a good track, the fraction of events within 2 s not cut by the 3 m minimum radius to muon track is

Isotope	Half-life [ms]	Decay mode	Branching ratio [%]
^{8}He	119.0	β^{-}n	16
^{9}Li	178.3	β^{-}n	49.5
^{11}Li	8.5	β^{-}n, β^{-}2n, β^{-}3n	85, 4.1, 1.9
^{13}Be	17.36	β^{-}n	0.28
^{14}Be	4.35	β^{-}n, β^{-}2n	81, 5
^{16}C	747	β^{-}n	98.8

Table 5.3: Possible cosmogenic backgrounds.

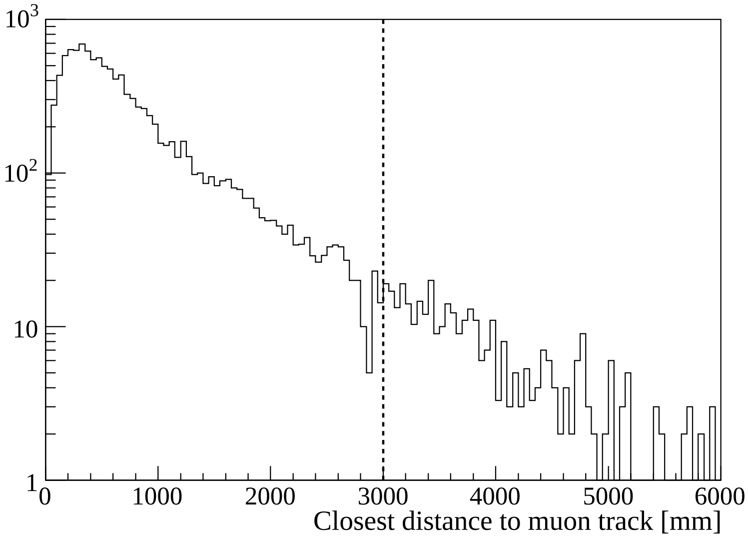

Figure 5.6: Neutron spatial distribution from muon track. The vertical line represents the 3 m cut following muon tracks with good tracks.

0.034±5.0 %, estimated from the fraction of spallation neutrons more than 3 m from the scintillator muon track, shown in Figure 5.6. This is a conservative estimate since the neutron probably drifts farther from the muon track.

^{9}Li decays to the 2.429 MeV, 2.780 MeV, 11.293 MeV, and 11.810 MeV excited states of ^{9}Be with branching ratios of 29.2 %, 15.6 %, 1.1 %, and 2.6 %, respectively [50]. The 2.429 MeV and 2.780 MeV excited states of ^{9}Be decay by neutron emission 9 % and ∼100 % of the time, respectively. The 11.293 MeV and 11.810 MeV excited states of ^{9}Be primarily decay into a neutron plus two α's. Figure 5.7 shows

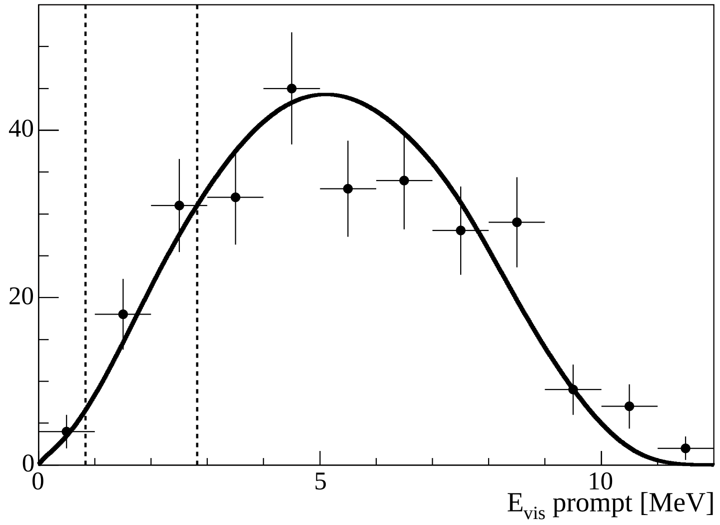

Figure 5.7: Energy spectrum of events within 2 s of muons, and within 3 m of muons with good track reconstructions and distance to candidate less than 3 m. Fitted with the expected ^{9}Li distribution. The vertical lines correspond to the prompt energy cut.

the energy spectrum of the events in Figure 5.5, including the expected ^{9}Li energy spectrum based on the ^{9}Li decay branching ratios. Integrating the expected energy spectrum between the prompt energy cuts, the probability of a ^{9}Li decay passing the prompt energy cut is 0.12.

Chapter 6

Analysis

As described in Section 1.6, the expected candidate rates due to terrestrial ^{238}U and ^{232}Th are estimated to be 29±5 and 7±1 per 10^{32} target protons per year, respectively, with a total of 36 ± 6 per 10^{32} target protons per year. The number of target proton-years in this data-set is $(2.63 \pm 0.19) \times 10^{31}$. Therefore the expected numbers of $\bar{\nu}_{\mathrm{e}}$ candidates due to terrestrial ^{238}U and ^{232}Th are estimated to be $N_U = 7.7 \pm 1.4$ and $N_{Th} = 1.9 \pm 0.4$, respectively, with a total of $N_U + N_{Th} = 9.6 \pm 1.8$. As described in Section 1.1, the ratio of ^{232}Th to ^{238}U concentrations, 3.7 to 4.1, is known better than the total concentrations. This results in a value of $\frac{N_U - N_{Th}}{N_U + N_{Th}}$ between 0.56 and 0.59, which does not depend strongly on the Earth model.

In the analysis presented here the number of terrestrial $\bar{\nu}_{\mathrm{e}}$ candidates is measured from both a rate only analysis, and an unbinned likelihood analysis of the total rate, prompt energy spectrum, and arrival time spectrum. The final result is based on the later analysis since this includes more information to distinguish backgrounds. An attempt is also made to measure the (α,n) background using pulse shape discrimination on the prompt scintillation light time distribution.

6.1 $\bar{\nu}_{\mathrm{e}}$ candidates

After the cuts described in Chapter 4, there are 103 $\bar{\nu}_{\mathrm{e}}$ candidates left in the dataset. Figure 6.1 shows the distribution of the prompt event energies including the main

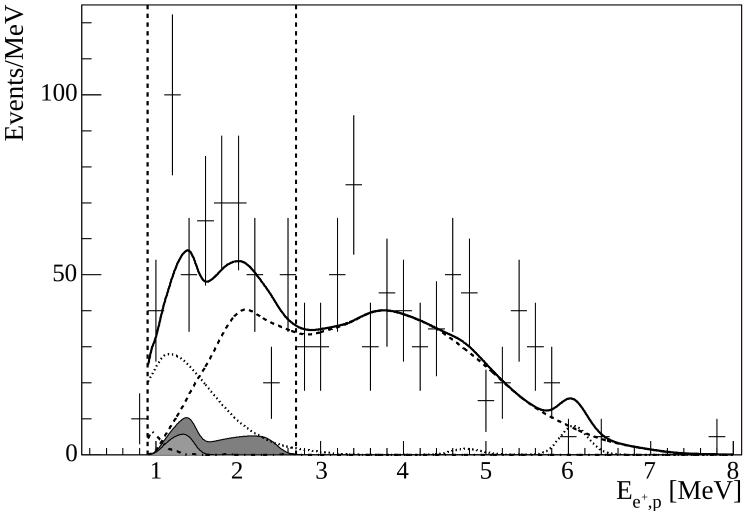

Figure 6.1: Distribution of prompt event energy including all the cuts except the prompt energy cut. The vertical lines define the analysis window. The shaded dark and light gray areas represent the expected number of terrestrial ^{238}U and ^{232}Th $\bar{\nu}_{\mathrm{e}}$ candidates based on terrestrial models. The dashed, dotted, and dot-dashed curves represent the expected reactor $\bar{\nu}_{\mathrm{e}}$, $^{13}\mathrm{C}(\alpha, \mathrm{n})^{16}\mathrm{O}$, and random coincidence backgrounds, respectively. The solid curve represents the expected prompt energy spectrum including all the background and expected terrestrial ^{238}U and ^{232}Th $\bar{\nu}_{\mathrm{e}}$ spectra.

backgrounds estimated in Chapter 5, and the expected terrestrial ^{238}U and ^{232}Th $\bar{\nu}_{\mathrm{e}}$ spectra. Figure 6.2 shows the distribution of delayed event energies as a function of time between the prompt and delayed events. The large number of events at low energies are due to random coincidences. As described in Section 4.2.7, there is a slight shift in the delayed event energy for times between the prompt and delayed event less than $30\,\mu$s due to the FEE dead-time. The $\bar{\nu}_{\mathrm{e}}$ candidates appear to be uniformly distributed within the fiducial volume, as shown in Figure 6.3. The large number of $\bar{\nu}_{\mathrm{e}}$ candidates near the balloon radius is consistent with the large number of random coincidences there. Uncorrelated events have a broad distribution of distances between the prompt and delayed events, whereas correlated events have a peak at short distances between them since they originate at the same position. Figure 6.4 shows that the candidates are consistent with being mostly correlated events.

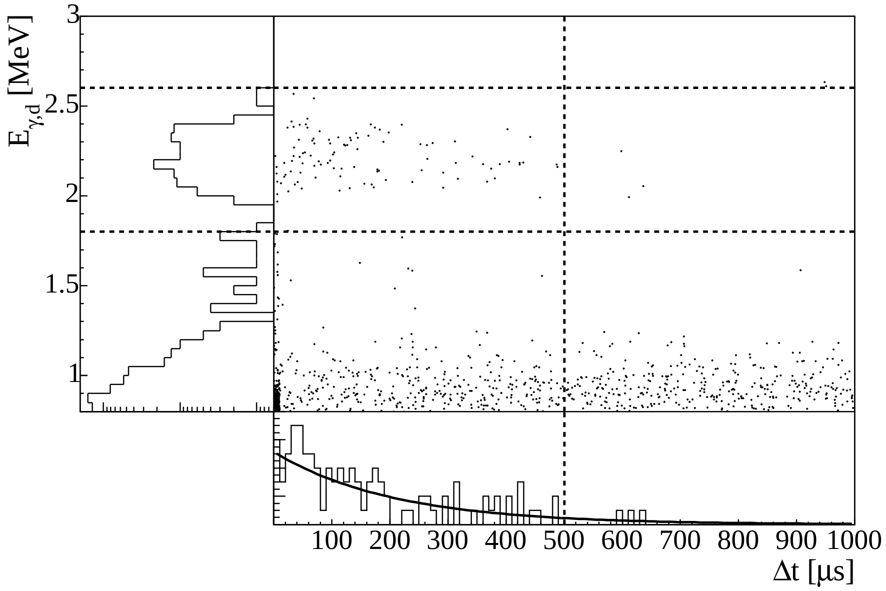

Figure 6.2: Distribution of delayed event energy as a function of time to prompt event including all the cuts except the delayed event energy and time between events cuts. The vertical dashed line represents the cut on maximum time between events, and the horizontal dashed lines represent the upper and lower delayed energy cuts. The bottom histogram only contains events passing the delayed energy cut and includes an exponential fit with the measured mean neutron capture time of 205.9 μs. The left histogram only contains events passing the time between events cut.

6.2 Pulse shape discrimination

The scintillation light time structure depends on the energy loss density. The scintillation light from neutron inverse β decay prompt events is caused by e^+'s, whereas the scintillation light from (α,n) background prompt events is caused by neutron thermalization. These have different energy loss densities and may produce different prompt event scintillation light time structures, which could be used to separate the two samples. This is a standard technique that can result in very good distinguishing power[51]. The distinguishing power obtainable in KamLAND is reduced because of the high concentration of dodecane in the scintillator.

The e^+ scintillation light time distribution can not be measured since we do not have a e^+ source. However, we have γ sources, which should have a similar scintillation

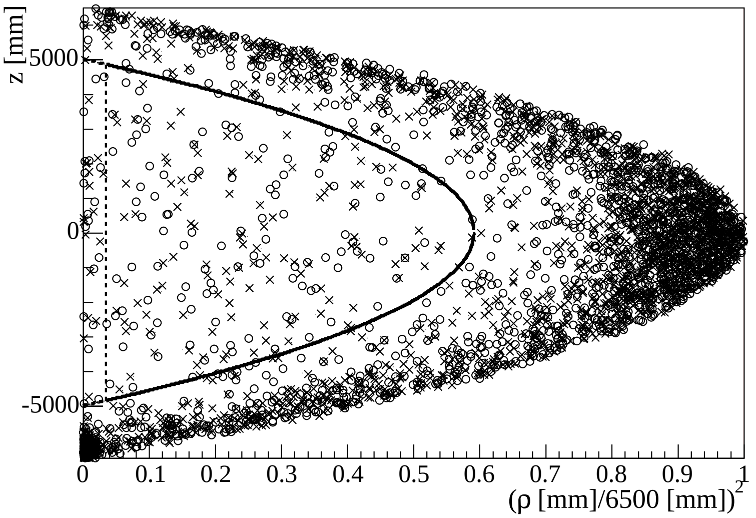

Figure 6.3: Prompt(circle) and delayed(cross) vertex distributions including all the cuts except the $|\mathbf{r}_p|$, $|\mathbf{r}_d|$, or ρ_d cuts. The solid line represents the delayed fiducial volume cut. The dashed line represents the prompt fiducial volume cut; this is equivalent to the delayed fiducial volume cut at large ρ.

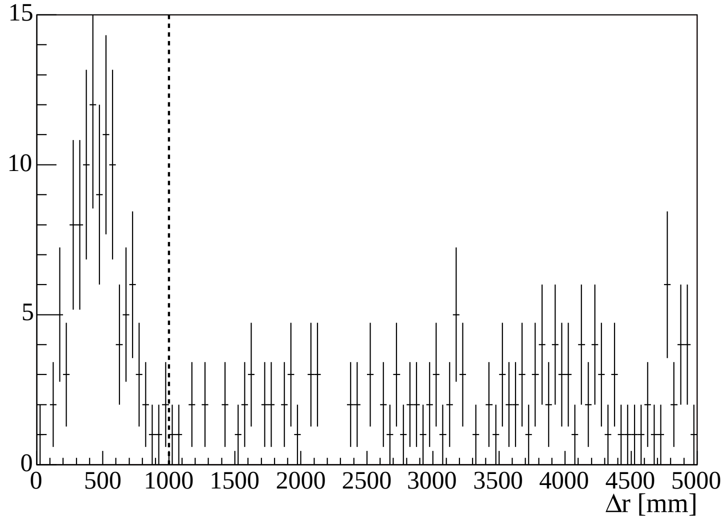

Figure 6.4: Distribution of distance between prompt and delayed events including all the candidate cuts except the $|\mathbf{r}_p - \mathbf{r}_d|$ cut. The vertical line represents the maximum distance between events cut.

light time structure to e^+ events since a e^+ produces two $0.511\,\mathrm{MeV}$ γ rays when it annihilates with an e^-. Therefore, the pulse shape discrimination algorithm is developed using $^{241}\mathrm{Am}^9\mathrm{Be}$ source data. Figure 6.5 shows the scintillation light time distributions for $^{241}\mathrm{Am}^9\mathrm{Be}$ n_0 neutron events, $n(t)$, and neutron capture γ rays, $\gamma(t)$, with the same "visible" energy. $\gamma(t)$ has a slightly higher peak, and faster decrease than $n(t)$. The approximately constant value at early times is due to the PMT dark noise. To distinguish two different scintillation light time distributions, a general particle identification parameter is defined by

$$S = \int_0^\infty dt\, P(t) g(t), \tag{6.1}$$

where $P(t)$ is a weighting function, and $g(t)$ is the scintillation light time distribution. Assuming poisson fluctuations in the number of scintillation photons and ensuring $\int_0^\infty dt\, n(t) = \int_0^\infty dt\, \gamma(t)$, the difference between S for γ rays and neutrons is maximized[52] if

$$P(t) = \frac{\gamma(t) - n(t)}{\gamma(t) + n(t)}. \tag{6.2}$$

The γ rays have $E_{vis} \approx 2.3\,\mathrm{MeV}$, therefore $\gamma(t)$ is calculated at this energy, $\gamma_2(t)$. $n(t)$ is then calculated at the same energy, $n_2(t)$. The lower plot of Figure 6.5 shows the resulting $P(t)$. Assuming that the number of scintillation photons scales with energy and the dark rate is constant, the weighting function as a function of E_{vis} is given by

$$P(E_{vis}, t) = \frac{\gamma_2(t) - n_2(t)}{\gamma_2(t) + n_2(t)} \left[1 + \frac{2B}{\gamma_2(t) + n_2(t)} \left(\frac{2.3}{E_{vis}[\mathrm{MeV}]} - 1\right)\right]^{-1}, \tag{6.3}$$

where B is the PMT dark rate.

Due to re-emission, in which a scintillation photon is absorbed by the scintillator and then re-emitted at a random angle, the scintillation light time distribution depends on the path length in the scintillator between the vertex and the PMT, d_{scint}. Therefore $P(E_{vis}, t)$ is calculated for d_{scint} between $2\,\mathrm{m}$ and $12\,\mathrm{m}$ using data from the $^{241}\mathrm{Am}^9\mathrm{Be}$ source deployed at different positions on the z-axis.

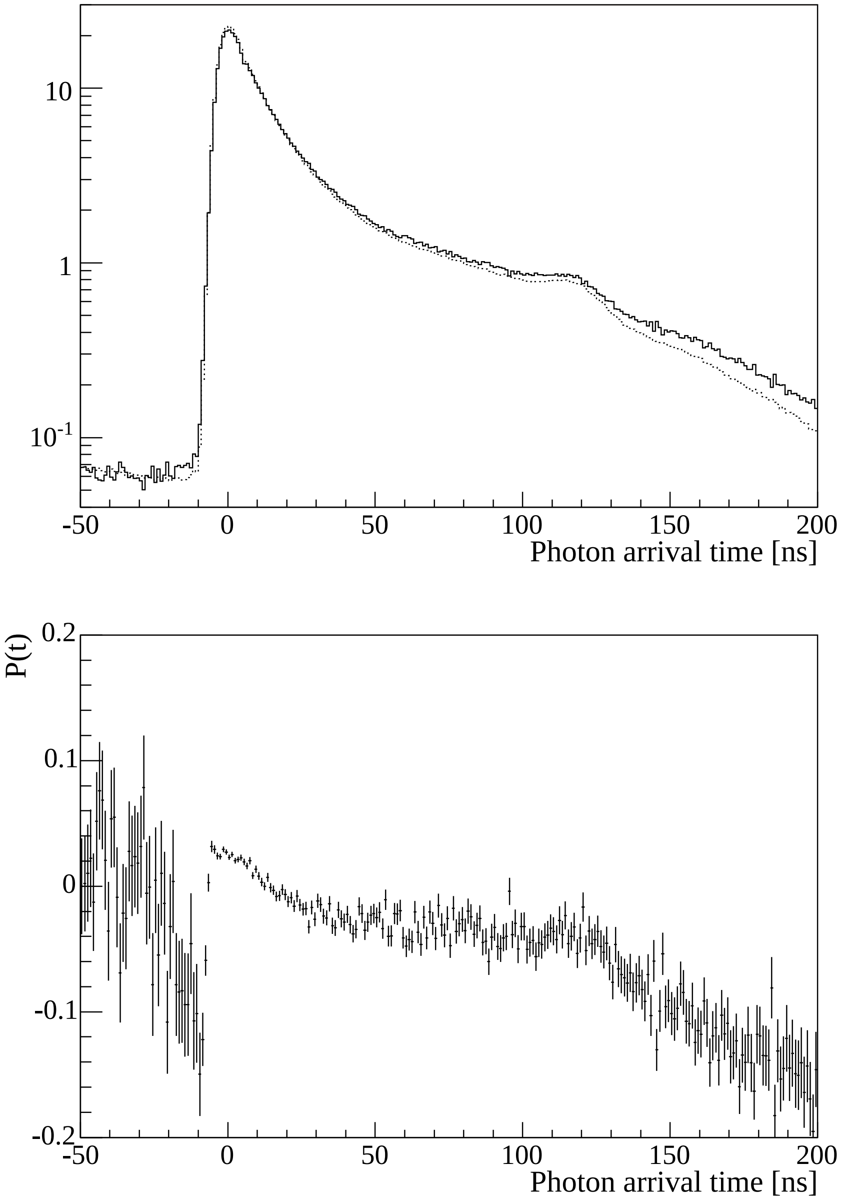

Figure 6.5: The upper plot shows the scintillation light time distributions for ^{241}Am^{9}Be n_0 neutron events (solid) and neutron capture γ's (dashed). The lower plot shows the difference in these distributions divided by the total of the two, $P(t)$.

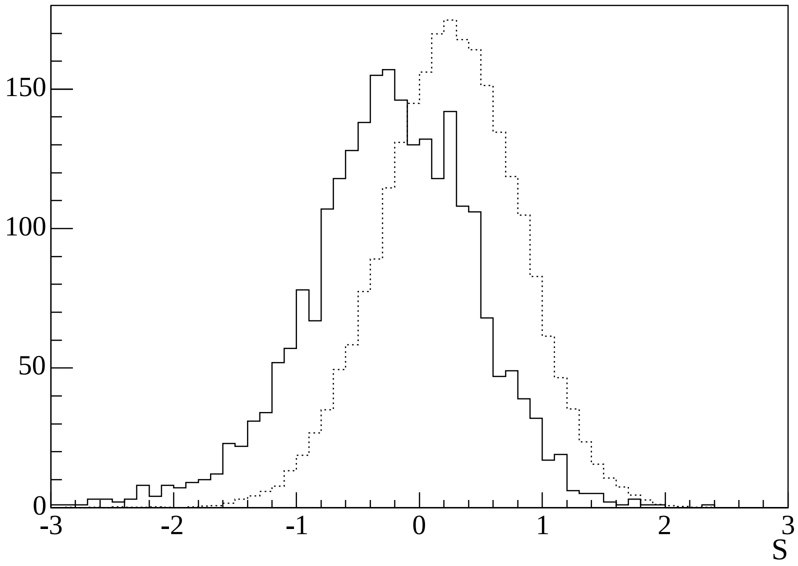

Figure 6.6: Pulse shape discrimination parameter for ∼2.3 MeV neutrons(solid) and γ's(dotted).

Figure 6.6 shows the distribution of S for neutron events, S_n, and γ events, S_γ. From a Gaussian fit the mean of $S_n(S_\gamma)$ is $-0.22 \pm 0.01(0.25 \pm 0.01)$ with a sigma of $0.64 \pm 0.01(0.56 \pm 0.01)$. Figure 6.7 shows that the mean and sigma of S_n and S_γ are reasonably stable as a function of energy and position. Assuming the S distribution is the same for γ and e^+ like events, the fraction of neutron backgrounds with respect to the total number of $\bar{\nu}_{\mathrm{e}}$ candidates, f_n, can be estimated by fitting the candidate prompt event S distribution with

$$P(S) = N \left[f_n G_{\mu=-0.22,\sigma=0.64}(S) + (1 - f_n) G_{\mu=0.25,\sigma=0.56}(S) \right], \tag{6.4}$$

where N is an overall normalization, and $G_{\mu,\sigma}(S)$ is a Gaussian distribution with mean of μ and variance of σ^2. Based on this fit, the estimated number of (α,n) background events is 51 ± 20. This measurement suggests that the number of (α,n) background events is greater than zero and slightly higher than the 21.9 ± 4.2 background events calculated in Section 5.2.1.

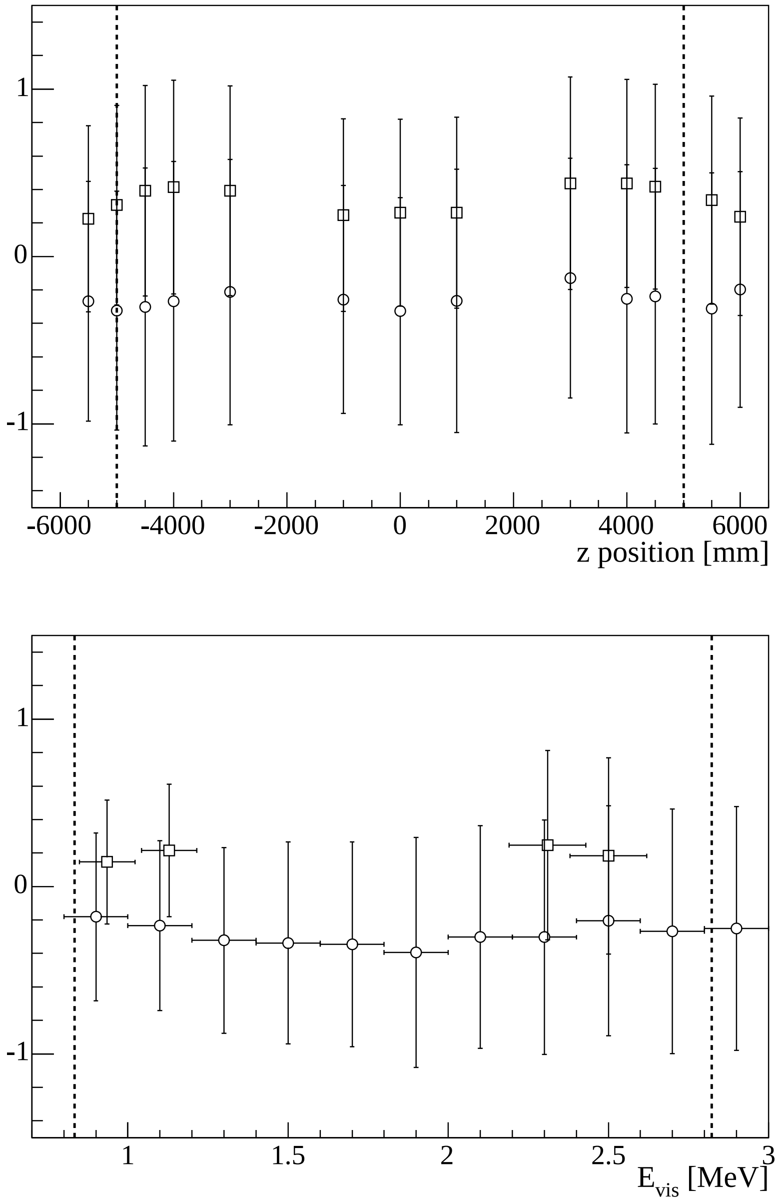

Figure 6.7: Mean of the pulse shape discrimination parameter for neutrons(circles) and γ rays(squares), where the vertical error bars represent the RMS of the distribution. The upper plot shows the variation as a function of ^{241}Am^{9}Be source deployment position for $\sim$2.3 MeV events, and the lower plot shows the variation as a function of energy. The vertical lines represent the upper and lower limits of the cuts.

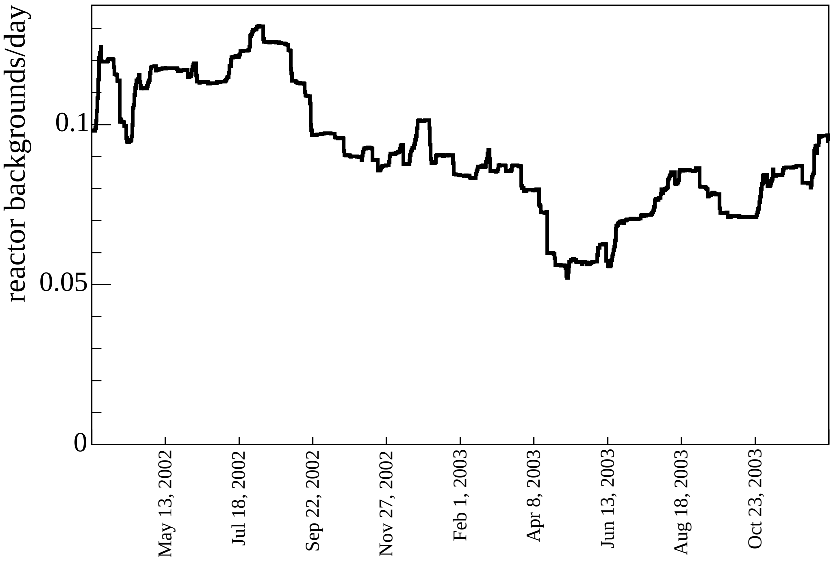

Figure 6.8: Time variation in reactor $\bar{\nu}_e$ background.

6.3 Rate analysis

Subtracting the number of background events in Chapter 5, the estimated number of terrestrial ^{238}U and ^{232}Th $\bar{\nu}_e$ candidates is 31±12. And the 95 % confidence interval is 7.4 to 55.4, which excludes zero and includes the expected signal.

6.4 Likelihood analysis

In another analysis method the prompt event energy and the absolute event time are used to distinguish terrestrial $\bar{\nu}_e$'s from background events. Unlike terrestrial $\bar{\nu}_e$ candidates, the reactor $\bar{\nu}_e$ background varies as a function of time, as shown in Figure 6.8. The prompt energy and time spectra analysis is performed with an unbinned maximum likelihood fit[53] since the binning process results in some loss of information. This extra information is important given the modest number of candidates.

To constrain the neutrino oscillation parameters, the spectral analysis is performed with a prompt energy cut of $0.9\,\mathrm{MeV} < E_{e^+,p} < 8.0\,\mathrm{MeV}$, which includes the entire reactor $\bar{\nu}_{\rm e}$ spectrum. Although this analysis has different cuts from the KamLAND reactor analysis[21], many of the candidates are common. To avoid using the same data twice, the neutrino oscillation parameters determined in the KamLAND reactor analysis can not be included in this likelihood analysis. However, the neutrino oscillation parameters determined from solar neutrino experiments[54] are included since these are completely independent analyses.

Given N_U and N_{Th} terrestrial ^{238}U and ^{232}Th $\bar{\nu}_{\rm e}$ candidates, respectively, the expected number of candidates with prompt energy, E_{e^+}, at time t_i is given by

$$\begin{aligned} \frac{dN}{dE\,dt}(E_{e^+}, t_i) &= \frac{N_U}{T}\frac{dN_U}{dE}(E_{e^+}) + \frac{N_{Th}}{T}\frac{dN_{Th}}{dE}(E_{e^+}) \\ &\quad + p_r \frac{dN_r}{dE\,dt}(E_{e^+}, t_i, \Delta m_{12}, \sin 2\theta_{12}) + \sum_j \frac{p_j}{T}\frac{dN_j}{dE}(E_{e^+}), \end{aligned} \tag{6.5}$$

where T is the livetime, and $\frac{dN_U}{dE}(E_{e^+})$ and $\frac{dN_{Th}}{dE}(E_{e^+})$ are the expected $\bar{\nu}_{\rm e}$ energy spectra for terrestrial ^{238}U and ^{232}Th, respectively. $\frac{dN_r}{dE}(E_{e^+}, t_i, \Delta m_{12}, \sin 2\theta_{12})$ is the reactor $\bar{\nu}_{\rm e}$ energy spectrum at time t_i for neutrino oscillation parameters Δm_{12} and $\sin 2\theta_{12}$, and p_r is a scaling of the expected reactor spectrum. The sum is over the other known backgrounds, $\frac{dN_j}{dE}(E_{e^+})$ is the expected energy spectrum for background j, and p_j is a background scaling. The total number of candidates expected, $\overline{N}$, is obtained by integrating Equation 6.5 over the prompt energy and livetime.

The log likelihood for observing the total event rate, prompt energy spectrum, and arrival time spectrum, is given by

$$\log L = -\overline{N} + \sum_{i=1}^{N} \log\left[\frac{dN}{dE\,dt}(a_0 E_i + a_1, t_i)\right] - \frac{1}{2}\chi_p^2, \tag{6.6}$$

where N is the observed number of candidates, E_i is E_{e^+} for event i, the energy scale is allowed to vary linearly with a slope a_0 and offset a_1, and χ_p^2 is a penalty term for varying measured parameters within their error ranges. χ_p^2 is given by

$$\begin{aligned}\chi_p^2 &= \left(\frac{p_r - 1}{\sigma_r}\right)^2 + \sum_j \left(\frac{p_j - 1}{\sigma_j}\right)^2 \\ &\quad + \sum_{k=1}^{3} \left[\frac{(a_0 - 1)E_k^{cal} + a_1}{\sigma_{E_k^{cal}}}\right]^2 + \Delta\chi_{sol}^2(\Delta m_{12}, \sin 2\theta_{12}), \qquad (6.7)\end{aligned}$$

where σ_r and σ_j are the fractional errors in the reactor background and background j's measured rates, respectively. $\sigma_{E_k^{cal}}$ is the error in the energy scale at energy E_k^{cal}, and $\Delta\chi_{sol}^2(\Delta m_{12}, \sin 2\theta_{12})$ is the $\Delta\chi^2$ term for neutrino oscillation parameters Δm_{12} and $\sin 2\theta_{12}$ obtained from solar neutrino experiments[54].

The best fit point is obtained by varying N_U, N_{Th}, a_0, a_1, Δm_{12}, $\sin 2\theta_{12}$, p_r, and the p_j's until $\log L$ is maximized. A $\Delta\chi^2$ is defined by

$$\Delta\chi^2 = 2(\log L_{max} - \log L), \qquad (6.8)$$

where $\log L_{max}$ is the log likelihood at the best fit point. The confidence interval for m parameters is obtained by calculating $\Delta\chi^2$ as a function of the m parameters, varying the other parameters to maximize $\log L$ at that point. For a one(two) parameter confidence interval the 68 %, 90 %, and 95 % confidence intervals are defined by $\Delta\chi^2$ less than 1.00(2.30), 2.71(4.61), and 3.84(5.99), respectively. Figure 6.9 shows the 68 %, 90 %, and 95 % confidence intervals obtained as a function of $N_U + N_{Th}$ and $\frac{N_U - N_{Th}}{N_U + N_{Th}}$. Figure 6.9 also includes the expected $N_U + N_{Th}$ and $\frac{N_U - N_{Th}}{N_U + N_{Th}}$. The data does not have much distinguishing power on $\frac{N_U - N_{Th}}{N_U + N_{Th}}$.

Assuming $\frac{N_U - N_{Th}}{N_U + N_{Th}} = 0.6$ from geophysical data, Figure 6.10 shows the 68 %, 90 %, and 95 % confidence intervals as a function of $N_U + N_{Th}$. The best fit point at $N_U + N_{Th} = 21$ is lower than the value of 31 obtained in Section 6.3. This is because the likelihood analysis favors slightly high values for the reactor $\bar{\nu}_e$ and (α,n) backgrounds. At this best point the neutrino oscillation parameters are $\Delta m_{12} = 7.4 \times 10^{-5}\,\mathrm{eV}^2$ and $\sin^2 2\theta_{12} = 0.837$, which are consistent with the KamLAND reactor analysis[21]. Figure 6.11 shows the expected prompt energy spectrum for this best fit point.

Figure 6.12 shows the expected terrestrial ^{238}U $\bar{\nu}_e$ detection rate at KamLAND as

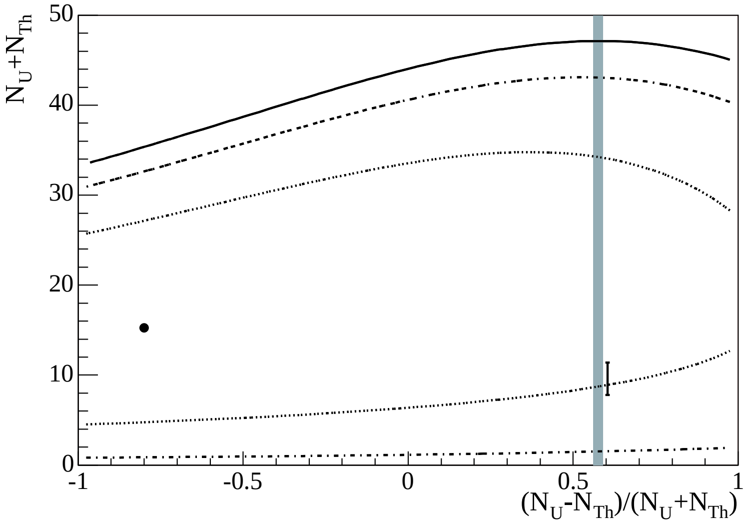

Figure 6.9: 68 % (dot-dashed), 90 % (dashed), and 95 % (solid) confidence intervals for the number of terrestrial ^{238}U and ^{232}Th $\bar{\nu}_e$'s. The best fit point is marked by a solid circle. The vertical shaded area represents the expected $\frac{N_U-N_{Th}}{N_U+N_{Th}}$, and the expected $N_U + N_{Th}$ is marked by error bars.

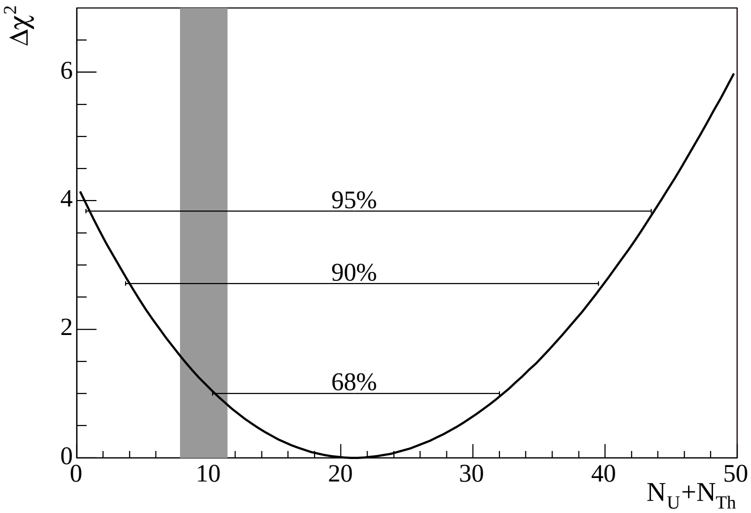

Figure 6.10: 68 %, 90 %, and 95 % confidence intervals for the total number of terrestrial ^{238}U and ^{232}Th $\bar{\nu}_e$'s having fixed $\frac{N_U-N_{Th}}{N_U+N_{Th}}$ to 0.6. The vertical shaded area represents the expected value of $N_U + N_{Th}$.

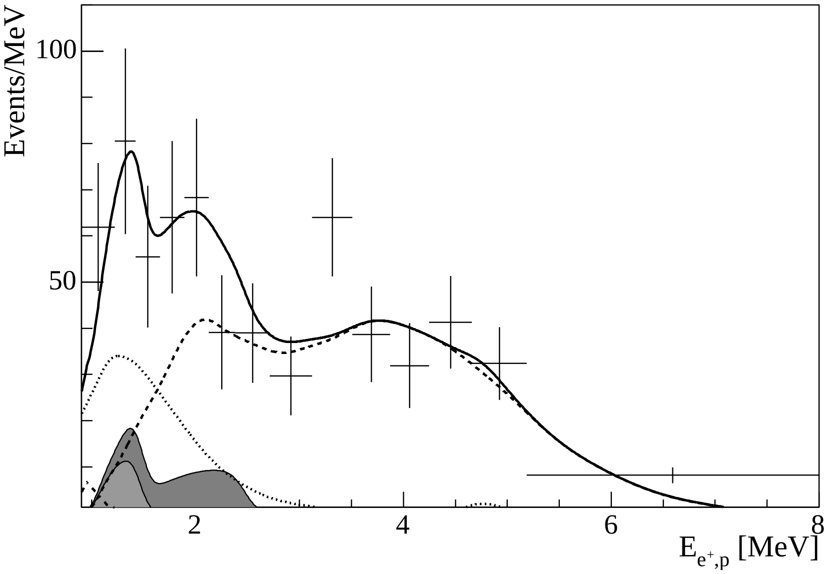

Figure 6.11: Distribution of prompt event energy. The shaded dark(light) gray area represents the best estimate for the number of terrestrial ^{238}U(^{232}Th) $\bar{\nu}_e$ candidates. The dashed, dotted, and dot-dashed curves represent the best fit reactor $\bar{\nu}_e$, $^{13}C(\alpha, n)^{16}O$, and random coincidence backgrounds, respectively. The solid curve represents the best fit prompt energy spectrum including all the background and terrestrial ^{238}U and ^{232}Th $\bar{\nu}_e$ spectra.

a function of the total terrestrial ^{238}U mass[55]. The shaded band represents a three sigma expected region obtained from a detailed study of the ^{238}U concentrations near KamLAND. The lower limit assumes the total terrestrial ^{238}U mass is equal to what is observed in the continental crust. The upper limit assumes that all the measured heat dissipation rate from the Earth is due to radiogenic heat generation. Tighter terrestrial ^{238}U mass limits are obtained from BSE models. The 90 % confidence interval of the measured ^{238}U $\bar{\nu}_e$ detection rate at KamLAND can not exclude any of these assumptions for the total terrestrial ^{238}U mass.

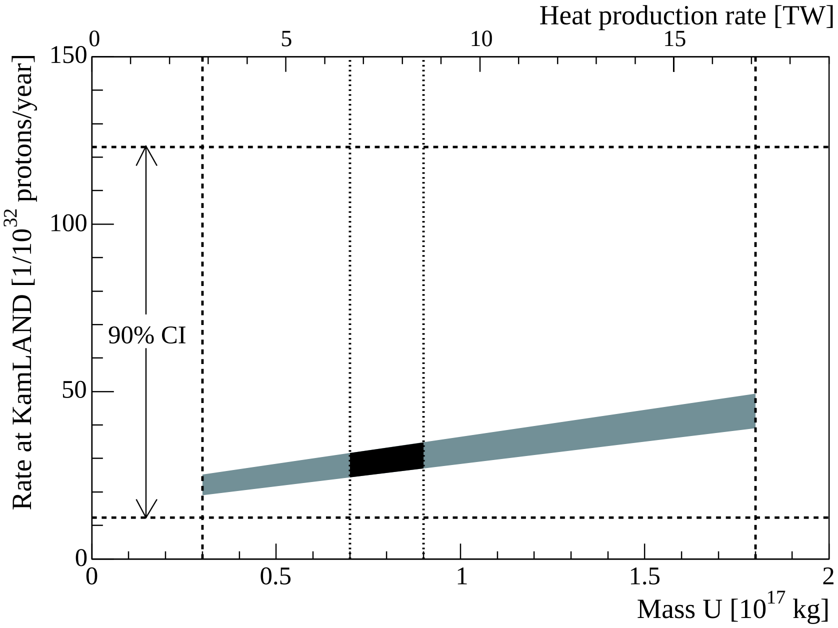

Figure 6.12: The dashed vertical lines represent the lower and upper limit on the total terrestrial ^{238}U mass, respectively. The dotted vertical lines represent the lower and upper limit on the total terrestrial ^{238}U mass assuming BSE Earth models. The gray area represents the three sigma confidence interval for the expected ^{238}U $\bar{\nu}_\mathrm{e}$ detection rate at KamLAND as a function of the total terrestrial ^{238}U mass. The black region is the same region assuming BSE Earth models. The horizontal lines represents the 90 % confidence interval for the measured ^{238}U $\bar{\nu}_\mathrm{e}$ detection rate at KamLAND.

Chapter 7

Conclusions

Based on $(2.63 \pm 0.19) \times 10^{31}$ target proton-years of data collected with KamLAND between March, 2002 and December, 2003, we have measured the total number of terrestrial ^{238}U and ^{232}Th $\bar{\nu}_{\mathrm{e}}$ candidates, $N_U + N_{Th}$, and the difference to the sum fraction, $\frac{N_U - N_{Th}}{N_U + N_{Th}}$. An unbinned likelihood analysis of the total event rate, energy spectrum, and time spectrum, is not very sensitive to $\frac{N_U - N_{Th}}{N_U + N_{Th}}$. Restricting $\frac{N_U - N_{Th}}{N_U + N_{Th}}$ to 0.6, which is robustly predicted from Earth models, the 90 % confidence interval of $N_U + N_{Th}$ is 4 to 40. This agrees with the expected value of 9.6 ± 1.8, but does not exclude any reasonable geophysical model. This $N_U + N_{Th}$ confidence interval is consistent with that obtained from an analysis of only the total event rate.

Currently the error in this analysis is dominated by the statistical error, which is large due to the large number of background events. The relative importance of this error will decrease as a function of time. With approximately four times more data the contribution from the statistical error should be approximately equivalent to the background error. Since the background error is mostly not statistics dominated, it should increase linearly with data size, which will then limit any further improvement in the measured terrestrial ^{238}U and ^{232}Th $\bar{\nu}_{\mathrm{e}}$ candidate rates. This will probably result in a factor of approximately two improvement in the measured rate. There is a planned purification of the KamLAND scintillator within the next two years. This should substantially reduce the ^{210}Pb concentration in the scintillator which would reduce the $(\alpha$,n) background. Also the largest error in the reactor background is due to uncertainty in the value of $\sin^2 2\theta_{12}$, which will hopefully be reduced with new results from SNO.

With more data and smaller background errors KamLAND may exclude some geophysical models. However, a precision measurement will probably require a bigger detector located away from nuclear reactors. The present data is the first measurement of the terrestrial ^{238}U and ^{232}Th $\bar{\nu}_{\mathrm{e}}$ rates, and will hopefully lead to future precision measurements.

Appendix A

Front-end electronics

Table A.1 lists FEE commands, with a brief description of each below:

- Global Acquisition: The FEE digitizes waveforms acquired due to the input signal crossing above the discriminator threshold in the previous ∼400 ns. Waveforms are acquired from all gains and then digitized in order of decreasing gain until the waveform does not have any ADC value above 1000; note that the maximum ADC value is 1023.

- Forced Acquisition: The FEE acquires then digitizes waveforms from either ATWD A, ATWD B, or whichever ATWD is available (No Priority). Waveforms are acquired from all gains when the FEE receives this command irrespective of whether the input signal crossed the discriminator threshold. The gains are then digitized in order of decreasing gain until the waveform does not have any ADC value above 1000; note that the maximum ADC value is 1023.

- Pedestal: The FEE acquires then digitizes waveforms from all signal inputs to either ATWD A or ATWD B. Waveforms are acquired when the FEE receives this command irrespective of whether the input signal crossed the discriminator threshold.

- Acquire Clock: The FEE acquires then digitizes waveforms from the clock input to either ATWD A or ATWD B.

- Reset Timestamp: The FEE resets its timestamp to zero.
- Test Pulser No Acquisition: The FEE deposits a predetermined charge at the input of channels enabled by the test pulser enable mask[1].
- Test Pulser Self Launching: The FEE deposits a predetermined charge at the input of channels enabled by the test pulser enable mask[1]. If the input signal crosses the discriminator threshold, then the waveform is acquired and digitized with either ATWD A or ATWD B.
- Test Pulser Forced Acquisition: The FEE deposits a predetermined charge at the input of channels enabled by the test pulser enable mask[1], then acquires and digitizes waveforms with either ATWD A or ATWD B.
- Increment Test Pulser Enable: The test pulser enable mask[1] number is incremented by one.
- Reset FPGA's: The FEE resets its FPGA's to the power up state.

---

[1] The test pulser enable mask is a 12-bit number, where each bit corresponds to one input channel. If the bit associated with an input channel equals one then that channel responds to test pulser commands.

Hex Command	Description
0x01	Global Acquisition
0x02	Forced Acquisition, ATWD A
0x03	Forced Acquisition, ATWD B
0x04	Acquire Clock, ATWD A
0x05	Acquire Clock, ATWD B
0x06	Reset Timestamp
0x07	Forced Acquisition, No Priority
0x08	Test Pulser Self Launching, ATWD A
0x09	Test Pulser Self Launching, ATWD B
0x0a	Test Pulser Forced Acquisition, ATWD A,
0x0b	Test Pulser Forced Acquisition, ATWD B,
0x0c	Test Pulser No Acquisition
0x12	Pedestal, ATWD A
0x13	Pedestal, ATWD B
0x1d	Reset FPGA's
0x1e	Increment Test Pulser Enable

Table A.1: FEE commands.

Appendix B

MACRO electronics

The FEE sums the voltages from six PMT's and sends it to the MACRO electronics, which provides an alternative system for recording waveforms. The MACRO electronics are arranged as 9U VME modules in 4 VME crates. Each crate has one VME I/O register with interrupt and a VME readout connected to its own computer. Each module has one waveform digitizer (WFD) and 16 input channels with separate discriminators whose thresholds are set by the DAQ. The 16 input channels are grouped into four sets of four. An 8-bit ADC converts the summed voltage from each group into a digital signal which is recorded as well as a 16-bit record of which input channels are above each of their thresholds.

The WFD has a 2048 sample long circular memory, as shown in Figure B.1. After data fills the last memory address, the next data fills the first memory address. The WFD samples data at 200 MHz, or every 5 ns, which corresponds to a total of 10.24 μs of data in the memory. However, the MACRO electronics have zero suppression enabling them to record longer than the previous 10.24 μs; data is only recorded if any of the 16 input channels is above its threshold. The MACRO electronics also record the number of 200 MHz clock samples, time word, to reconstruct the time structure of the input.

As well as having 16 input signals, each MACRO module has two pulsed NIM inputs to start and a stop signal digitization by the WFD. A fan-out board below each crate takes a start or stop signal and sends it to all the MACRO modules in

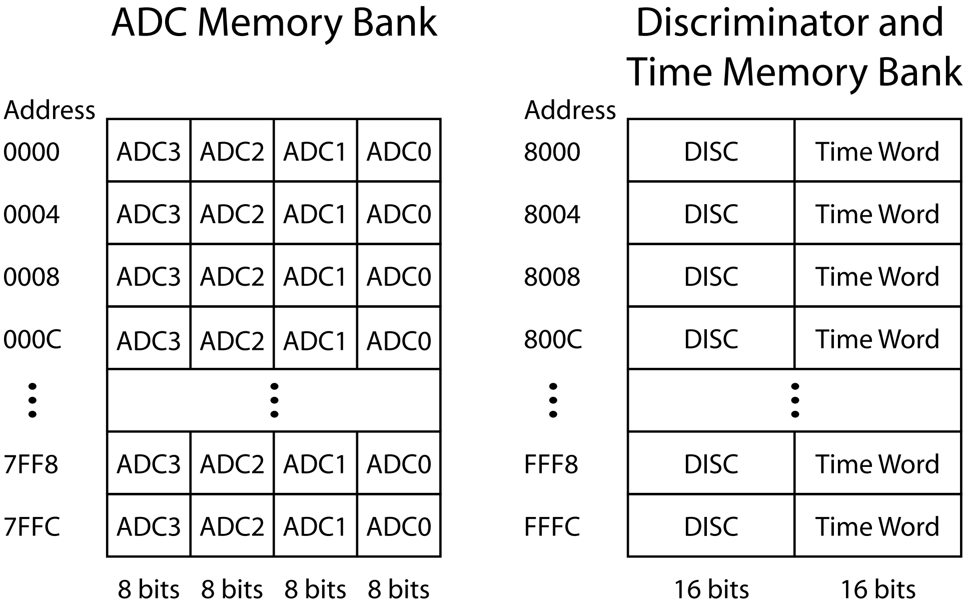

Figure B.1: WFD memory layout. ADC0 - ADC3 stores the summed voltage from the 4 input groups. DISC stores the input channels above its discriminator threshold. Time Word stores the number of 200MHz clock-ticks.

the VME crate. The VME I/O register in each crate issues a pulsed start signal at the start of each run. Based on the triggers described in Appendix C.2.3, the trigger module generates and sends a stop command to all MACRO modules, and all crates' VME I/O registers. The VME I/O register generates an interrupt causing the DAQ to readout a length of data, from all modules in that VME crate. Two types of stop commands, a long stop and a short stop, are sent to different inputs of the VME I/O register. The DAQ sets the readout times, which are 1 ms and 150 μs for the long and short stops, respectively. Once each MACRO VME crate is ready to record new data after all the previous data is recorded the DAQ instructs the VME I/O register to generate a pulse start signal sent to each MACRO module in the VME crate. The DAQ then instructs the VME I/O register to generate a logic level ready signal which is sent to a coincidence module. When the coincidence module receives a ready signal from all four MACRO VME I/O registers a global ready signal is sent to the trigger module, enabling another stop command to be sent to the MACRO electronics.

Appendix C

Trigger

C.1 Hardware

Figure C.1 shows the main components of the trigger module and how they communicate with the DAQ. The trigger board contains a 40 MHz clock, which is distributed to all FEE modules to keep them synchronized with the trigger board. The trigger board does not contain its own data transfer standard; instead it communicates with DAQ via commercial VME output registers and latches[1]. The output register and latches use ECL outputs and inputs, respectively.

Every clock-tick the trigger module receives $\mathrm{N_{FEE}}$ from all 200 FEE modules, where each of these is a 4-bit LVPECL signal, which corresponds to a total of 800 inputs. Based on these inputs, the trigger board must issue a global acquisition command to the FEE within ∼400 ns. To achieve this, the trigger board uses FPGA's[56] to perform calculations. These perform the highly parallel calculations necessary, have a large number of inputs and outputs[2], and are reprogrammable, allowing for development of new trigger algorithms.

Figure C.2 shows a schematic of the trigger board. The 800 LVPECL signals from the FEE modules are converted to LVTTL signals before being sent to the

---

[1] Although easy to develop, this is the slowest part of the trigger module and could easily be incorporated into the trigger board if a new board were to be developed.

[2] The largest number of I/O's available was ∼500 at the time the trigger module was designed in 2000.

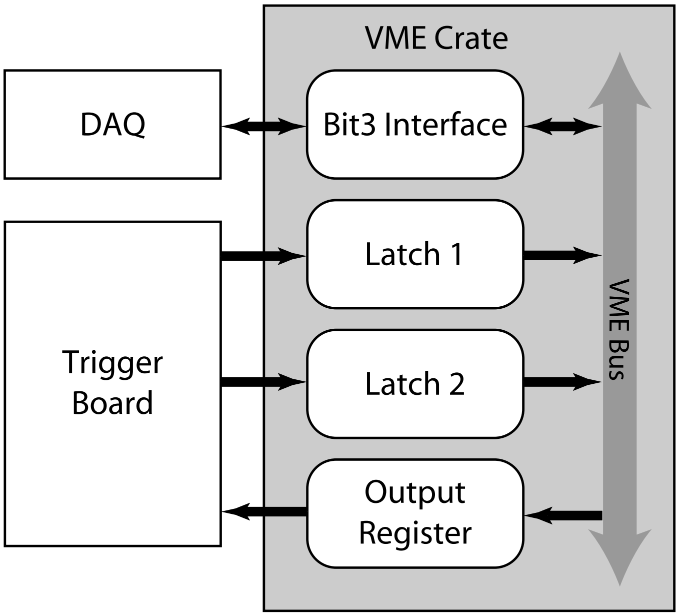

Figure C.1: An overview of the main trigger module components and the communication among them.

FPGA's. This has two advantages: the converter chips act as a buffer to the expensive FPGA chip, and LVTTL signals require only one input line referenced to ground while LVPECL signals require two input lines. Because of the large number of inputs, two input FPGA's perform initial calculations and pass the reduced information to a third FPGA. The third FPGA then combines the information from the first two FPGA's. The ECL signals from the output register are converted to TTL signals and sent to the third FPGA. TTL signals from the third FPGA are converted to ECL signals and sent to latch 1 and 2. FEE commands are generate by the third FPGA and converted to LVPECL signals before being sent to a fan-out board and then to each FEE VME crate. MACRO electronics stop commands are generated by the third FPGA and converted to ECL signals before being sent to an ECL to NIM converter and then to the MACRO electronics.

Each FPGA is mounted on a separate daughterboard, which can be removed from the trigger motherboard. Each daughterboard contains all the components necessary to run the FPGA, all the other components are contained on the motherboard. These three daughterboards are identical except for the code stored on the PROM. This code

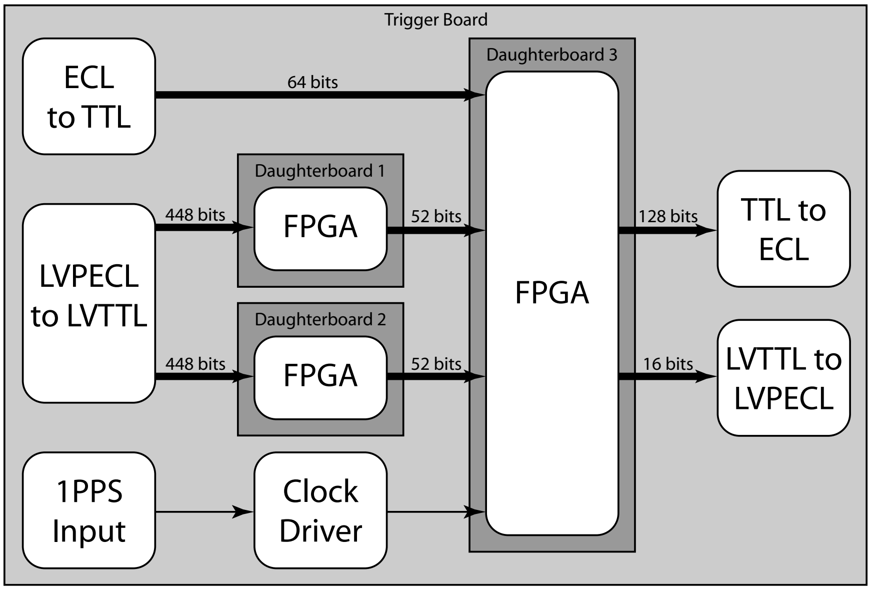

Figure C.2: An overview of the trigger board.

is transferred to the FPGA on power up.

C.1.1 GPS

For timing between events within a run it is sufficient to use the timestamp. However, if KamLAND were to detect a supernova, it may be possible to use the difference in arrival times at different detectors around the world to determine the location of the supernova. In order to compare times at different detectors, it is necessary to know the absolute time precisely. The trigger module records the absolute time obtained from a Global Positioning System (GPS) receiver. The GPS receiver uses time signals from the GPS satellites to calculate the absolute time and position of the receiver. The absolute time is accurate to 100 ns of Universal Time Co-ordinates (UTC). The GPS receiver also generates a One Pulse Per Second (1PPS) output accurate to 150 ns of the UTC second.

Figure C.3 shows a schematic of the GPS timing system. The GPS receiver must be located outside the mine in order to receive signals from the satellites. The trigger module must be located inside the mine to issue commands to the FEE. Therefore, the

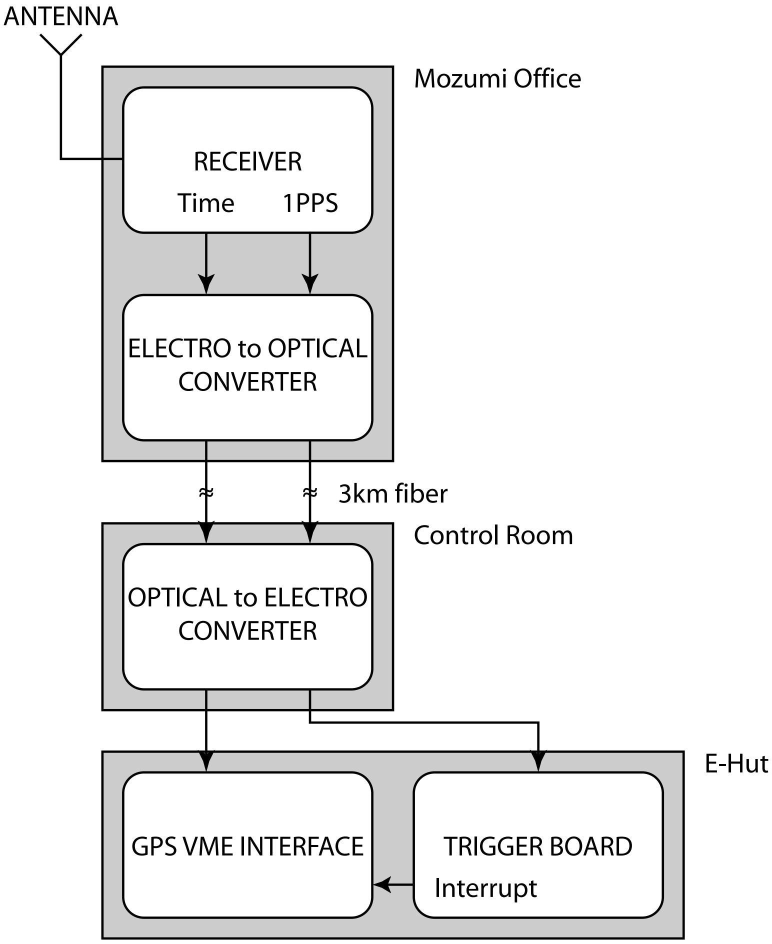

Figure C.3: Schematic of the GPS timing system.

time, encoded in a serial digital format, and 1PPS signal are converted into optical signals and sent into the mine. The encoded time is connected to a GPS VME interface, which is accurate to only 1 μs of UTC due to the nature of the encoded time. The time is recorded by the GPS VME interface when it receives an interrupt signal issued by the GPS trigger described in Appendix C.2.4. GPS triggers are issued two clock-ticks after the 1PPS signal, allowing timing accuracy of the 1PPS signal, $\sim$150 ns to UTC. Timestamps are then correlated to UTC since the timestamp is recorded when the GPS trigger is issued.

C.2 Firmware

The DAQ communicates the run conditions to the trigger module using serial transfer on the 32-bit output register: 16 bits for data transfer, and 5 bits identifying the data being transferred. The remaining bits of the output register define commands such as run start and run end. The run start command causes the trigger module to start issuing triggers, the trigger module timestamp to be reset to zero, and a reset timestamp command to be sent to the FEE modules. The run stop command causes the trigger module to stop issuing triggers. The run conditions are output to latch 2 to confirm successful data transfer.

Triggers are issued for a variety of reasons which can be split into four basic groups: triggers that issue global acquisition commands to the ID FEE, triggers that issue global acquisition commands to the OD FEE, triggers that issue stop commands to the MACRO electronics, and other triggers that do not necessarily issue a command. Two ID FEE triggers or two OD FEE triggers can not be issued within 200 ns of each other. Most of these triggers can be enabled or disabled. The details of each trigger are described below.

C.2.1 ID FEE triggers

- Singles Trigger: A global acquisition command is issued to the ID FEE modules when N_{ID} crosses above a threshold set by the DAQ.

- Prescale Trigger: A global acquisition command is issued to the ID FEE modules when both of these conditions are met: N_{ID} crosses above threshold, and the absolute time is within the prescale time from the last 1PPS signal. Both the threshold and prescale time (in multiples up to 65535 of $102.4\,\mu$s) are set by the DAQ. This is used when the event rate is too high for the DAQ to handle.

- Prompt Trigger: A global acquisition command is issued to the ID FEE modules, and a window of time for a delayed trigger is opened when N_{ID} crosses above threshold. Both the threshold and delay time (in multiples up to 65535 of

25 ns) are set by the DAQ. To reduce data size, the issuing of the global acquisition command to the FEE can be disabled by the DAQ. However, the trigger record is still produced and the delayed trigger time window is still opened.

- Delayed Trigger: A global acquisition command is issued to the ID FEE modules when both of these conditions are met: N_{ID} crosses above threshold, and a prompt trigger has occurred within the delay time. Both the threshold and delay time (in multiples up to 65535 of 25 ns) are set by the DAQ.

- Five Inch PMT Trigger: A global acquisition command is issued to the ID FEE modules when $N_{5"}$ crosses above a threshold set by the DAQ.

- OD to ID Trigger: A global acquisition command is issued to the ID FEE modules when there is an OD FEE trigger.

C.2.2 OD FEE triggers

- OD Singles Trigger: A global acquisition command is issued to the OD FEE modules when either N_{ODtop}, N_{ODupper}, N_{ODlower}, or N_{ODbottom} crosses above the threshold set for each section by the DAQ.

- ID to OD Trigger: A global acquisition command is issued to the OD FEE modules when there is an ID FEE trigger.

C.2.3 MACRO triggers

- MACRO Singles Trigger: A short stop command is issued to the MACRO electronics 20 μs after N_{ID} crosses above a threshold set by the DAQ. This trigger is prescaled so that the trigger is only issued when N_{ID} crosses above threshold a certain number of times. This number is set by the DAQ.

- MACRO Doubles Trigger: A long stop command is issued to the MACRO electronics 200 μs after $339 < \mathrm{NMax}_{\mathrm{ID}} < 540$ if $199 < \mathrm{NMax}_{\mathrm{ID}} < 1050$ within the previous 300 ns to 500 μs.

- MACRO Muon Trigger: A short stop command is issued to the MACRO electronics 130 μs after $N_{\mathrm{ID}} > 1303$.

- MACRO Random Trigger: A short stop command is issued to the MACRO electronics every 32 s.

C.2.4 Other triggers

- History Trigger: For up to 8 consecutive clock-ticks, a trigger record is produced while N_{ID} is above a threshold set by the DAQ.

- OD History Trigger: For up to 8 consecutive clock-ticks each, a trigger record is produced while either N_{ODtop}, N_{ODupper}, N_{ODlower}, or N_{ODbottom} is above the threshold set by the DAQ for each section.

- 1PPS Trigger: A trigger record is produced every time the trigger module receives a 1PPS input.

- GPS Trigger: This is issued every 32 s and cannot be disabled; it freezes the GPS time for later readout. The issuing of a forced acquisition command to all the FEE modules at the same time can be enabled by the DAQ.

- Supernova Trigger: This is designed to detect the neutrino signal from a supernova, described in Section D. If the trigger module observes eight events with $N_{\mathrm{ID}} \geq 772$ in $\sim$0.84 s this is treated as a supernova candidate. After a supernova candidate is observed, the trigger module sets optimal trigger parameters to collect as many supernova events as possible for 1 min before returning to the initial trigger parameters. Normal trigger parameters would collect most supernova events but could miss the important proton scattering events. The rarity of observation of supernova explosions make it important to collect as many supernova events as possible. This trigger is almost always enabled so supernova events will be collect even if we are operating with sub optimal trigger parameters. When the DAQ receives the supernova trigger, it prevents the shift taker from stopping the run for 1 min.

- Forced Calibration Trigger: A forced acquisition command is issued to either the ID or OD FEE modules when the trigger module receives an input pulse. The pulse is generated by a calibration device, such as a laser, and must arrive just before the signals from the photons have reached the FEE.

- Global Calibration Trigger: A global acquisition command is issued to either the ID or OD FEE modules 8 clock-ticks[3] after the trigger module receives an input pulse. The pulse is generated by a calibration device, such as a laser, and must arrive just before the signals from the photons have reached the FEE.

- Delayed Calibration Trigger: A trigger record is produced 15 clock-ticks after the trigger module receives an input pulse. The pulse is generated by a calibration device, such as a laser, and must arrive just before the signals from the photons have reached the FEE. This records the $\mathrm{N_{ID}}$ when the signals from the photons have reached the FEE.

- Disable and Enable Triggers: The trigger module disables the issuing of other triggers when the trigger board memory becomes almost full. The trigger module enables the issuing of other triggers when the trigger board memory empties.

- Acquisition Trigger: One of the following commands is issued to the FEE modules: 0x2, 0x3, 0x4, 0x5, 0x8, 0x9, 0xa, 0xb, 0xc, 0x12, or 0x13; see Table A.1. The command is issued a number of times, set by the DAQ up to 65535, at fixed intervals, set by the DAQ in multiples up to 65335 of 102.4 μs.

Table C.1 lists the unique trigger type associated with each of the triggers described above. The trigger record contains the timestamp, trigger type, $\mathrm{N_{ID}}$, $\mathrm{N_{ODtop}}$, $\mathrm{N_{ODupper}}$, $\mathrm{N_{ODlower}}$, $\mathrm{N_{ODbottom}}$, $\mathrm{N_{5"}}$, and calibration number. The calibration number is the number of calibration input signals since the start of the run. The trigger record is transmitted as five 32-bit words using serial transfer with latch 1. Figure C.4 shows the format of the trigger record, which includes identification on which word is being transferred, so that data with missing words can be identified. A buffer, 511 trigger

---

[3] This time was too short to collect all the light, so it was increased to 15 clock-ticks from run 3381 in February, 2004.

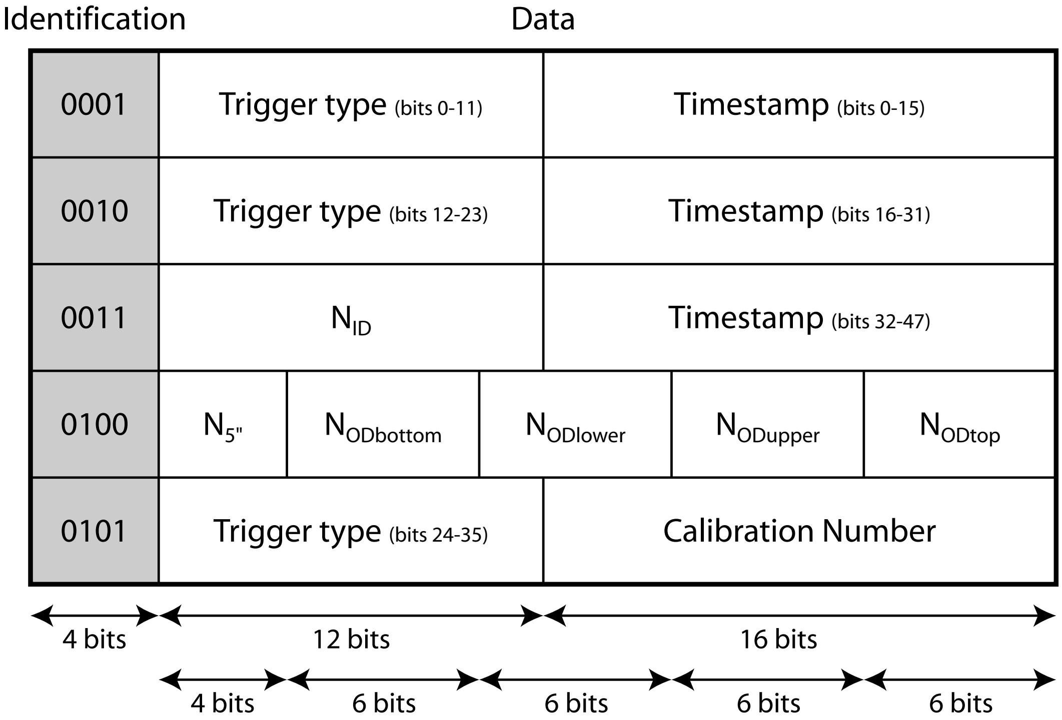

Identification	Data				
0001	Trigger type (bits 0-11)		Timestamp (bits 0-15)		
0010	Trigger type (bits 12-23)		Timestamp (bits 16-31)		
0011	N_{ID}		Timestamp (bits 32-47)		
0100	$N_{5''}$	$N_{ODbottom}$	$N_{ODlower}$	$N_{ODupper}$	N_{ODtop}
0101	Trigger type (bits 24-35)		Calibration Number		

Figure C.4: The trigger record data format. The Timestamp and Trigger type are a 48-bit and 36-bit number, respectively.

records deep, incorporated into the third FPGA allows for a trigger rate of 40 MHz for a brief period. However the continuous possible trigger rate depends on the total data transfer speed, which is limited by the latch to ∼40 kHz.

Trigger Type	Description
0x000,000,001	ID singles trigger
0x000,000,002	ID history trigger
0x000,000,004	5 inch PMT trigger
0x000,000,008	1pps trigger
0x000,000,0X0[a]	Acquire Trigger
0x000,000,100	ID prescale trigger
0x000,000,200	GPS trigger
0x000,000,400	Delayed calibration trigger
0x000,000,800	Supernova trigger
0x000,00X,000[b]	Calibration Trigger
0x000,010,000	MACRO singles trigger
0x000,020,000	MACRO coincidence trigger
0x000,040,000	MACRO random trigger
0x000,080,000	MACRO muon trigger
0x000,100,000	OD top singles trigger
0x000,200,000	OD upper singles trigger
0x000,400,000	OD lower singles trigger
0x000,800,000	OD bottom singles trigger
0x001,000,000	ID delayed trigger
0x002,000,000	ID prompt trigger
0x004,000,000	OD to ID trigger
0x008,000,000	ID to OD trigger
0x010,000,000	OD top history trigger
0x020,000,000	OD upper history trigger
0x040,000,000	OD lower history trigger
0x080,000,000	OD bottom history trigger
0x400,000,000	Disable trigger
0x800,000,000	Enable trigger

Table C.1: Summary of the different triggers.

---

[a] X = 1-b correspond to the following FEE commands (see Table A.1) 0x02, 0x03, 0x04, 0x05, 0x08, 0x09, 0x12, 0x13, 0x0a, 0x0b, and 0x0c, respectively

[b] X = 1-5 correspond to different ID forced acquisition triggers, X = 6-7 OD forced acquisition trigger, X = 9-d ID global acquisition trigger, X = e-f OD global acquisition trigger

Appendix D

Supernova

A "standard" supernova is thought to release 3×10^{46} J of energy over 10 s[57]. Essentially all this energy is evenly distributed among ν_e's, $\bar{\nu}_\mathrm{e}$'s, ν_μ's, $\bar{\nu}_\mu$'s, ν_τ's, and $\bar{\nu}_\tau$'s. Due to their different interactions with matter, the different neutrino flavors leave the supernova with different mean energies. The mean ν_e energy is $\sim 11\,\mathrm{MeV}$, the mean $\bar{\nu}_\mathrm{e}$ energy is $\sim 16\,\mathrm{MeV}$, and the mean energy of the other neutrino flavors is $\sim 25\,\mathrm{MeV}$. Based on these assumptions, Table D.1 gives the number of neutrinos that would be observed with KamLAND from a "standard" supernova in the center of the Milky Way, $\sim$10 kpc away. These numbers do not include neutrino oscillations. The exact numbers would depend on neutrino oscillations, neutrino temperatures and energy released. Because of their spectral information, the proton scatter events allow us to independently measure the ν_x temperature and energy released. KamLAND is the only operating experiment that could do this; however, a very low threshold is required to record a significant number of events, and there is no coincidence signature to help reduce backgrounds.

It is expected that on average there are about three type II supernova per century [60, 61] in the Milky Way. The last nearby supernova was SN1987A in the Large Magellanic Cloud, approximately 50 kpc[62] away. A total of $\sim$19 neutrinos were observed from SN1987A at the Kamiokande[63] and IMB[64] detectors.

Detection Mechanisim	Expected Number	Reference
$\bar{\nu}_{\mathrm{e}} + \mathrm{p} \rightarrow \mathrm{e}^{+} + \mathrm{n}$	330	[58]
$\nu_x +^{12}\mathrm{C} \rightarrow \nu_x +^{12}\mathrm{C}^{*} + \gamma(15.11\mathrm{MeV})$	57.6	[58]
$\nu_e +^{12}\mathrm{C} \rightarrow \mathrm{e}^{-} +^{12}\mathrm{N}$	1.9	[58]
$\bar{\nu}_{\mathrm{e}} +^{12}\mathrm{C} \rightarrow \mathrm{e}^{+} +^{12}\mathrm{B}$	7.4	[58]
$\nu_x + \mathrm{p} \rightarrow \nu_x + \mathrm{p}$	273[a]	[59]

Table D.1: Expected supernova events observable with KamLAND for a "standard" supernova in the center of the Milky Way assuming no neutrino oscillations.

---

[a] Based on a 0.2MeV threshold

Appendix E

DAQ

KamLAND uses KiNOKO[1][65] (KiNOKO is Network distributed Object oriented KamLAND Online system) DAQ. The top layer of the KiNOKO system is divided into components, each of which has its own function and connections to other components. Figure E.1 shows a diagram of the components involved in data acquisition, viewing, and storage in the KamLAND system. KiNOKO processes can access an object on a remote computer as if it were a local object. This allows KiNOKO to operate as a network distributed parallel processing system while behaving as a single integrated system.

KiNOKO uses a universal scripting language; the user can describe multiple system setups without needing to edit the source code. The system generally needs four scripts: a readout script (.kts), viewer script (.kvs), component script (.kcom), and control panel script (.kcml). Code to access measurement devices is written in a similar manner to UNIX device drivers; it is a modular code block detached from the main application. The interface implements functions to operate the device, rather than being coded for a particular application. The code to operate the measurement devices is part of the readout script, which forms the bases of the "data collectors" in Figure E.1. The trigger module and the FEE are readout at a fixed rate of 10 Hz. The MACRO electronics uses an interrupt to readout the electronics whenever it receives

---

[1] Although this was developed for KamLAND, it is general enough for use in a large variety of applications.

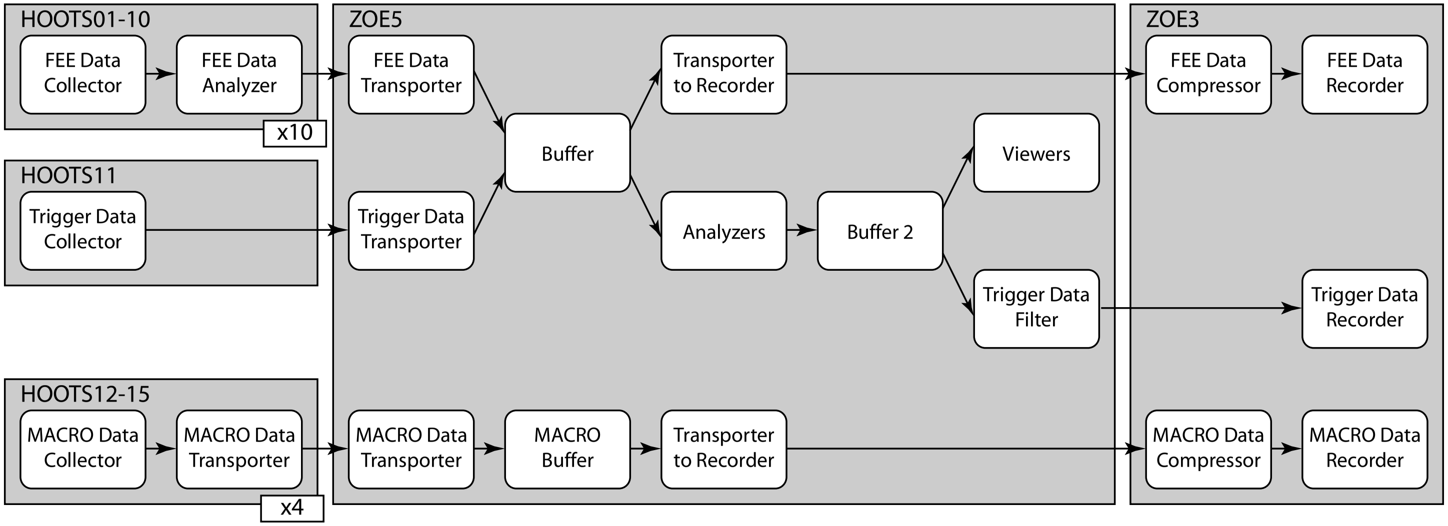

Figure E.1: Schematic of the DAQ components. Hoots1-15, Zoe3, and Zoe5 are different computers.

a stop command.

In Figure E.1 the component labelled “analyzers” consists of three different analyzers chained together in series, and the component labelled “viewers” consists of four different viewers chained together in series. The viewers display summary information from the analyzers. The trigger data analyzer takes the “raw” trigger data consisting of five 32-bit words, shown in Figure C.4, checks all words are received, and associates the timestamp, trigger type, $\mathrm{N_{ID}}$, $\mathrm{N_{ODtop}}$, $\mathrm{N_{ODupper}}$, $\mathrm{N_{ODlower}}$, $\mathrm{N_{ODbottom}}$, and $\mathrm{N_{5''}}$ with a single trigger event. It also calculates $\mathrm{NMax_{ID}}$, $\mathrm{NMax_{OD}}$, and the number of ID and OD triggers in the previous second.

Appendix F

Vertex algorithm

The event vertex is calculated from the collection of pulse arrival times and the number of PE's. The Peak Time Fitter (PTF) vertex algorithm assumes photons travel in a straight line from the vertex to the PMT and the speeds of light in the scintillator and buffer oil are $195\,\mathrm{mm\,ns^{-1}}$ and $205\,\mathrm{mm\,ns^{-1}}$, respectively. The PTF algorithm can be broken down into the following steps:

1 Pulses with 0.2 to 10 PE's are selected.

2 An initial estimated event vertex is calculated from the distribution of light, given by

$$\mathbf{r} = \frac{1.62 \sum_i \mathrm{PE}_i \mathbf{r}_i}{\sum_i \mathrm{PE}_i},$$

where $\mathbf{r}_i$ is the location of the PMT with the i^{th} pulse.

3 A histogram of the pulse arrival time adjusted for the time of flight from the estimated vertex is calculated.

4 The mean arrival time of the peak, t_{peak}, is estimated from the pulses in the time window between 10 ns before and 5 ns after the maximum bin in the histogram.

5 Pulses arriving between 10 ns before and 5 ns after t_{peak} are selected.

6 A correction to the current estimated vertex is calculated from the selected pulses arrival times,

$$\Delta\mathbf{r} = \sum_i (\mathbf{r} - \mathbf{r}_i) \frac{t(\mathbf{r} - \mathbf{r}_i) - (t_i - t_{peak})}{t_i - t_{peak}} \mathrm{PE}_i,$$

where $\mathbf{r}$ is the current estimated vertex, $t(\mathbf{r} - \mathbf{r}_i)$ is the time of flight from the current estimated vertex to the PMT with the i^{th} pulse, and t_i is the arrival time of the pulse.

7 The mean arrival time corrected for travel time from the current estimated vertex, t_{peak}, is calculated for the selected pulses.

8 A new estimate of the vertex is calculated from $\mathbf{r} + \Delta\mathbf{r}$.

9 Steps 5 to 8 are repeated until $|\Delta\mathbf{r}| < 5\,\mathrm{mm}$, then repeat another 10 times.

Appendix G

Livetime calculation

When the trigger module disables and later re-enables, it issues disable[1] and enable triggers; see Appendix C.2.4, allowing us to determine the length of these periods. These triggers are not recorded in the actual data; however, they are recorded by the trigger data analyzer, described in Appendix E.

Using the data from the trigger data analyzer, the livetime is determined to the accuracy[2] of the 40MHz clock, 0.01 %. Figure G.1 shows the trigger module disable periods versus run number. The trigger module was disabled for 0.55 % and 0.012 % of the time before and after run 876, respectively. Disable periods longer than 0.1s are caused by slow processing of data by the DAQ. These periods represent 99.83 % and 95.3 % of the disable period before and after run 876, respectively. The peak in disable periods at 0.41ms is caused by the trigger boards internal buffer becoming full due to short bursts of data. This is the time needed to transfer this data from the trigger memory. Using the data from the trigger data analyzer, the fraction of the total time when the trigger was disabled for less than 0.1s is $\sim 9 \times 10^{-4}$ % and $\sim 6 \times 10^{-4}$ % before and after run 876, respectively. These short disables are not excluded from the livetime calculated in Section 4.4; however, this causes negligible

---

[1] There was a problem with disable triggers sometimes not being issued before run 876 in July 2002. However, the disable periods can be easily calculated since the last trigger before the enable trigger should have occurred one clock-tick prior to the missing disable trigger.

[2] The quoted accuracy includes aging and an operating temperature range of 0°C to 70°C. The actual accuracy during operation is probably better than this.

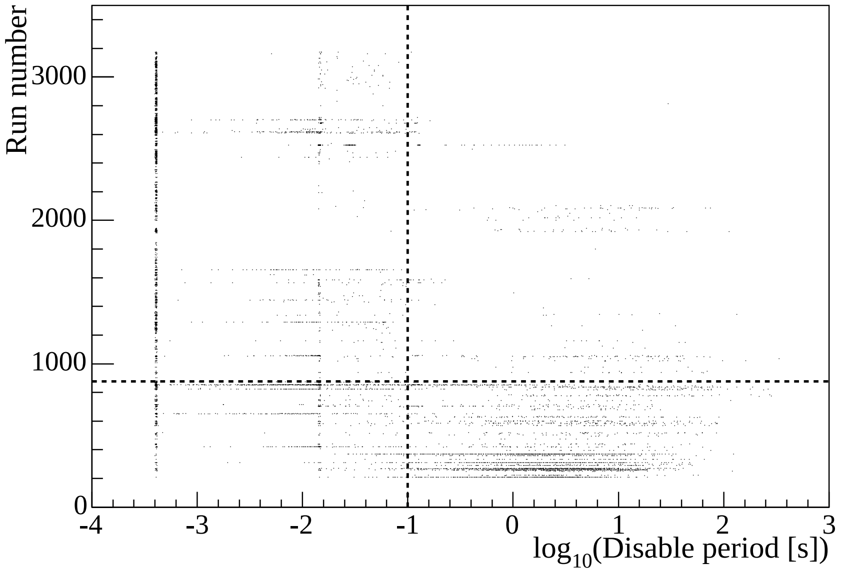

Figure G.1: Trigger disable period calculated from the trigger data analyzer data.

error.

The livetime calculated from the number of clock-ticks while the trigger is enabled is compared to the number of 1pps triggers. The livetimes from these two methods agree within $1 \times 10^{-3}\,\%$ after run 876[3], which is approximately a factor of 10 better than the quoted accuracy of the 40MHz clock. This error in the clock period results in a negligible error in the calculated livetime.

---

[3] The 1pps trigger was not enabled during supernova mode before run 876 in July, 2002.

Bibliography

[1] G. Eder, Nucl. Phys. **78**, 657 (1966).

[2] G. Marx, Czech. J. Phys. B **19**, 1471 (1969).

[3] G. Schubert, D. L. Turcotte, and P. Olson, *Mantle Convection in the Earth and Planets* (Cambridge University Press, Cambridge, 2001).

[4] A. A. Kremenetsky and L. N. Ovhinnikov, Precambrian Res. **33**, 11 (1986).

[5] S. R. Taylor and S. M. McLennan, *The Continental Crust: Its Composition and Evolution: An Examination of the Geochemical Record Preserved in Sedimentary Rocks* (Blackwell Scientific Publications, Oxford, 1985).

[6] R. L. Rudnick and D. M. Fountain, Rev. Geophys. **33**, 267 (1995).

[7] W. F. McDonough and S. s. Sun, Chem. Geol. **120**, 223 (1995).

[8] G. C. Brown and A. E. Mussett, *The Inaccessible Earth* (Chapman & Hall, London, 1993).

[9] D. M. Shaw, Trans. Roy. Soc. Canada **19**, 233 (1981).

[10] E. Anders and N. Grevesse, Geochim. Cosmochim. Acta **53**, 197 (1989).

[11] A. Rocholl and K. P. Jochum, Earth Planet. Sci. Lett. **117**, 265 (1993).

[12] J. Zschau, Tidal friction in the solid earth: Constraints from the chandler wobble period, in *Space Geodesy and Geodynamics*, edited by P. Brosche and J. Sundermann, p. 315, Springer-Verlag, Berlin, 1978.

[13] H. N. Pollack, S. J. Hurter, and J. R. Johnson, Rev. Geophys. **31**, 267 (1993).

[14] F. M. Richter, Earth Planet. Sci. Lett. **68**, 471 (1984).

[15] M. J. Jackson and H. N. Pollack, J. Geophys. Res. **89**, 10103 (1984).

[16] T. Spohn and G. Schubert, J. Geophys. Res. **87**, 4682 (1982).

[17] http://ie.lbl.gov/ensdf/.

[18] E. Holzschuh, Rep. Prog. Phys. **55**, 1035 (1992).

[19] H. Behrens and J. Jänecke, *Numerical Tables for Beta Decay and Electron Capture* Vol. 4, Landolt-Börnstein - Group I Elementary Particles, Nuclei and Atoms (Springer-Verlag, New York, 1969).

[20] R. D. McKeown and P. Vogel, Phys. Rep. **394**, 315 (2004).

[21] T. Araki *et al.*, (2005), arXiv:hep-ex/040635.

[22] Y. Ashie *et al.*, Phys. Rev. Lett. **93**, 101801 (2004).

[23] M. Apollonio *et al.*, Eur. Phys. J. C **27**, 331 (2003).

[24] P. Vogel and J. F. Beacom, Phys. Rev. D **60**, 053003 (1999).

[25] A. Kurylov, M. J. Ramsey-Musolf, and P. Vogel, Phys. Rev. C **67**, 035502 (2003).

[26] K. Eguchi *et al.*, Phys. Rev. Lett. **90**, 021802 (2003).

[27] F. Mantovani, L. Carmignani, G. Fiorentini, and M. Lissia, Phys. Rev. D **69**, 013001 (2004).

[28] J. B. Benziger *et al.*, Nucl. Instrum. Methods Phys. Res., Sect. A **417**, 278 (1998).

[29] W. H. Press, B. P. Flannery, S. A. Teukolsky, and W. T. Vetterling, *Numerical Recipes in C: The Art of Scientific Computing* (Cambridge University Press, Cambridge, 1992), chap. 14.

[30] J. B. Birks, *The theory and practice of scintillation counting* Vol. 27, International series of monographs on electronics and instrumentation (Macmillian, New York, 1964), chap. 6.

[31] J. D. Jackson, *Classical Electrodynamics* (Wiley, New York, 1990), pp. 637–640.

[32] S. Agostinelli *et al.*, Nucl. Instrum. Methods Phys. Res., Sect. A **506**, 250 (2003).

[33] S. F. Mughabghab, M. Divadeenam, and N. Holdenothers, *Neutron Cross Sections* (Academic Press, New York, 1981).

[34] K. Schreckenbach, G. Colvin, W. Gelletly, and F. Vonfeilitzsch, Phys. Lett. B **160**, 325 (1985).

[35] A. A. Hahn *et al.*, Phys. Lett. B **218**, 365 (1989).

[36] V. I. Kopeikin, L. A. Mikaelyan, and V. V. Sinev, Phys. Atom. Nuclei **64**, 849 (2001).

[37] P. Vogel, G. K. Schenter, F. M. Mann, and R. E. Schenter, Phys. Rev. C **24**, 1543 (1981).

[38] B. Achkar *et al.*, Phys. Lett. B **374**, 243 (1996).

[39] R. Bunn *et al.*, *Interim storage of spent nuclear fuel: A safe, flexible, and cost-effective near-term approach to spent fuel managment* (Harvard University, 2001), http://www.ksg.harvard.edu/bcsia/atom.

[40] http://wwwndc.tokai.jaeri.go.jp/ftpnd/jendl/jendl-an-2003.html.

[41] http://www.srim.org/.

[42] D. West and A. C. Sherwood, Ann. Nucl. Energy **9**, 551 (1982).

[43] R. B. Walton, J. D. Clement, and F. Boreli, Phys. Rev. **107**, 1065 (1957).

[44] G. W. Kerr, J. M. Morris, and J. R. Risser, Nucl. Phys. **A110**, 637 (1968).

[45] G. J. H. Jacobs and H. Liskien, Ann. Nucl. Energy **10**, 541 (1983).

[46] Geant - detector description and simulation tool, CERN Program Library Long Writeup W5013, 1993.

[47] G. Horton-Smith, private communication.

[48] S. Eidelman *et al.*, Phys. Lett. B **592**, 272 (2004).

[49] D. Lal, Annu. Rev. Earth Pl. Sc. **16**, 355 (1988).

[50] D. R. Tilley *et al.*, Nucl. Phys. A **745**, 155 (2004).

[51] G. Ranucci, A. Goretti, and P. Lombardi, Nucl. Instrum. Methods Phys. Res., Sect. A **412**, 374 (1998).

[52] E. Gatti and F. D. Martini, A new linear method of discrimination between elementary particles in scintillation counters, in *Conference on Nuclear Electronics, Belgrade 1961*, Vol. 2, p. 265, International Atomic Energy Agency, 1962.

[53] A. Stuart, *Kendall's advanced theory of statistics* Vol. 2A (Oxford University Press, New York, 1999).

[54] S. N. Ahmed *et al.*, Phys. Rev. Lett. **92**, 181301 (2004).

[55] G. Fiorentini, M. Lissia, F. Mantovani, and R. Vannucci, (2005), arXiv:hep-ph/0501111.

[56] G. Gratta, L. Miller, C. Roat, D. Tracy, and Y. Wang, Nucl. Instrum. Methods Phys. Res., Sect. A **400**, 456 (1997).

[57] P. Vogel, Supernova neutrinos, X International Workshop on Neutrino Telescopes, Venice, Italy, 2003, arXiv:nucl-th/0305003.

[58] Alivisatos *et al.*, Stanford University Report No. HEP-98-03, 1998 (unpublished), http://hep.stanford.edu/∼gratta/kamland_prop.ps.gz.

[59] J. F. Beacom, W. M. Farr, and P. Vogel, Phys. Rev. D **66**, 033001 (2002).

[60] S. van den Bergh, Phys. Rep. **204**, 385 (1991).

[61] G. A. Tammann, W. Loffler, and A. Schroder, Astrophys. J. Suppl. S. **92**, 487 (1994).

[62] N. Panagia, R. Gilmozzi, F. Macchetto, H. M. Adorf, and R. Kirshner, Astrophys. J. Lett. **380**, L23 (1991).

[63] K. Hirata *et al.*, Phys. Rev. Lett. **58**, 1490 (1987).

[64] R. M. Bionta *et al.*, Phys. Rev. Lett. **58**, 1494 (1987).

[65] http://www.awa.tohoku.ac.jp/ naoko/kinoko-e/.